SAND2023-05244T

Jonathan E. Bainbridge

Candidate

Physics & Astronomy

Department

This dissertation is approved, and it is acceptable in quality and form for publication:

Approved by the Dissertation Committee:

Peter Schwindt

Chair

Ivan Deutsch

Member

Tara Drake

Member

Paul Schwoebel

Member

An Optically Pumped Comagnetometer for High-sensitivity RF Detection without Magnetic Shielding

by

Jonathan Edward Bainbridge

A.S., Clinton Community College, 2012
B.A., Physics & Mathematics, Coe College, 2016
M.S., Physics, University of New Mexico, 2020

THESIS

Submitted in Partial Fulfillment of the

Requirements for the Degree of

Doctor of Philosophy
Physics

The University of New Mexico

Albuquerque, New Mexico

May, 2024

Dedication

To my dear sweet wife Evelyn, our lovely dog Lucie, and the family we have built together. I hope to share many more years together.
And to my family, who always supported me in my academic journey.

"They don't think it be like it is. But it do" – Oscar Gamble

Acknowledgments

Thanks to Ivan Deutsch for sharing his infectious enthusiasm for atomic physics, and to fellow Sandian and UNM alumnus Adrian Orozco for connecting me to research opportunities at Sandia during our shared time as graduate students.

I am appreciative of numerous Sandians for their support. Special gratitude is extended to to my dissertation advisor, Peter Schwindt, for giving me the opportunity to work on this project, and for his precious time and effort spent mentoring me. I am also thankful to Mike Martin for his early tutelage in foundational laboratory skills. More broadly, I would like to express my appreciation of everyone I have shared the laboratory with, including but not limited to Tony Carter, Kaleb Kaleb Cambell, Matthew Chow, Bethany Little, William Kindel, and Danial Thrasher. Special recognition is extended to the Sandians who worked directly on this research project, including Neil Clausen, Jeffrey Bach, Lee Marshell, and Joonas Iivanainen. Finally, thanks to Matthew Currey for sharing his wise insights on writing a dissertation such as this.

I am eternally grateful to my wonderful family, who have always supported my pursuit of a career in science, and for the unwavering support of my lovely wife Evelyn and to our amazing dog Lucie-Goosie who always makes me smile. Thanks, in a broader sense, to New Mexico itself, this great Land of Enchantment. In the natural majesty and solitude of which I have found a peace I had never hitherto known.

Finally, I am thankful to Sandia National Laboratories for organizing and supporting this work through their laboratory directed research and development (LDRD) program. *

*Sandia National Laboratories is a multimission laboratory managed and operated by National Technology & Engineering Solutions of Sandia, LLC, a wholly owned subsidiary of Honeywell International Inc., for the U.S. Department of Energy's National Nuclear Security Administration under contract DE-NA0003525

An Optically Pumped Comagnetometer for High-sensitivity RF Detection without Magnetic Shielding

by

Jonathan Edward Bainbridge

A.S., Clinton Community College, 2012

B.A., Physics & Mathematics, Coe College, 2016

M.S., Physics, University of New Mexico, 2020

Ph.D., Physics, University of New Mexico, 2024

Abstract

We develop an optically-pumped magnetometer (OPM) sensitive in the radiofrequency(RF) regime based on ^{85}Rb in a natural abundance rubidium vapor cell to operate in dynamic geomagnetic field environments. Because high sensitivity operation of RF OPMs requires control of the magnetic field environment near DC, we develop an OPM *comagnetometer* that also utilizes the ^{87}Rb present within the same vapor cell to implement a secondary OPM *variometer* that provides information on the field-environment near DC. This information is used to provide feedback via a set of tri-axial field control coils that counters the unwanted effects of external geomagnetic fields from DC to 60 Hz, which in turn allows RF OPM operation with an intrinsic sensitivity of around 9 fT Hz$^{-1/2}$ in the presence of external magnetic fields on the order of 10s of μT.

Contents

List of Figures

List of Tables

Glossary

OPM	Optically-pumped magnetometer.
RF	Radio-frequency.
γ	Gyromagnetic ratio.
$\mathbf{e}_\mu$	Unit vector in direction $\mu = \{x, y, z\}$.
FWHM	Full width at half maximum.
LF	Low frequency. Frequencies from 30 to 300 kHz.
VLF	Very-low frequency. Frequencies from 3 to 30 kHz.

Chapter 1

Introduction

In 1865, James Clerk Maxwell laid the theoretical foundation for much of the modern world [61]. His landmark synthesis of electromagnetic theory into a single set of equations elucidated that light could be described as an electromagnetic wave that propagates through space. In a series of landmark experiments in 1887-1888, Heinrich Hertz experimentally confirmed the existence of electromagnetic waves as predicted by Maxwell's theory [41, 40, 43, 42]. Building on this success, generation and detection of electromagnetic waves became the basis for many of the great technological innovations of the 20th century, with little indication of this rate of technological innovation slowing thus far into the 21st.

The plethora of applications of electromagnetic waves stems partially from the fact that their frequency can vary across a vast range. Everything from radio-frequency (RF) and below on the low end ranging from near DC to about 300 MHz, to microwaves in the range from 300 MHz to 300 GHz, and then infrared,visible, and ultraviolet light up to hundreds of terahertz! In this work, we will focus on detection of signals in the lower end of the RF portion of the spectrum, from about 3 kHz to 3 MHz, corresponding to the very-low frequency (VLF), low frequency (LF) and medium frequency (MF) bands [49]. Some applications in this area include nuclear

magnetic resonance (NMR) and nuclear quadrupole (NQR) for chemical detection and imaging [74, 76, 73, 54, 52, 24, 23, 22], and electromagnetic induction imaging (EMI) in conductive materials [94, 95, 15, 16, 17, 28, 31, 31, 29, 57, 60, 50]. Signals of interest require sensitivity on the level of fT $\mathrm{Hz}^{-1/2}$ or better. Existing pick-up coils are pressed to achieve this level of sensitivity within a reasonable footprint for many potential use cases, such as detection of explosives or achieving acceptable spatial resolution in EMI images. We seek to develop a quantum sensor to address these challenges.

This dissertation details the development of an OPM that uses ^{85}Rb to achieve exceptionally high sensitivity to electromagnetic fields in the above mentioned frequency range from 3 kHz to 3 MHz. While the basic approach described here has been implemented previously [75, 54, 74, 76, 73, 52, 24], this platform provides high sensitivity while operating outside of a magnetically shielded environment without the need for a multi-channel gradiometric configuration to facilitate common-mode noise cancellation. Key to this approach is the implementation of a second OPM within the same vapor cell using the ^{87}Rb that is also present within natural rubidium vapor. Using this *comagnetometer*, the low-frequency external field below 60 Hz is determined and actively compensated using a set of tri-axial field control coils. Active stabilization of the magnetic field environment near DC allows for the operation of our device within dynamic environments outside of a magnetic shield.

1.1 Radio-frequency Atomic Sensing

In the most basic atomic magnetometer, we use the Larmor precession of the magnetic moment of the atom. The frequency of Larmor precession f_L depends on the applied magnetic field $\mathbf{B}$ as given by the equation:

$$2\pi f_{\mathrm{L}} = \gamma|\mathbf{B}|. \tag{1.1}$$

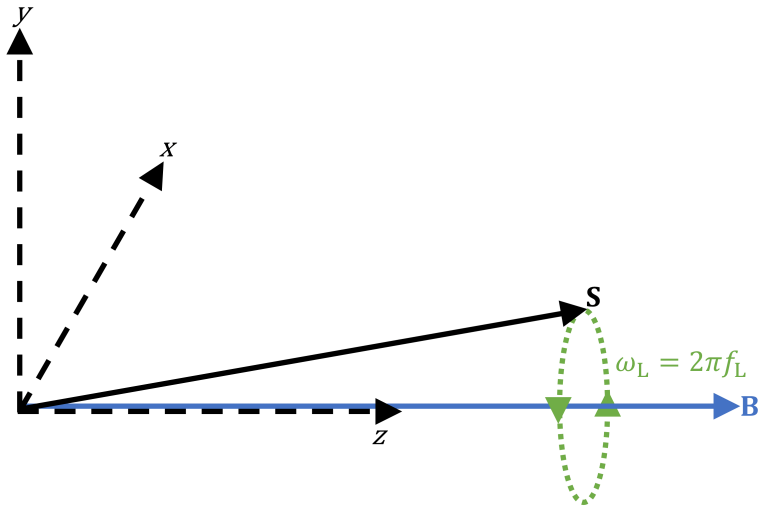

Figure 1.1: Larmor resonance of the atomic spin **S** about the longitudinal (z)-axis in magnetic field **B** at angular frequency $\omega_L = 2\pi f_L$.

So by measuring the Larmor frequency f_L, we can determine the external field amplitude $|\mathbf{B}|$ if we know the gyromagnetic ratio. However, we can look at this equation in another way; by setting the external field $|\mathbf{B}|$, we can detect signals at a frequency $f = f_L$, so long as the magnitude of the RF signal remains small compared to the total field amplitude $|\mathbf{B}|$. The bandwidth of the atomic response will be given by an approximately Lorentzian profile centered at f_L, as discussed in Section 2.1.1. In the experiments detailed in this work, we use the atoms within a hot rubidium vapor, with a bandwidth around $\Delta f = 1.5\,\text{kHz}$ FWHM.

Savukov et al (2005) demonstrated how to make an OPM that is sensitive at RF frequencies using this basic idea [75]. They were able to achieve a sensitivity of $2\,\text{fT Hz}^{-1/2}$. However, as seen from Equation 1.1, the magnetic field seen by the atoms must be precisely controlled to enable this method. The requirement of precise magnetic field control limited the application of this approach to shielded environments. In this work, we develop a new approach for providing active feedback to compensate the external field which enables the use of this approach outside a

magnetically shielded environment.

1.2 Variometry for Bias Field Control

As seen in the previous section, RF atomic magnetometry requires precise control of the magnetic field **B**. Compensation can be provided via currents run through a set of tri-axial electromagnetic coils. However, we must know which currents to apply for creating control fields that cancel the external field in each direction. For this we need a vector magnetometer that operates at low frequencies to provide this external field information. This can be accomplished using an additional fluxgate magnetometer located as near as possible to the atoms used for RF sensing. Indeed, it *is* done in several experiments in the United Kingdom focused on electromagnetic imaging applications [31, 50, 16]. However, in order to reduce the volume, weight, and power consumption of our device as much as possible, whilst simultaneously sampling the magnetic field from within the same volume as the atoms measuring the RF signal, we elected to use another OPM within the same vapor cell.

Our approach instead uses a secondary OPM *variometer* as detailed by Alexandrov et al. (2004) [4, 3]. This method starts with a standard scalar magnetometer based on a hot alkali vapor that is only sensitive to the total field amplitude $|\mathbf{B}|$ and adds a a rotating modulation within the transverse plane that imposes an amplitude modulation on the signal when external fields are not aligned along the longitudinal direction of the device. The phase of this amplitude modulation is additionally dependent on the orientation of the external perturbing field, and can be used to separate the signal into two orthogonal axes within the transverse plane. This leads to a device that is separately sensitive to the transverse field $\mathbf{B}_\perp = B_x\mathbf{e}_x + B_y\mathbf{e}_y$ and total field amplitude, which is sufficient information to determine the tri-axial field

information using the relation:

$$\mathbf{B} = B_z\mathbf{e}_z + B_x\mathbf{e}_x + B_y\mathbf{e}_y; \tag{1.2}$$

from which we can determine the z-direction field to be:

$$B_z = \sqrt{|\mathbf{B}|^2 - B_\perp^2}. \tag{1.3}$$

We implement a variometer within hot rubidium vapor using ^{87}Rb that makes up a minority of natural rubidium vapor. Our implementation has a feedback bandwidth of DC-60 Hz, with a maximum effective slew rate of about $8\,\mu\mathrm{T\ s}^{-1}$, limited primarily by the need to maintain high RF sensitivity. As we shall see, there is a fundamental trade-off between the sensitivity of the variometer and RF magnetometer.

1.3 Overview

In this dissertation, we will first review the atomic physics to both aspects of our magnetometers. Chapter 2 provides a review of the physics of RF OPMS. Chapter 3 describes the principles of the OPM variometer. Chapter 4 discusses the synthesis of both an RF OPM and OPM variometer into a single vapor cell, including the development of the digital and analog aspects of the control system. Chapter 6 provides a summary, conclusions, and future outlook. Additional content not included in this document is archived separately at the Sandia National Laboratories Technical Library, New Mexico, reachable at 505-845-8287 or libref@sandia.gov. Access to this additional content will be provided to appropriate parties upon request.

The work presented in Chapters 3 and 4 were published in the literature in a peer-reviewed paper [33]*.

*Note that the author used their married last name for this publication. Because this degree program was already in-progress before said marriage, they will retain their legal last name "Bainbridge" as currently enrolled for purposes of this thesis.

Chapter 2

The Physics of RF OPMs

In Section 1.1 a brief overview of RF sensing with an OPM was presented. This Section explores the underlying physics of RF OPMs in more detail. Fundamentally, an OPM is an ensemble of atoms with collective net magnetic moment $\boldsymbol{\mu}$ that interact with an external magnetic field $\mathbf{B}_{\text{Ext}}$ via the interaction Hamiltonian $\hat{H}_B = \boldsymbol{\mu} \cdot \mathbf{B}_{\text{Ext}}$. We first review the basic picture of the atom as a tuned oscillator introduced in Section 1.1. Then, we examine the quantum-mechanical underpinnings of these dynamics, including, the methods used to spin-polarize the atoms via optical pumping and the response of the atoms to incident light fields. Detailed modeling of the physics within the alkali vapor cell via the state-operator method will also be explored. Finally, we will derive the fundamental quantum mechanical noise floor of an RF OPM to understand its potential sensitivity.

2.1 Basic Physical Principles

2.1.1 The Atoms as a Tuned Oscillator

As mentioned in Section 1.2, when an external magnetic field $\mathbf{B}$ is applied to an atom with electronic spin $\mathbf{S}$, Larmor precession can result. To create an RF OPM, we control the applied field in Equation 1.1, which shall hereafter be referred to as the *bias field* and be denoted $\mathbf{B}_0$. By convention, the direction of the bias field is along the *longitudinal* direction of our magnetometer, which we denote as the z-direction, so $\mathbf{B}_0 = B_0\mathbf{e}_z$. The bias field sets the Larmor frequency such that it matches the RF frequency we wish to detect, giving $f_{RF} \approx f_L$. With the sensitive frequency set, we can detect external electromagnetic RF fields by their magnetic part $\mathbf{B}_{\mathrm{RF}}$, which will resonantly excite the Larmor resonance of the electronic spins of the atoms about the bias field under the following conditions:

1. The amplitude of the RF field $B_{RF} = |\mathbf{B}_{\mathrm{RF}}|$ must remain small compared to the bias field: $B_{\mathrm{RF}} \ll B_0$.

2. The magnetic field of the RF signal must have a part within the plane transverse to the longitudinal axis (the xy-plane), so $0 \leq \mathbf{B}_{\mathrm{RF}}/B_{\mathrm{RF}} \cdot \mathbf{e}_z < 1$ .This is because resonant spin precession takes place within the plane orthogonal to the bias field; only the part of the RF field in the plane transverse to the longitudinal axis will contribute to resonant excitation. For maximum sensitivity the RF field should be propagating along the longitudinal direction, so that the magnetic field is entirely within the transverse plane, and $(\mathbf{B}_{RF}/B_{RF}) \cdot \mathbf{e}_z = 0$

3. The atomic spin $\mathbf{S}$ must be highly polarized along the longitudinal axis. We will refer to the normalized spin vector $\mathbf{P} = \mathbf{S}/S$ as the *spin-polarization* vector, and its magnitude P as the spin-polarization. Thus for a spin polarized along the longitudinal direction, $P_z = \mathbf{P} \cdot \mathbf{e}_z \approx 1$.

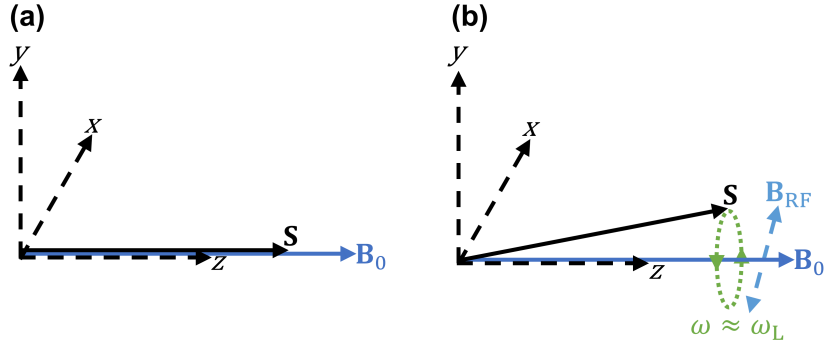

Figure 2.1: **(a)** Atomic spin **S** is polarized along the longitudinal axis defined by the applied bias field $\mathbf{B}_0$. **(b)** An RF signal with magnetic field $\mathbf{B}_{\mathrm{RF}} = B_{\mathrm{RF}} \cos(\omega t)\mathbf{e}_\perp$ where $\mathbf{e}_\perp$ is a unit vector in the transverse plane, resonantly drives Larmor resonance of the polarized atomic spin.

The nature of this project guarantees the first condition is met. For instance, using either naturally occurring isotope of rubidium for sensing at a frequency on the order of $10 - 100$ kHz, the bias field amplitude will be on the order of $1 - 10\,\mu$T. Fields in which we are interested have a magnitude in the pT range or below. Higher amplitude fields could easily be detected by existing inductive pick-up coil technology. The second condition can be met by physically rotating the transverse (xy) plane of the magnetometer into an orientation parallel to the RF magnetic field. The third condition can be met by polarizing the electron spins via optical pumping, as detailed in Section 2.2.2.

2.1.2 The Quantum Mechanical Picture

We may also view the dynamics of the atom from a quantum mechanical perspective. In an alkali atom, there is a single electron in the outermost valence shell. The energy level of this outermost electron is called the *principal* quantum number. Because the principal quantum number is set only by the position of the alkali on the periodic table, and remains unchanged in the dynamics we shall discuss, it is actually of little

importance to us. Of much greater interest is that this unpaired outermost electron has intrinsic *spin* angular momentum $\mathbf{S} = \frac{1}{2}\hbar\mathbf{e}_n$ where $\mathbf{e}_n$ is a general unit vector. Henceforth, the factor of $\hbar$ will be understood to be implied when discussing angular momenta, and we will simply write $\mathbf{S} = \frac{1}{2}\mathbf{e}_n$ and $S = \frac{1}{2}$. The projection of the electron spin along the bias field $m_S = \mathbf{S} \cdot \mathbf{e}_z$ is called the *spin* quantum number. In addition to spin, the electron has an angular momentum associated with its motion around the nucleus, denoted $\mathbf{L}$, which is called the *orbital* angular momentum. The magnitude of this orbital angular momentum ℓ, defined by the relation $L^2 = \ell(\ell+1)$ is called the *azimuthal* quantum number; it determines the orbital of the electron as it moves around the nucleus. The total angular momentum of the electron is given by the vector sum $\mathbf{J} = \mathbf{L} + \mathbf{S}$. The nucleus of the atom additionally has a spin denoted by $\mathbf{I}$, which is determined by the specific isotope in question. The vector sum of the nuclear spin with the electronic angular momentum produces the *total* spin denoted by $\mathbf{F}$ and expressed as $\mathbf{F} = \mathbf{I} + \mathbf{J}$.

We will consider the D_1 and D_2 alkali transitions, defined by the transition of the electron from the $\ell = 0$ to the $\ell = 1$ orbitals. For the ground state of this transition, $J = L + S = 1/2$. The excited state may have the electron spin either add to or subtract from the orbital angular momentum, giving $m_J = 1 \pm 1/2$ for $J = 1/2$ or $J = 3/2$. The former has lower energy and is referred to as the D_1 transition, while the latter has higher energy and is called the D_2 transition. The energy difference between the $J = 1/2$ and $J = 3/2$ excited states is called the *fine structure* of the atom. Finally, we must consider the total angular momentum F, for which the nuclear spin may further either add to or subtract from the total electron angular momentum. This leads to the splitting of the electron energy structure into further energy levels, which are called the *hyperfine* structure of the atom. The overall structure of the atomic energy levels is shown in Figure 2.2.

Each hyperfine energy mainfold has a further total of $2F+1$ sub-levels, called the *Zeeman* levels (or states) of the electron, which are determined by the projection of

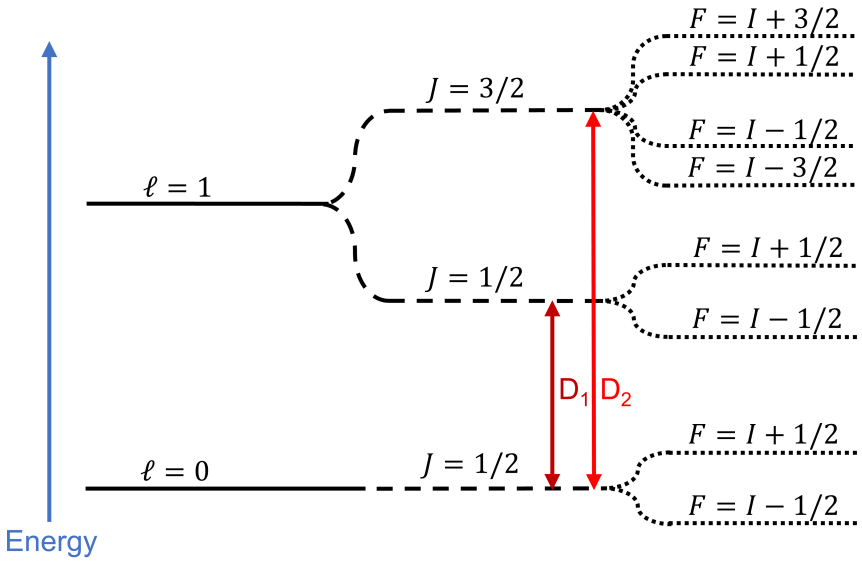

Figure 2.2: Energy level structure of the outermost electron of an alkali atom. Solid lines indicate the energy due to the orbital angular momentum, while dashed lines indicate the fine structure, and dotted lines show the hyperfine structure.

the total spin onto the bias field along the longitudinal axis $m_F = \mathbf{F} \cdot \mathbf{e}_z$. Without any magnetic bias field applied, these Zeeman levels are degenerate. When a bias field is applied, this degeneracy is lifted as the symmetry is broken by the bias field as it alters the energy levels of the spins within it. So long as the energy splitting between Zeeman levels in the bias field remains small compared to the energy difference between adjacent hyperfine manifolds (the hyperfine splitting), the energy splitting of the sub-levels is termed the *Zeeman effect*, for which the energy difference between adjacent states is approximately linear in the bias field, and given by

$$\Delta E_Z = \mu_B g_F B_0, \tag{2.1}$$

where $\mu_B = q_e \hbar / (2m_e) = 9.274 \times 10^{-24}\,\mathrm{J\,T^{-1}}$ is the *Bohr magneton*, $q_e = 1.602 \times 10^{-19}\,\mathrm{C}$ is the elementary charge, $m_e = 9.109 \times 10^{-31}\,\mathrm{kg}$ the mass of the electron, and g_F the *Lande g-factor* of the hyperfine transition. We can re-write Equation 2.1

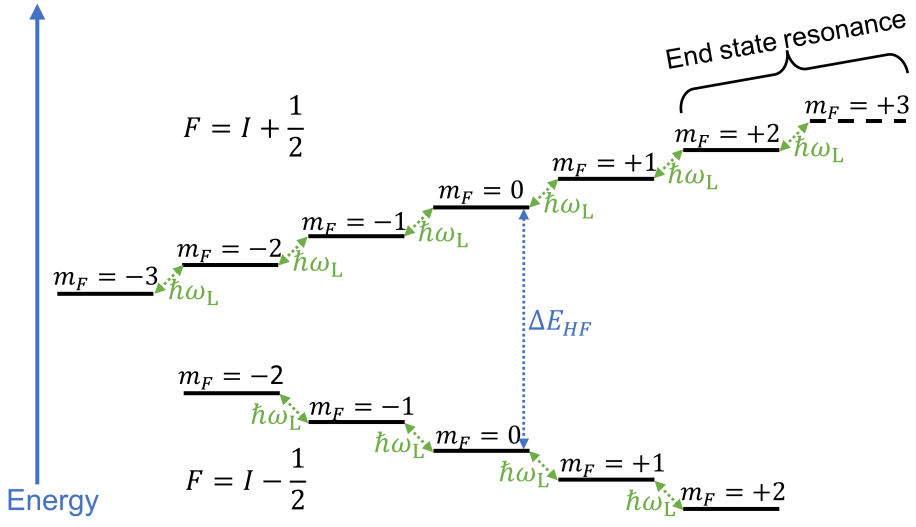

Figure 2.3: Zeeman energy levels of a nuclear spin 5/2 alkali atom in a nonzero bias field. The stretched state is highlighted by a dashed line. The end state resonance used for RF sensitivity used in this work is also shown.

in terms of the gyromagnetic ratio to find

$$\begin{aligned} \Delta E_Z &= \hbar \frac{q_e}{2m_e} g_F B_0 \\ &= \hbar \gamma B_0, \end{aligned} \tag{2.2}$$

where $\gamma = \gamma_e g_F$ is the gyromagnetic ratio, and $\gamma_e = q_e/2m_e = 2\pi \times 28.025$ GHz T^{-1} is the gyromagnetic ratio of a bare electron. Dropping the factor of $\hbar$, we find the angular frequency of transitions between adjacent Zeeman levels is

$$\begin{aligned} \omega &= \gamma B_0 \\ &= \omega_L. \end{aligned} \tag{2.3}$$

Equation 2.3 makes the picture of Larmor resonance presented previously clear from a quantum mechanical perspective: Larmor precession is simply resonance between Zeeman levels in the hyperfine manifold. A diagram of the Zeeman levels in a nonzero bias field for an $I = 5/2$ nuclear spin is shown in Figure 2.3.

When the spin is highly polarized along the z-axis as discussed previously, we know that $m_F = F_a = I + 1/2$ is at its maximum magnitude, and the state of the atoms in the hyperfine basis is $|F_a, m_F = F_a\rangle$. This is called the *stretched* state, because the spin is "stretched" along the longitudinal axis to the greatest possible extent. Of course a nearly resonant RF field will then induce resonance between adjacent Zeeman levels. In particular it will couple the the stretched state and the adjacent Zeeman level given by $|F_a, m_F = F_a - 1\rangle$. This *end-state transition* provides the physical basis of the magnetometer.

2.2 Detailed Atomic Dynamics

We have thus far considered the simple dynamics of an ideal single atom. Now we shift our attention to a more realistic picture of an *ensemble* of many atoms. We will denote the total number of atoms by N, and quantities such as the electron spin $\mathbf{S}$ and the total spin $\mathbf{F}$ will be taken to refer to the *ensemble average* of these quantities, given by $\mathbf{K} \to \mathbf{K} = \frac{1}{N}\sum_{i=1}^{N} \mathbf{K}_n$ where $\mathbf{K}$ is a general atomic angular momentum operator, and i refers to the i'th atom in the ensemble. This has the effect of increasing the total signal in proportion to N. For the $\sim 10^{13}$ atoms present in a $1\,\mathrm{cm}^3$ heated vapor cell, this provides the exquisite sensitivity we seek. On the other hand, interactions between alkali atoms, *buffer gas* atoms present for reasons explained below, and the glass walls of the vapor cell will degrade the sensitivity. Optical pumping and inclusion of a carefully selected type and amount of buffer gas will help ameliorate these effects.

2.2.1 Light-Atom Interactions and the Line Shape

The atoms within the ensemble will only have an appreciable interaction with an incident light-field when the optical frequency ν of the the light field is near an

atomic resonance and has a polarization capable of driving an allowed transition as determined by the selection rules. See Harris and Bertolucci (1989) for a review of the atomic selection rules [39]. An incident light-field that meets these criteria will transfer photons to the atoms at an absorption rate denoted by $R_{\mathrm{Abs}}(\nu)$, which is given by a sum over all possible allowed transitions

$$R_{\mathrm{Abs}}(\nu) = \sum_i \sigma_n(\nu)\Phi(\nu), \tag{2.4}$$

where $\sigma_i(\nu)$ is the photon absorption cross-section for the i'th allowed transition at frequency ν, and $\Phi(\nu)$ is the incident photon flux in photons per unit-time per unit-area. Photon flux is set by the power and spot size of the incident laser light. Modern semiconductor lasers as used in this work have a linewidth much smaller than those of the optical transitions they drive, and can be treated as approximately monochromatic. The response of the atoms to the incident light-field as captured by the absorption cross-section $\sigma_n(\nu)$ has a lower bandwidth limit set by the *natural lifetime* $\tau_{\mathrm{N}} = \frac{1}{2\pi\Gamma_{\mathrm{N}}}$, where Γ_{N} is the *natural linewidth* of the optical transition in question, which is a well measured quantity for the D_1 and D_2 transitions in all alkali species, and is summarized in Table A.2. The linewidth is then further broadened by various effects that couple the atoms to external degrees of freedom and increase decoherence. These include [25]:

1. **Pressure broadening**: Additional decoherence introduced by collisions between buffer gas particles and the alkali atoms will cause the optical linewidth to widen. This effect broadens an optical line by an amount Γ_{P} proportional to the density of buffer gas present. The name of the effect is due to the fact this density is typically specified by fill gas pressure when constructing a vapor cell. It will also cause a shift of the resonance center frequency $\Delta\nu_0(\mathrm{P})$. The total linewidth is a sum of the natural and pressure broadened lifetimes $\Gamma_{\mathrm{Tot}} = \Gamma_{\mathrm{N}} + \Gamma_{\mathrm{P}}$. Table A.3 gives the measured values for the pressure broadening and resonance frequency shift caused by nitrogen gas within the most

commonly utilized alkali species. The absorption of photons with resonant frequency ν_0 from a light-field at optical frequency ν is then a Lorentzian with FWHM linewidth Γ_{Tot} given by $[\Gamma_{\mathrm{Tot}}/(2\pi)]/[\Delta\nu^2+(\Gamma_{\mathrm{Tot}}/2)^2]$ where $\Delta\nu = \nu-\nu_0$ is the frequency shift from optical resonance. We may extend this result to also include a dispersive part that modifies the index of refraction of light moving through the vapor, given by $\Delta\nu/[\Delta\nu^2 + (\Gamma_{\mathrm{Tot}}/2)^2]$. Both the absorptive and dispersive terms can be expressed via a a single complex Lorentzian given by [77]

$$\mathcal{L}(\Delta\nu, \Gamma_{\mathrm{Tot}}) = \frac{1}{\pi}\frac{\Gamma_{\mathrm{Tot}}/2 + i\Delta\nu}{\Delta\nu^2 + (\Gamma_{\mathrm{Tot}}/2)^2}. \tag{2.5}$$

2. **Doppler Broadening**: An atom moving relative to a light-field with wave-vector $\mathbf{k}$ at velocity $\mathbf{v}$ will experience a Doppler shift in its frequency given by $\Delta\nu_{\mathrm{D}}(\mathbf{v}) = -\nu(\frac{\mathbf{v}}{c}\cdot\frac{\mathbf{k}}{k})$ where $c = 2.997925\times10^8$ m s^{-1} is the speed of light in a vacuum. The i'th atom will therefore see an effective resonance frequency that is dependent on its particular velocity $\mathbf{v}_i$. Because the atoms are in a heated vapor cell, they will have a range of thermal velocities determined by a three dimensional Maxwell-Boltzmann distribution. Thus the probability of $\mathbf{v}_i$ being within the volume-element d^3v in the three-dimensional velocity domain is given by

$$P(\mathbf{v})d^3v = \sqrt{\frac{m}{2\pi k_B T}}\exp\left(\frac{-m\mathbf{v}\cdot\mathbf{v}}{2k_B T}\right), \tag{2.6}$$

where $k_B = 1.381\times10^{-23}$ J K^{-1} is the Boltzmann constant, T is the temperature in Kelvin, and m is the mass of the alkali species in question. This distribution of possible velocities leads necessarily to a distribution of optical resonance frequencies via the aforementioned Doppler shift $\Delta\nu_D(\mathbf{v})$. The result is an effective broadening of the resonant line as atoms moving at different speeds are resonant at shifted frequencies. The associated distribution in optical frequency is in fact a Gaussian of the form [77]

$$\mathcal{G}(\Delta\nu, \Gamma_{\mathrm{G}}) = \frac{2\sqrt{\ln 2/\pi}}{\Gamma_{\mathrm{G}}}\exp\left(\frac{-4\ln 2\Delta\nu^2}{\Gamma_{\mathrm{G}}^2}\right), \tag{2.7}$$

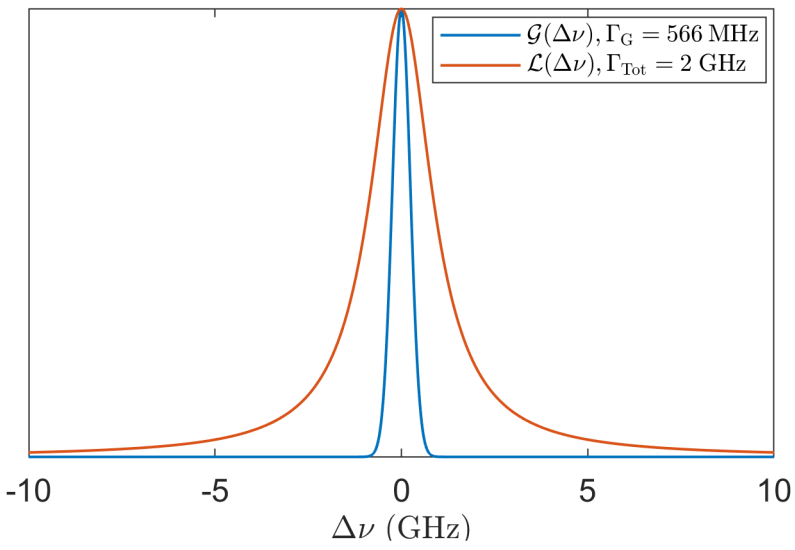

Figure 2.4: Comparison of Lorentzian profile due to pressure broadening with FWHM linewidth of $\Gamma_L = 2$ GHz, which is a realistic value for ~ 100 Torr of nitrogen buffer gas in a Rb cell, and a Gaussian profile due to Doppler broadening with FWHM of $\Gamma_G = 566$ MHz, which is a realistic value for ^{85}Rb at 100°C. Curves have been re-scaled to have the same on-resonance value for comparison.

where Γ_G is the FWHM of the distribution.

Regardless of the specifics, integrating the response of the atoms over all possible optical frequencies gives the constant [77, 25]

$$\int_0^\infty \sigma(\nu) d\nu = \pi r_e c f_{Res}, \tag{2.8}$$

where $r_e = 2.82$ fm is the so-called classical electron radius, and f_{Res} is the *oscillator strength* of the transition in question. For the D_1 transition, $f_{Res} \approx 1/2$, while for the D_2 transition, $f_{Res} \approx 2/3$. There are slight deviations from these idealized values due to perturbations to the exact dynamics caused by spin-orbit coupling, along with the interaction of the outermost alkali electron with electrons in the filled shells below it [64]. Exact measured values are given in Table A.2.

The natural linewidth in alkali atoms is on the order of $\Gamma_N \sim 10$ MHz, while the Doppler-broadened linewidth is on the order of $\Gamma_G \sim 100$ MHz. The pressure

broadened linewidth is of course determined by amount of buffer gas present. We intentionally use enough buffer gas such that the individual hyperfine transitions are not well-resolved to achieve a high efficiency of optical pumping, as discussed in Section 2.2.2. This leads to a pressure-broadened linewidth on the order of $\Gamma_{\mathrm{Tot}} \sim 1\,\mathrm{GHz}$. Thus pressure broadening is by far the dominant mechanism, and we can treat the atomic response to the incident light as a Lorentzian as given by the real part in Equation 2.5. The optical absorption then becomes

$$\sigma(\Delta\nu) = \pi r_{\mathrm{e}} c f_{\mathrm{Res}} \frac{\Gamma_{\mathrm{Tot}}/(2\pi)}{\Delta\nu^2 + (\Gamma_{\mathrm{Tot}}/2)^2}. \tag{2.9}$$

2.2.2 Optical Pumping

For the methods described in Section 2.1 to work, we must polarize the electron spin $\mathbf{S}$ along the longitudinal axis such that $P_z \approx 1$. To achieve this, many optical pumping schemes have been developed since the technique was initially invented in the 1950s, and many excellent works on the subject have been published. See, for instance "Optically Polarized Atoms" by Auzinsh et al. (2010) [13]. An excellent introduction specific to general magnetometry which considers optical pumping on the D_2 transition, along with the case of an arbitrarily polarized light-field, was given by Seltzer in his Ph.D. thesis [77]. This discussion will summarize sections of the latter relevant to our experiment. We simply need to put the atoms within the ensemble into the stretched state. To do so, we illuminate the ensemble with a "pump" or "pumping" light beam that is resonant with the D_1 transition in our alkali species of choice. Using the D_2 transition, we could only achieve half as much spin polarization, as shown by Seltzer (2008) [77]. Using rubidium as an example, this means a source at 795 nm. Semiconductor lasers at this wavelength (along with those of Potassium and Cesium) are readily available to use as a coherent light source.

The atoms will start out in a highly randomized state* that is distributed among the Zeeman levels by rapid collisions between atoms themselves and with the buffer gas and cell walls. Thus the spin-polarization P of the ensemble will be very small, and without well defined direction, giving $\mathbf{P} \cdot \mathbf{e}_z \approx 0$. When illuminated by the resonant light of the optical pumping beam, atoms in a lower energy states will be coherently excited to higher states, provided the polarization of the pumping light meets the selection rules imposed by the symmetries of the underlying dynamics. See Harris and Bertolucci (1989) for greater details [39]. Depending on the polarization of the pumping light, the atoms may do one of three things† in their interaction with the light-field

1. **$\boldsymbol{\sigma\pm}$ Transitions**: The atom may gain (+) or lose (−) a quantum of angular momentum to the light field, leading to a

$$\left|\ell = 0, J = 1/2, F = I \pm 1/2, m_F = m_F^{(0)}\right\rangle \rightarrow \left|\ell = 1, J = 1/2, F = I \pm 1/2, m_F = m_F^{(0)} \pm 1\right\rangle$$

   transition. This is caused by light with right(+) or left(−) circular polarization along the bias field, and is denoted a $\sigma\pm$ transition.

2. **$\boldsymbol{\pi}$ Transitions**: The atom may gain energy, but neither gain nor lose any angular momentum, leading to a

$$\left|\ell = 0, J = 1/2, F = I \pm 1/2, m_F = m_F^{(0)}\right\rangle \rightarrow \left|\ell = 1, J = 1/2, F = I \pm 1/2, m_F = m_F^{(0)}\right\rangle$$

   transition. This is caused by light with a linear polarization along the bias field, and is denoted a π transition.

*The exact state of the ensemble will in fact be given by a thermal distribution with polarization $P_{\mathrm{Th}} = \tanh\left(\frac{g_s \mu_B B}{2 k_B T}\right)$

†Technically, these cases only cover *single*-photon transitions. Multi-photon transitions which transfer multiple quanta and are subject to different selection rules are possible, but only become significant at higher light intensities than we will consider in this work.

A general elliptical polarization of the light field will drive a superposition of these transitions, which we will not consider here. For our purposes, we can simply illuminate the atoms with a light-field that is polarized to drive $\sigma+$ transitions. This can be achieved relatively easily using a birefringnet materiel cut to a proper thickness to cause a $\lambda/4$ delay in the phase between its fast (lower index of refraction) and slow (higher index of refraction) directions. Such a *quarter-wave plate* allows us to easily rotate an initially linearly polarized light source, such as that from a diode laser, into a circular polarization that will excite $\sigma\pm$ transitions. We use light with a right-hand circular polarization that drives $\sigma+$ transitions.

We now arrive at the reasons for the inclusion of a buffer gas: In a glass cell containing only alkali atoms, the thermal motion discussed in Section 2.2.1 will cause the atoms to quickly move to the walls of the cell. Upon collision with the cell walls, these alkali atoms will briefly adhere to the the inner glass surface of the cell, where complex interactions with the particles in the glass will quickly depolarize the spin. After the atom re-enters the volume of the cell, it will have lost all spin polarization, as illustrated in Figure 2.5.

We can model this process as simply treating all collisions of atoms within the cell as becoming completely depolarized [10, 77]. There are several ways to address this decoherence process. Coating the interior surfaces of the glass cell with certain organic compounds can effectively prevent alkali atoms from depolarizing after collisions with the walls. Seltzer gives a good overview in Chapter 5 of his thesis [77]. This approach typically limits the achievable alkali vapor density, as the organic coating would be irreversibly damaged when heated beyond its melting temperature. Another well established approach, which is used in this work, is to include a buffer gas that collides with the alkali atoms, slowing their diffusion to the cell walls. While spin-depolarizing collisions still occur between the buffer gas and alkali atoms as characterized by the cross-sections given in Table A.3, selection of a proper buffer gas species with a sufficiently low cross-section for such spin-destruction collisions

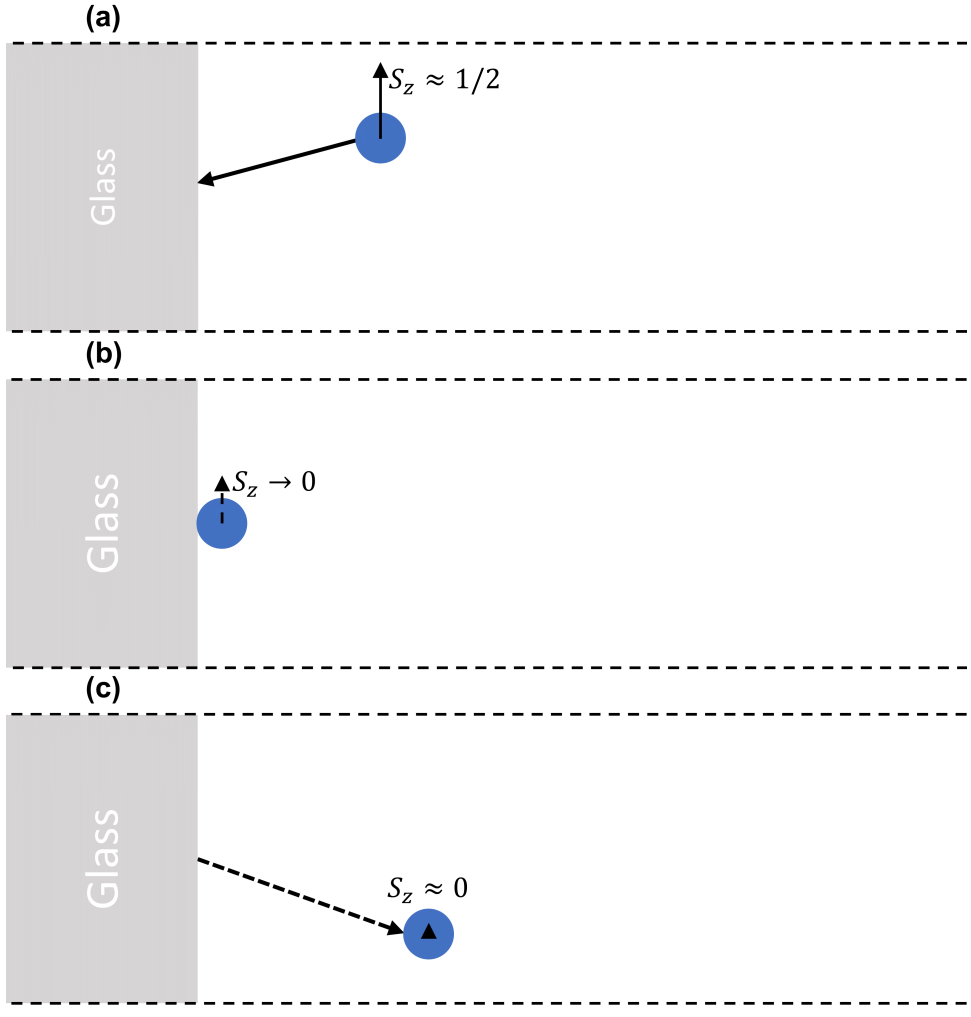

Figure 2.5: Collision of an alkali atom with the glass surface of the vapor cell. **(a)** An initially spin-polarized alkali atom within the volume is incident on the glass surface. **(b)** The atom briefly adheres to the glass, where complex interactions between the glass and alkali atoms quickly depolarizes the spin. **(c)** The alkali atom returns to the cell volume having lost its spin polarization.

at a properly selected density will lead to an overall depolarization rate much lower than would occur in its absence.

We also wish to include a *quenching* gas to prevent *radiation trapping*: a phenomenon that occurs when the photons of resonant light emitted by alkali atoms

decaying from their excited states are re-absorbed by adjacent alkali atoms before they can exit the vapor. Because the direction and polarization of these decay photons will be random, their absorption by neighboring alkali atoms will lead to additional decoherence that tends to randomize the state of the ensemble and degrade the average spin coherence. A detailed treatment of radiation trapping is beyond the scope of this work. See, for instance,"Radiation Trapping in Atomic Vapours" by Molisch and Oehry (1998) for a detailed treatment [65]. Franz (1968) demonstrated how to ameliorate the effect of radiation trapping via the inclusion of a *quenching gas* [35]. Typically a diatomic molecule, the quenching gas allows for the alkali atoms to quickly shed energy via complex interactions with the vibrational and rotational molecular degrees of freedom, allowing them return to their ground state without emitting resonant photons that would lead to radiation trapping. Within a Rb cell, diatomic nitrogen gas functions well as both a buffer and quenching gas due to its relatively small spin-destruction cross-section with Rb, and its high efficiency as a quenching gas. See Table A.3 for a comparison of the spin-destruction and quenching cross-sections between various alkali species and nitrogen buffer gas. Thus we use N_2 for both functions, and will refer to it as the buffer gas from now on, but it should be understood that it functions as a quenching gas as well.

There is one final benefit to the inclusion of a buffer gas: In its absence, the $F_{\mathrm{a,b}} = I \pm 1/2$ (+ for a, - for b) manifolds of the ground state of the D_1 transition are individually well resolved, as the Dopplar-broadened linewidth is smaller than the ground state hyperfine splitting. However, if we include sufficient buffer gas, the pressure broadening effect discussed in Section 2.2.1 causes the linewidth of the optical transition to become greater than the hyperfine energy splitting. In this regime, the laser simultaneously energetically addresses all transitions from both ground state hyperfine manifolds to the excited state. Then, the only liming factor is that the polarization of the light matches the selection rules required for a transition between any given Zeeman levels. The situation for pumping with $\sigma+$ light is shown

in Figure 2.6.

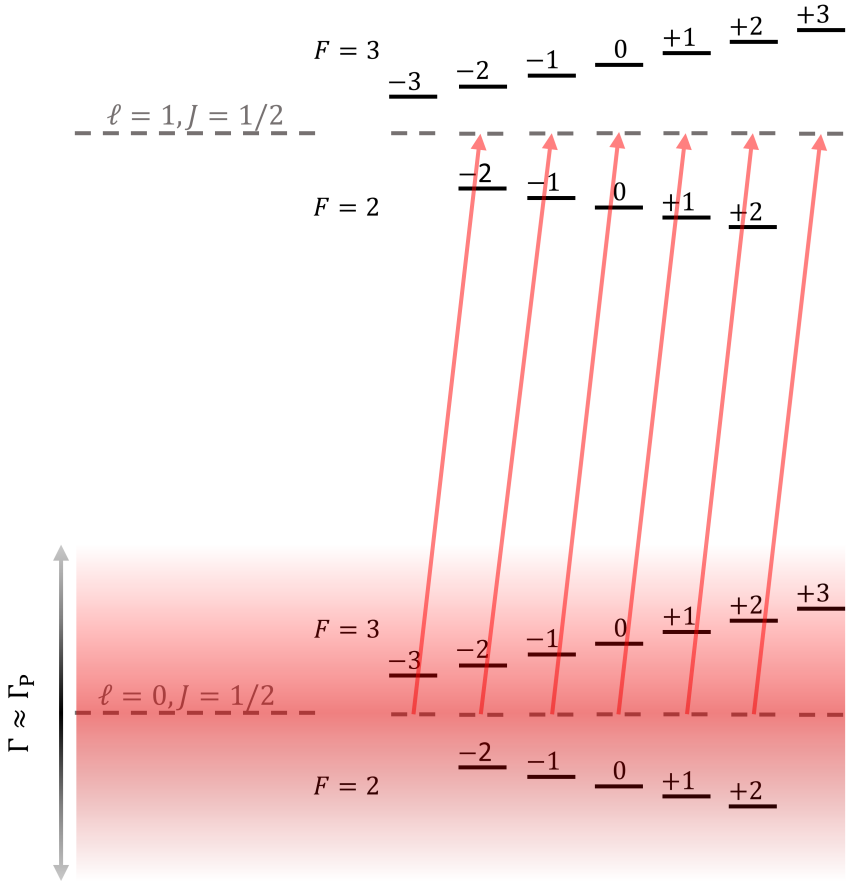

Figure 2.6: Optical pumping on the D_1 line in an $I = 5/2$ alkali atom such as ^{85}Rb using $\sigma+$ photons. All transitions are energetically allowed, because the optical linewidth of the transition is greater than the hyperfine splitting, meaning transitions between individual hyperfine manifolds are not well resolved. The polarization and the selection rules dictate that transitions must take place between an initial and final Zeeman state such that the atom gains +1 angular momentum.

Once in the excited state, the electron will decay back to the ground state, either by emitting photons at the rate $R_{\mathrm{Tot}} = 1/\tau_{\mathrm{Tot}} = \pi\Gamma_{\mathrm{Tot}}$, or by quenching as discussed above. In the former case, the emitted photon will carry a random $\sigma\pm$ or π polarization, and the atom may decay from its excited state Zeeman level to any Zeeman

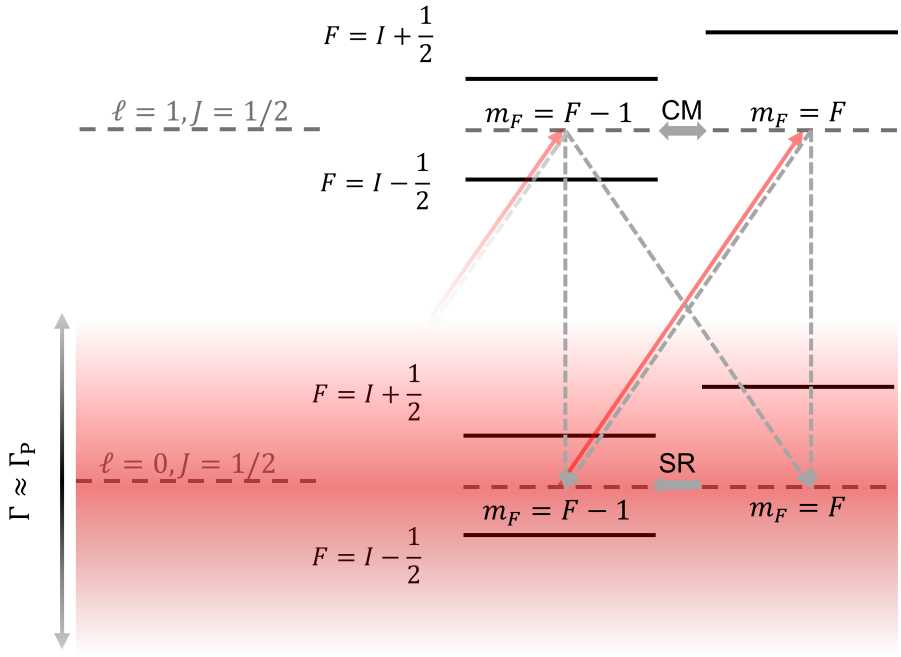

Figure 2.7: A close up view of optical pumping into the stretched state of an Alkali atom. Photons with $\sigma+$ polarization shown with red arrows drive the electron into the excited state. The atom then decays via spontaneous emission and quenching, shown by dashed gray arrows. Collisonal mixing (CM) is indicated by a gray double arrow, while spin relaxation processes (SR) indicated by a single-sided solid gray arrow, tend to degrade spin polarization.

level in the ground state that has the correct angular momentum m_F to allow the transition. A $\sigma\pm$ photon results from a $\Delta m_F = \mp 1$ decay, while a π photon is from a $\Delta m_F = 0$ decay, as required by the conservation of angular momentum. The relative probability for each type of transition is given by branching ratios captured by the Clebsch-Gordan coefficients. They can be found in reference tables [96]. The latter case of decay via quenching is both more complex from a basic physics perspective, and yet simpler for our purposes: the complex interactions between the vibrational and rotational degrees of freedom of the diatomic quenching gas molecule and the alkali electron quickly, which is to say on a time-scale much smaller than the natural lifetime, distributes atoms in the excited state uniformly between all Zeeman levels.

This results in a uniform probability of decay from the excited state to all allowed Zeeman levels in the ground state [77].

Whatever the mechanism, once atomic decay leads it to the stretched state $|F = F_a, m_F = F_a\rangle$, it can no longer absorb additional angular momentum from the pumping light-field, as it already has the maximum possible angular momentum along the longitudinal axis. Thus atoms in the stretched state are "dark" to the pumping light-field, as the selection rules prevent the absorption of any further photons. In the absence of relaxation mechanisms, the atoms in the ensemble will eventually collect in the stretched state. In reality, the spin-relaxing processes of spin-destruction and spin-exchange collisions will fight against the pumping process and tend to re-distribute the electrons among the Zeeman levels of the ground state. Nevertheless, properly balanced optical pumping will create and maintain an atomic ensemble that is nearly entirely in the stretched state, giving $P_z \approx 1$. Proper tuning can be achieved in a practical sense by setting the optical frequency to the center of the resonance, and adjusting the power to the minimize the RF linewidth, as discussed in Section 2.2.6.

2.2.3 The RF Atomic Response

Let us now consider the behavior of the spin when a bias field $\mathbf{B}_0 = B_0\mathbf{e}_z$ is applied. The treatment given here is taken from Sections 2 and 3 in the thesis of Seltzer [77], along with the discussion provided by Alexandrov and Vershovskiy (2013)[2], which are in turn drawn from the orignal work of Bloch (1946) [19]. As mentioned at the beginning of this Section, the atoms with magnetic moment $\boldsymbol{\mu} = \gamma\hbar\mathbf{S}$ interact with the magnetic field via the interaction Hamiltonian

$$\begin{aligned} \hat{H}_B &= \boldsymbol{\mu} \cdot \mathbf{B}_0 \\ &= \gamma\hbar\mathbf{S} \cdot \mathbf{B}_0. \end{aligned} \tag{2.10}$$

The evolution of the spin is then given by

$$\begin{aligned}\frac{d\mathbf{S}}{dt} &= \frac{i}{\hbar}[\hat{H}_B, \mathbf{S}] \\ &= i\gamma[\mathbf{S}\cdot\mathbf{B}_{\text{Ext}}, \mathbf{S}].\end{aligned} \tag{2.11}$$

Applying the angular momentum commutation relation $[S_i, S_j] = i\epsilon_{ijk}S_k$,[‡] where ϵ_{ijk} is the Levi-Civita symbol, allows us to reduce this to

$$\frac{d\mathbf{S}}{dt} = \gamma\mathbf{S}\times\mathbf{B}_0. \tag{2.12}$$

This is just the equation of motion of a classical dipole in an external field, and leads to Larmor precession as we might have expected. Now consider the addition of an RF field in the plane transverse to the z-direction, given by $\mathbf{B}_{\text{RF}} = B_{\text{RF}}\cos(\omega_{\text{RF}}t)\mathbf{e}_y$. This field can be written as the combination of two counter-rotating terms in the complex plane, given by

$$\tilde{B}_{\text{RF}} = \tfrac{1}{2}iB_{\text{RF}}\Big(e^{+i\omega_{\text{RF}}t} + e^{-i\omega_{\text{RF}}t}\Big). \tag{2.13}$$

Let us now transform into a coordinate system $[x', y', z]$ that *co-rotates* at $+\omega_{\text{RF}}$ about the longitudinal axis with the positively rotating portion of the RF field. In this frame, the co-rotating portion of the field is static, with a magnitude of $B_{\text{RF}}/2$, while the counter-rotating part is moving away at frequency $-2\omega_{\text{RF}}$. We can now make the so-called *rotating-wave approximation*, and assume that since the RF linewidth is very small compared to the RF frequency, $-2\omega_{\text{RF}}$ is very far from resonance, and the counter-rotating part can be neglected entirely. By applying vector transformation rules in the rotating frame, we find that the the bias field in the rotating frame is given by

$$\mathbf{B}_0' = \left(B_0 - \frac{\omega_{\text{RF}}}{\gamma}\right)\mathbf{e}_z. \tag{2.14}$$

[‡]Note that the Einstein summation is being followed here, and a sum over repeated indices is implied.

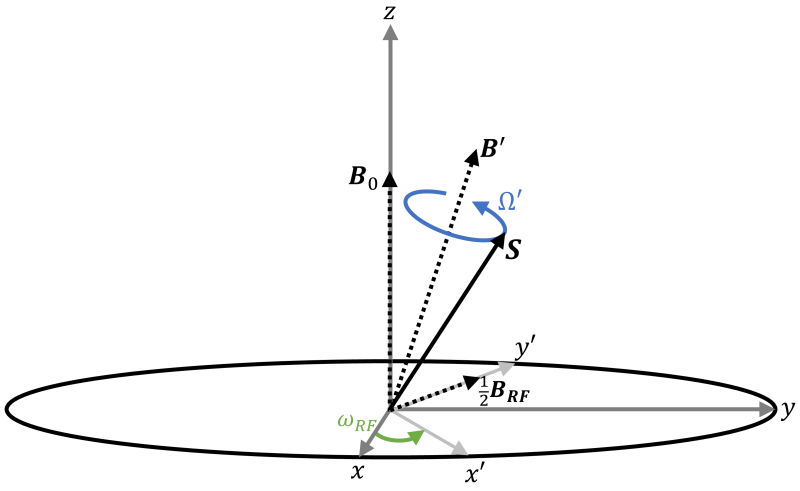

Figure 2.8: Dynamics of the rotating-wave approximation. In the rotating frame, the atoms experience a magnetic field $\mathbf{B}' = (-\Delta\omega/\gamma)\mathbf{e}_z + \frac{1}{2}B_{\mathrm{RF}}\mathbf{e}_{y'}$, about which they precess within the rotating frame at frequency $\Omega' = \sqrt{\Delta\omega_{\mathrm{RF}}^2 + (\gamma B_{\mathrm{RF}}/2)^2}$

Then the total magnetic field in the rotating frame is

$$\begin{aligned}\mathbf{B}' &= \frac{\omega_0 - \omega_{\mathrm{RF}}}{\gamma}\mathbf{e}_z + \tfrac{1}{2}B_{\mathrm{RF}}\mathbf{e}_{y'} \\ &= \frac{-\Delta\omega_{\mathrm{RF}}}{\gamma}\mathbf{e}_z + \frac{1}{2}B_{\mathrm{RF}}\mathbf{e}_{y'},\end{aligned} \tag{2.15}$$

where we have identified $B_0 = \omega_0/\gamma$ on the first line, and the shift from RF resonance is $\Delta\omega_{\mathrm{RF}} = \omega_0 - \omega_{\mathrm{RF}}$ on the second. Figure 2.8 illustrates the rotating-wave approximation. The Bloch Equation in the rotating frame is then [19, 77].

$$\frac{d\mathbf{S}'}{dt} = \gamma\mathbf{S}' \times \mathbf{B}' - \frac{1}{T_2}\mathbf{S}'_\perp - \frac{1}{T_1}(S_z - S_0)\mathbf{e}_z, \tag{2.16}$$

where $\mathbf{S}'_\perp = S'_x\mathbf{e}_{x'} + S'_y\mathbf{e}_{y'}$ is the transverse spin in the rotating frame, T_1 is the *longitudinal* spin-relaxation time, T_2 is the *transverse* spin-relaxation time, and

$$S_0 = \frac{sR_{\mathrm{OP}}}{2(R_{\mathrm{OP}} + R_{\mathrm{Rel}})} \tag{2.17}$$

is the equilibrium spin in the absence of the RF field, where $s \approx +1$ is the photon polarization for optical pumping with $\sigma+$ photons, R_{OP} is the optical pumping rate,

and R_{Rel} is a phenomenological parameter to characterize spin-relaxation processes. The equilibrium solution to Equation 2.16 is

$$S'_x = \frac{1}{2}\gamma B_{\mathrm{RF}} \frac{S_0 T_2}{1 + (\gamma B_{\mathrm{RF}}/2)^2 T_1 T_2 + \Delta\omega_{\mathrm{RF}}^2 T_2^2} \tag{2.18a}$$

$$S'_y = -\frac{1}{2}\gamma B_{\mathrm{RF}} \frac{S_0 \Delta\omega_{\mathrm{RF}} T_2^2}{1 + (\gamma B_{\mathrm{RF}}/2)^2 T_1 T_2 + \Delta\omega_{\mathrm{RF}}^2 T_2^2} \tag{2.18b}$$

$$S_z = \frac{S_0[1 + (\Delta\omega_{\mathrm{RF}} T_2)^2]}{1 + (\gamma B_{\mathrm{RF}}/2)^2 T_1 T_2 + \Delta\omega_{\mathrm{RF}}^2 T_2^2}. \tag{2.18c}$$

We transform back from the rotating frame to get the signal seen in the laboratory

$$\begin{aligned} S_x &= S'_x \cos(\omega_{\mathrm{RF}} t) - S'_y \sin(\omega_{\mathrm{RF}} t) \\ &= \frac{1}{2} S_0 \gamma B_{\mathrm{RF}} \frac{\cos(\omega_{\mathrm{RF}} t) T_2 + \Delta\omega_{\mathrm{RF}} T_2^2 \sin(\omega_{\mathrm{RF}} t)}{1 + (\gamma B_{\mathrm{RF}}/2)^2 T_1 T_2 + \Delta\Omega_{\mathrm{RF}}^2 T_2^2} \\ &= \frac{1}{2} S_0 \gamma B_{\mathrm{RF}} \left[\frac{1}{\sqrt{1 + (\gamma B_{\mathrm{RF}}/2)^2 T_1 T_2}} \frac{\pi\Gamma_{\mathrm{RF}}}{(\pi\Gamma_{\mathrm{RF}})^2 + \Delta\omega_{\mathrm{RF}}^2} \cos(\omega_{\mathrm{RF}} t) \right. \\ &\qquad \left. + \frac{\Delta\omega_{\mathrm{RF}}}{(\pi\Gamma_{\mathrm{RF}})^2 + \Delta\omega_{\mathrm{RF}}^2} \sin(\omega_{\mathrm{RF}} t) \right]. \end{aligned} \tag{2.19}$$

This is just the absorptive and dispersive parts of a Lorentzian curve with FWHM linewidth given by $2\pi\Gamma_{\mathrm{RF}}$, where the RF linewidth is

$$\Gamma_{\mathrm{RF}} = \frac{1}{\pi T_2} \sqrt{1 + \left(\tfrac{1}{2}\gamma B_{\mathrm{RF}}\right)^2 T_1 T_2}. \tag{2.20}$$

In the regime of small magnetic fields on the order of pT and below that we wish to measure, we will typically find that $2/(\gamma\sqrt{T_1 T_2}) \gg B_{\mathrm{RF}}$, so the second term under the radical related to power-broadening of the line can be neglected to find the demodulated response can be written in the form of a complex Lorentzian as defined by Equation 2.5

$$\tilde{S}_x^{(\mathrm{Demod})} \approx \tfrac{1}{2}\gamma S_0 B_{\mathrm{RF}} \mathcal{L}(\Delta\omega_{\mathrm{RF}}, \Gamma_{\mathrm{RF}}). \tag{2.21}$$

The nuclear spin will be "dragged" along by the motion of the electron spin due to the hyperfine interaction given by $\hat{H}_{\mathrm{HF}} = a_{\mathrm{HF}} \mathbf{I} \cdot \mathbf{S}$ where the a_{HF} is the hyperfine

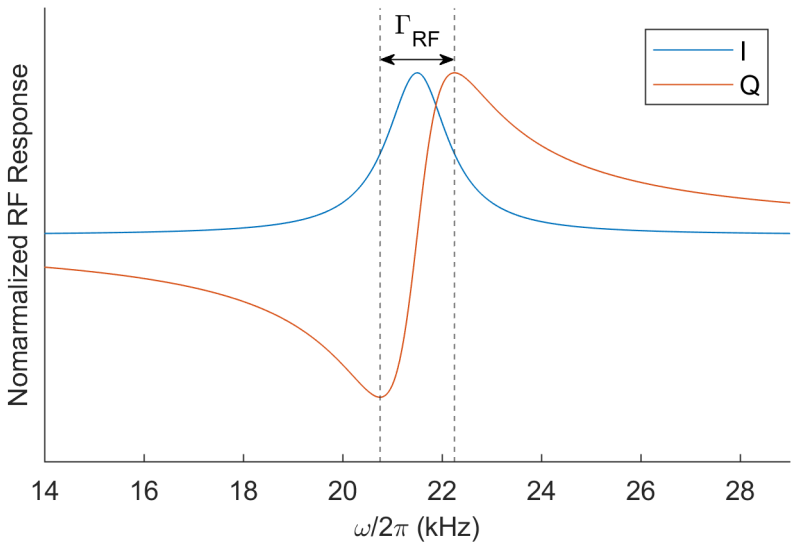

Figure 2.9: The normalized response of the atomic spins to an RF field. Both the in-phase (I) part describing absorption and the in-quadrature (Q) part describing dispersion are shown. Realistic values of $\omega_0 = 2\pi$ 21.5 kHz and $\Gamma_{\mathrm{RF}} = 1.5$ kHz were used to generate these curves.

coupling, which is available for all alkali atoms in the literature [5]. As a result, in the regime of high polarization in which we work, the nuclear spin precesses parallel to the electron spin and the *total* spin $\mathbf{F}$ precesses at a rate that is a factor of $q = 2I+1$ slower than that of a bare electron alone [77, 19]. Appelt et al. (1998) showed that the total spin-polarization due to an RF field $\mathbf{B}_{\mathrm{RF}} = B_{\mathrm{RF}}\cos(\omega_{\mathrm{RF}}t)\mathbf{e}_y$ with $B_{\mathrm{RF}} \ll B_0$ in the regime of high spin-polarization is [10]

$$P_x = \frac{F_x}{F} \approx \frac{1}{2}\gamma B_{\mathrm{RF}} \sin(\omega_{\mathrm{RF}}t)\mathrm{Re}\big(\mathcal{L}(\Delta\omega_{RF}, \Gamma_{\mathrm{RF}})\big). \tag{2.22}$$

where $\gamma = \gamma_e/q$ is the modified gyromagnetic ratio of the electron due to the drag of the nuclear spin.

Equation 2.22 provides a basis for understanding the atomic dynamics of the magnetometer, and tells us the line-shape we can expect to see. The RF linewidth Γ_{RF} will set the sensitive bandwidth about the center frequency that is set by B_0. As we shall see in Section 2.2.6, the sensitivity depends inversely on the RF linewidth.

On the other hand, the requisite bandwidth of the sensor depends on the application; it may be preferable to trade some sensitivity for a wider bandwith in some circumstances.

2.2.4 Full Dynamics and the State Operator

The phenomenological picture provided by the Bloch Equations is quite useful, but it relies on simply assuming the existence of a spin-relaxation rate R_{Rel}. To more fully characterize the dynamics of the atoms within the vapor cell, we need to consider the interactions experienced by the alkali atoms that contribute to spin-relaxation. These include collisions with other alkali atoms, collisions with buffer gas atoms, collisions with the cell walls, interaction with external magnetic fields, interaction with the light-fields of both the optical pumping and probing beams, and the hyperfine interaction. Solving the Schrödinger Equation directly is essentially impossible for this application, since we wish to characterize an ensemble of many atoms, and thus must include both the quantum mechanical evolution of the individual atoms as well as the statistical mixing implied by the ensemble approach. To do this, we employ the *state* or *density* operator approach. Ballentine (1998) provides a careful general treatment of the state operator in relation to the foundations of quantum mechanics [14]. A good overivew of the of the application of this method to atomic systems is provided by Auzinsh, Budker, and Rochester (2010) [13].

For a single particle with index $n \in [1, N]$, the quantum state can be written as the general ket $|\psi_n\rangle$. The state operator of this particle is given by the outer product $\rho_n = |\psi_n\rangle \langle\psi_n|$. The great utility of this approach becomes clear when we see that this representation makes it possible to take an ensemble average of the quantum states of the particles in the vapor cell

$$\rho = \frac{1}{N} \sum_{n=1}^{N} \rho_n. \tag{2.23}$$

The value of any ensemble averaged operator $\mathbf{K}$ is then simply given by taking the trace

$$\langle \mathbf{K} \rangle = \mathrm{Tr}[\rho \mathbf{K}] = \mathrm{Tr}[\mathbf{K}\rho]. \tag{2.24}$$

In fact, Equation 2.24 extends to finding the expected value of any observable. For our purposes, we shall be measuring the spin. The evolution of the atomic density operator is found by combining the Schrödinger Equation

$$i\hbar \frac{d}{dt} |\psi\rangle = \hat{H}_{\mathrm{Tot}} |\psi\rangle , \tag{2.25}$$

where $\hat{H}_{\mathrm{Tot}}$ is the total Hamiltonian, with Equation 2.23 which gives

$$\begin{aligned}
\frac{d}{dt}\rho &= \frac{d}{dt}\frac{1}{N}\sum_{n=1}^{N} |\psi_n\rangle \langle\psi_n| \\
&= \frac{1}{N}\sum_{n=1}^{N}\left[\left(\frac{d}{dt}|\psi_n\rangle\right)\langle\psi_n| + |\psi_n\rangle\left(\frac{d}{dt}\langle\psi_n|\right)\right] \\
&= \frac{1}{N}\sum_{n=1}^{N}\left[\frac{1}{i\hbar}\hat{H}_{\mathrm{Tot}}|\psi_n\rangle\langle\psi_n| - \frac{1}{i\hbar}|\psi_n\rangle\langle\psi_n|\hat{H}_{\mathrm{Tot}}\right] \\
&= \frac{1}{N}\frac{1}{i\hbar}\sum_{n=1}^{N}(\hat{H}_{\mathrm{Tot}}\rho_n - \rho_n\hat{H}_{\mathrm{Tot}}) \\
&= \frac{1}{i\hbar}\frac{1}{N}\sum_{n=1}^{N}[\hat{H}_{\mathrm{Tot}}, \rho_n] \\
&= \frac{1}{i\hbar}[\hat{H}_{\mathrm{Tot}}, \rho].
\end{aligned} \tag{2.26}$$

This result is known as the *Liouville*, or *master* equation. The latter moniker is used because it describes the population in the quantum states of the system as the ensemble evolves over time. Equation 2.26 is trace preserving; meaning it does not account for the effects of decoherence due to the coupling of the system to external degrees of freedom. However, we can extend the result to include the open quantum system dynamics of loss and decoherence from couplings of the spins to external degrees of freedom through various processes such as interactions with the optical pumping light-field, buffer gas particles, and the cell walls. The total master Equation including decoherence mechanisms for the evolution of a collection of atomic

spins within a vapor cell was complied by Appelt et al. (1998)[10]. It is given by

$$\frac{d}{dt}\rho^{(i)} = \frac{a_{\mathrm{HF}}^{(i)}}{i\hbar}[\mathbf{I}_i \cdot \mathbf{S}_i, \rho^{(i)}] + \frac{\mu_{\mathrm{B}} g_s^{(i)}}{i\hbar}[\mathbf{B}_{\mathrm{Ext}} \cdot \mathbf{S}_i, \rho^{(i)}] + R_{\mathrm{OP}}^{(i)}[\phi^{(i)}(1 + 2\mathbf{s} \cdot \mathbf{S}_i) - \rho^{(i)}] + R_{\mathrm{SD}}^{(i)}(\phi^{(i)} - \rho^{(i)}) + R_{\mathrm{SE}}^{(i)}[\phi^{(i)}(1 + 4\langle \mathbf{S}_i \rangle \cdot \mathbf{S}_i) - \rho^{(i)}] + D_i \nabla^2 \rho^{(i)}. \tag{2.27}$$

In this representation i indexes the alkali species. In general there may be multiple species. Of specific interest to us is natural rubidium, which has 72.15% ^{85}Rb and 27.85% ^{87}Rb. Although more general combinations such as Rb and Cs are also possible. The term $\phi^{(i)} = \rho^{(i)}/4 + \mathbf{S}_i \cdot (\rho^{(i)} \mathbf{S}_i)$ describes the part of the state that is purely nuclear spin-polarized via the hyperfine interaction, such that $\rho_i - \phi_i$ is the part with purely electron spin-polarization. The terms in the top row of Equation 2.27 describe respectively the hyperfine interaction between the nuclear and electronic spins of the alkali atoms, the interaction of the electron spin with the external magnetic field, and optical pumping of the electron spin at the rate $R_{\mathrm{OP}}^{(i)}$ by a light-field with polarization $\mathbf{s}$ as described above. The optical pumping term along with the terms in the second row describe the various spin-decoherence mechanisms that contribute to the overall spin relaxation rate. We will now examine them in more detail.

The fourth term describes collisions between the alkali atoms that destroy spin coherence, appropriately called spin-destruction collisions. These occur both with other alkali atoms and with buffer gas particles, with rates given by $R_{\mathrm{SD}}^{(ij)}$ The total spin destruction cross-section for the i'th alkali is then $R_{\mathrm{SD}}^{(i)} = \sum_j R_{\mathrm{SD}}^{(ij)}$.

The fifth term describes the effect of spin-exchange collisions arising from the spin-spin interaction during a collision. This coupling conserves the *total* spin $\mathbf{F}_1 + \mathbf{F}_2$ of the two particles. However, as the collisions take place on a time-scale much shorter than the hyperfine interaction, the electron spins of the two particles can be re-distributed between hyperfine levels during the interaction while leaving the nuclear spins unaffected. Figure 2.10 shows an example where the electron spins are interchanged, while conserving the total spin of the two particles. This leads to

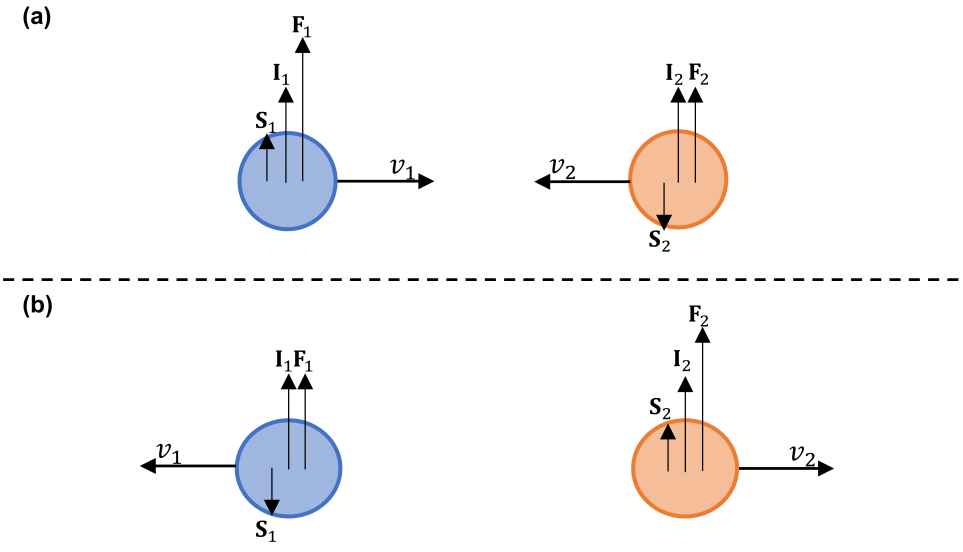

Figure 2.10: A spin-exchange collision between particle 1 shown in blue, and particle 2, shown in orange. **(a)** Two incoming particles with opposite electron spins collide. **(b)** After collision, electron the spins are reversed between the two particles, but the nuclear spins are unaffected, and the total spin $\mathbf{F}_1 + \mathbf{F}_2$ is conserved.

redistribution of the total spins among the various Zeeman levels, and thus degrades the spin-polarization of the ensemble. Spin-exchange can thus lead to significant spin depolarization. But it can be considerably ameliorated by properly balanced optical pumping, as discussed in Section 2.2.6.

The final term describes diffusion to the walls with diffusion constant D_i. Particles incident on the walls are fully depolarized, as discussed in Section 2.2.2.

These terms collectively describe the physical origins of the phenomenological spin relaxation rate R_{Rel}. The RF linewidth of the end state transition is determined by all of them. The state operator approach enables us to effectively model the detailed dynamics of the atoms within the vapor by solving solving the differential equation given by Equation 2.27. To make practical use of the state operator approach, we must first choose a complete basis $\{|n\rangle\}$ in which to represent the state operator as a matrix with components given by $\rho^{(i)}_{n,m} = \langle n| \rho^{(i)} |m\rangle$. The basis of total angular mo-

mentum states $\{|F, m_F\rangle\}$ is approximately orthonormal in the regime of linear Zeeman splitting, making it an appropriate appropriate choice for modeling the atomic dynamics for our applications. Because there are $N_Z = 2(2I+1)$ total Zeeman levels, the state operator can be represented as a $N_Z \times N_Z$ matrix, with components indexed by the total angular momentum F and its longitudinal projection m_F, so the matrix becomes $\rho^{(i)}_{n,m} = \langle F, m_F| \rho^{(i)} |F', m'_F\rangle$. Recall that $F_a = I + 1/2$ is the total angular momentum of the upper hyperfine manifold, with a total of $N_a = 2F_a + 1$ Zeeman levels while $F_b = I - 1/2$ is the total angular momentum of the lower hyperfine manifold with $N_b = 2F_b + 1$ total Zeeman levels. We will use the convention that $\rho^{(i)}_{1,1} = |F_b, m_F = -F_b\rangle \langle F_b, m_F = -F_b|$, $\rho^{(i)}_{2,2} = |F_b, m_F = -F_b + 1\rangle \langle F_b, m_F = -F_b + 1|$, up to $\rho^{(i)}_{N_b,N_b} = |F_b, m_F = +F_b\rangle \langle F_b, m_F = +F_b|$. After this, we start over with states in the upper hyperfine manifold, so $\rho^{(i)}_{(N_b+1),(N_b+1)} = |F_a, m_F = -F_a\rangle \langle F_a, m_F = -F_a|$, and then the angular momentum once again increases down the diagonal as we iterate through the Zeeman levels of the upper hyperfine manifold, so $\rho^{(i)}_{(N_b+2),(N_b+2)} = |F_a, m_F = -F_a + 1\rangle \langle F_a, m_F = -F_a + 1|$, all the way up to $\rho^{(i)}_{(N_b+N_a),(N_b+N_a)} = |F_a, m_F = +F_a\rangle \langle F_a, m_F = +F_a|$, where $N_b + N_a = N_Z$. An example of such a matrix for an $I = 5/2$ alkali species such as ^{85}Rb is given in Equation 2.28.

$$\rho = \begin{bmatrix} \overbrace{\begin{matrix} \rho_{1,1} & \rho_{1,2} & \rho_{1,3} & \rho_{1,4} & \rho_{1,5} \\ \rho_{2,1} & \rho_{2,2} & \rho_{2,3} & \rho_{2,4} & \rho_{2,5} \\ \rho_{3,1} & \rho_{3,2} & \rho_{3,3} & \rho_{3,4} & \rho_{3,5} \\ \rho_{4,1} & \rho_{4,2} & \rho_{4,3} & \rho_{4,4} & \rho_{4,5} \\ \rho_{5,1} & \rho_{5,2} & \rho_{5,3} & \rho_{5,4} & \rho_{5,5} \end{matrix}}^{\rho_b} & \begin{matrix} \rho_{1,6} & \rho_{1,7} & \rho_{1,8} & \rho_{1,9} & \rho_{1,10} & \rho_{1,11} & \rho_{1,12} \\ \rho_{2,6} & \rho_{2,7} & \rho_{2,8} & \rho_{2,9} & \rho_{2,10} & \rho_{2,11} & \rho_{2,12} \\ \rho_{3,6} & \rho_{3,7} & \rho_{3,8} & \rho_{3,9} & \rho_{3,10} & \rho_{3,11} & \rho_{3,12} \\ \rho_{4,6} & \rho_{4,7} & \rho_{4,8} & \rho_{4,9} & \rho_{4,10} & \rho_{4,11} & \rho_{4,12} \\ \rho_{5,6} & \rho_{5,7} & \rho_{5,8} & \rho_{5,9} & \rho_{5,10} & \rho_{5,11} & \rho_{5,12} \end{matrix} \\ \begin{matrix} \rho_{6,1} & \rho_{6,2} & \rho_{6,3} & \rho_{6,4} & \rho_{6,5} \\ \rho_{7,1} & \rho_{7,2} & \rho_{7,3} & \rho_{7,4} & \rho_{7,5} \\ \rho_{8,1} & \rho_{8,2} & \rho_{8,3} & \rho_{8,4} & \rho_{8,5} \\ \rho_{9,1} & \rho_{9,2} & \rho_{9,3} & \rho_{9,4} & \rho_{9,5} \\ \rho_{10,1} & \rho_{10,2} & \rho_{10,3} & \rho_{10,4} & \rho_{10,5} \\ \rho_{11,1} & \rho_{11,2} & \rho_{11,3} & \rho_{11,4} & \rho_{11,5} \\ \rho_{12,1} & \rho_{12,2} & \rho_{12,3} & \rho_{12,4} & \rho_{12,5} \end{matrix} & \overbrace{\begin{matrix} \rho_{6,6} & \rho_{6,7} & \rho_{6,8} & \rho_{6,9} & \rho_{6,10} & \rho_{6,11} & \rho_{6,12} \\ \rho_{7,6} & \rho_{7,7} & \rho_{7,8} & \rho_{7,9} & \rho_{7,10} & \rho_{7,11} & \rho_{7,12} \\ \rho_{8,6} & \rho_{8,7} & \rho_{8,8} & \rho_{8,9} & \rho_{8,10} & \rho_{8,11} & \rho_{8,12} \\ \rho_{9,6} & \rho_{9,7} & \rho_{9,8} & \rho_{9,9} & \rho_{9,10} & \rho_{9,11} & \rho_{9,12} \\ \rho_{10,6} & \rho_{10,7} & \rho_{9,10} & \rho_{10,9} & \rho_{10,10} & \rho_{10,11} & \rho_{10,12} \\ \rho_{11,6} & \rho_{11,7} & \rho_{11,8} & \rho_{11,9} & \rho_{11,10} & \rho_{11,11} & \rho_{11,12} \\ \rho_{12,6} & \rho_{12,7} & \rho_{12,8} & \rho_{12,9} & \rho_{12,10} & \rho_{12,11} & \rho_{12,12} \end{matrix}}^{\rho_a} \end{bmatrix} \tag{2.28}$$

Entries on the diagonal in the matrix representation of ρ in Equation 2.28 represent the normalized relative population of the Zeeman levels. The region highlighted by the blue dashed line in the upper left corner of the matrix representation of ρ in Equation 2.28 shows the sub-matrix ρ_b for the lower hyperfine manifold with $F = F_b = I - 1/2 = 2$, while the region highlighted by the red dashed line shows the sub-matrix ρ_a representing the upper hyperfine manifold with $F = F_a = I + 1/2 = 3$. Off-diagonal entries within these blocks describe coherence between the Zeeman levels within a single manifold, such as those induced by the RF field. Entries outside the blocks describe coherence between the upper and lower hyperfine manifolds, such as would be introduced by a driving field with energy equal to the hyperfine splitting. For instance, in ^{85}Rb, the $|F = F_b, m_F = 0\rangle \leftrightarrow |F = F_a, m_F = 0\rangle$ "clock" transition is at approximately 3 GHz, and the coherence induced by a such a driving field is captured by $\rho_{3,9}$ and $\rho_{9,3}$.

To calculate the evolution of $\rho_{n,m}$ as a function of time, we must calculate an

appropriate representation of $\mathbf{B}_{\text{Ext}}$, and $\mathbf{s}$. They can both be represented as three-dimensional vectors $\mathbf{V} = [V_x, V_y, V_z]$ relative to their x, y, and z components. For our optical pumping scheme, we have the particularly simple arrangement of $\mathbf{s} \approx \mathbf{e}_z = [0, 0, 1]$. The external magnetic field will be a combination of the bias field and an RF magnetic field in the transverse plane, so $\mathbf{B}_{\text{Ext}} = B_0\mathbf{e}_z + B_{\text{RF}}\cos(\omega_{\text{RF}}t)\mathbf{e}_y = [0, B_{\text{RF}}\cos(\omega_{\text{RF}}t), B_0]$.

We must also find the representations of the angular momentum operators $\mathbf{F}, \mathbf{S}, \mathbf{I}$ in this basis. They will take the form of $N_Z \times N_Z \times 3$ vector-operators that can be represented as three-dimensional arrays. An appropriate representation of their components is most conveniently found by making a change of basis from the [x,y,z] basis to the so called *spherical* basis given by the coordinate transformation

$$\begin{aligned} \mathbf{e}_0 &= \mathbf{e}_z \\ \mathbf{e}_\pm &= \mp\frac{1}{\sqrt{2}}\mathbf{e}_x - \frac{i}{\sqrt{2}}\mathbf{e}_y. \end{aligned} \tag{2.29}$$

This basis corresponds to the photon polarization of optical pumping, as a photon with π polarization will have a polarization-projection of unity along the $\mathbf{e}_0$ direction, while photons with $\sigma_\pm$ polarization will have polarization-projections of unity along the $\mathbf{e}_\pm$ axes respectively. Because this basis respects the inherent spherical symmetry of the system, it also allows us to calculate the components of the general angular momentum operator $\mathbf{K} = \hat{K}_0\mathbf{e}_0 + \hat{K}_+\mathbf{e}_+ + \hat{K}_-\mathbf{e}_-$. This operator has matrix components given by

$$\langle F, m_F | \mathbf{K} | F', m'_F \rangle = \sum_q \langle F, m_F | \hat{K}_q | F', m'_F \rangle \mathbf{e}_q, \tag{2.30}$$

where $q = 0, \pm 1$ is the *spherical index* of the transition. In the spherical basis, we know the action of the operators $\hat{K}_q$ on the basis states $\{|K, m_K\rangle\}$

$$\begin{aligned} \hat{K}_0 |K, m_K\rangle &= m_K |K, m_K\rangle \\ \hat{K}_\pm |K, m_K\rangle &= \sqrt{K(K+1) - m_K(m_K \pm 1)}\, |K, m_k \pm 1\rangle, \end{aligned} \tag{2.31}$$

since the z-component is the same as the $q = 0$ operator, and the $q = \pm 1$ operators are simply angular momentum ladder operators. Equation 2.31 makes calculation of the components $F_{n,m}$ particularly easy in the spherical basis

$$\begin{aligned} \langle F, m_F | \hat{F}_0 | F', m'_F \rangle &= m'_F \delta_{F,F'} \delta_{m_F, m'_F} \\ \langle F, m_F | \hat{F}_\pm | F', m'_F \rangle &= \sqrt{F'(F'+1) - m'_F(m'_F \pm 1)} \delta_{F,F'} \delta_{m_F, m'_F \pm 1} \end{aligned}, \tag{2.32}$$

where $\delta_{n,m}$ is the Kroneker delta. The final key to calculating the all the components of the $\mathbf{F}$ comes from the the Wigner-Eckhart theorem [13]

$$\langle F, m_F | \hat{K}_q | F', m'_F \rangle = \langle F', m'_F, 1, q | F, m_F \rangle \langle F | |\mathbf{K}| | F' \rangle , \tag{2.33}$$

where $\langle F', m_{F'}, 1, q | F, m_F \rangle$ is the Clebsch-Gordan coefficient of the transition, and $\langle F | |\mathbf{K}| | F' \rangle$ is the *reduced* matrix element of the transition that depends only on the starting and ending values of F and not on the spherical index q. As mentioned earlier, Clebsch-Gordan coefficients are tabulated in various references [96], or they can be computed as discussed by Auznish, Budker, and Rochester [13]. Thus the problem can be solved by computing the reduced matrix element $\langle F, m_F | |\mathbf{F}| | F, m'_F \rangle$ using Equation 2.31 and the Winger-Eckhart theorem (Eq. 2.33). Note that the operator $\mathbf{F}$ cannot couple the $F = F_a$ and $F = F_b$ manifolds, as it is inherently diagonal in the basis of its own eigenstates. Then we can compute the rest of the matrix elements using the reduced-matrix element and the appropriate Clebsch-Gordan coefficients as prescribed by the Wigner-Eckhart theorem (Eq. 2.33).

With $F_{n,m}$, known it is sufficient to calculate either of $I_{n,m}$ or $S_{n,m}$, as in the ground state $\mathbf{L} = 0$, so $\mathbf{F} = \mathbf{I} + \mathbf{S}$ and thus the difference gives final unknown operator. We will calculate the the electron-spin operator $\mathbf{S}$. This is a bit more involved. It can be broken into finding components within the $F = F' = F_{a,b}$ manifolds, and those that couple the $F_{a,b}$ and $F' = F_{b,a}$ manifolds. The former can be computed using the ratio of matrix elements given by

$$\frac{\langle F_{a,b} | \mathbf{S} | F_{a,b} \rangle}{\langle F_{a,b} | \mathbf{F} | F_{a,b} \rangle} = \pm \frac{1}{2I+1}, \tag{2.34}$$

where the positive sign corresponds to $F = F_a$ and the negative sign is for $F = F_b$. Thus Equation 2.34 and the already known values $\langle F| \, |\mathbf{F}| \, |F\rangle$ give the components of $\mathbf{S}$ for which $F = F'$. For the terms that couple the two manifolds, we must expand the coupled basis $\{|F, m_F\rangle\}$ in terms of electron and nuclear spin states using the Clebsh-Gordon coefficients

$$|F, m_F\rangle = \sum_{m_I} \sum_{m_S} \langle I, m_I, S = \tfrac{1}{2}, m_S | F, m_F\rangle \, |I, m_I, S, m_S\rangle \, . \tag{2.35}$$

Utilizing Equation 2.35 and operating with $\hat{S}_0$ gives

$$\begin{aligned} \langle F, m_F| \, \hat{S}_0 \, |F', m'_F\rangle = \sum_{m_I, m_S} & m_s \langle I, m_I, S = \tfrac{1}{2}, m_S | F, m_F = m_I + m_S\rangle \\ & \times \langle I, m_I, S = \tfrac{1}{2}, m_S | F', m'_F = m_I + m_S\rangle. \end{aligned} \tag{2.36}$$

Setting $F = F_{a,b}$, $F' = F_{b,a}$ and $m_F = m'_F = 0$, then combing the result with the Wigner-Eckhart theorem (Eq. 2.33) gives the result we seek

$$\begin{aligned} \langle F_{a,b}| \, \hat{S}_0 \, |F_{b,a}\rangle = \frac{1}{2\langle F_{a,b}, 0, 1, 0 | F_{a,b}, 0\rangle} \Big(& \langle I, -\tfrac{1}{2}, \tfrac{1}{2}, \tfrac{1}{2} | F_a, 0\rangle \langle I, -\tfrac{1}{2}, \tfrac{1}{2}, \tfrac{1}{2} | F_b, 0\rangle \\ & - \langle I, \tfrac{1}{2}, \tfrac{1}{2}, -\tfrac{1}{2} | F_a, 0\rangle \langle I, \tfrac{1}{2}, \tfrac{1}{2}, -\tfrac{1}{2} | F_b, 0\rangle \Big). \end{aligned} \tag{2.37}$$

Equations 2.36, 2.37, and the Winger-Eckhart theorem (Eq. 2.33) again give us the recipe to compute all the elements $S_{n,m}$ of the electron-spin operator. Then we also have the nuclear-spin operator from

$$I_{n,m} = F_{n,m} - S_{n,m}. \tag{2.38}$$

Note that since the spin-operators are vector operators, all three spherical components $\hat{K}_q$ must be calculated for each. From here we may either rotate the operators back into the $[x, y, z]$ basis, or simply rotate any input vectors such as $\mathbf{B}_{\text{Ext}}$ into the spherical basis for the computation.

With the operators in hand, we only need the prefactors to compute the state

evolution from Equation 2.27. The electron g-factor is simply $g_s \approx 2$. The spin-exchange and spin-destruction rates are given by

$$R^{(ij)}_{\mathrm{SD(SE)}} = n_j \sigma^{(ij)}_{\mathrm{SD(SE)}} \langle v_{ij} \rangle \,, \tag{2.39}$$

where $R_{\mathrm{SD(SE)}}$ is the spin-destruction(spin-exchange) rate for the i'th alkali interacting with the j'th species in the cell, n_j is the density of the j'th species with which the alkali interacts, $\sigma_{\mathrm{SD(SE)}}$ is the cross-section of spin-destruction(spin-exchange) interactions between the i'th alkali and j'th species, and $\langle v_{ij} \rangle$ is the average relative velocity between the two particles due to their thermal motion. Note that spin-exchange collisions only take place between alkali atoms in our system.[§] In contrast spin-destruction collisions occur between all particles interacting within the vapor cell. The alkali density can be computed from the cell temperature using the formula provided in Appendix A. If there is a temperature gradient within the cell, as there typically is, then the minimum temperature of the cell will set the alkali density, as alkali atoms will tend to preferentially condense there. The spin-destruction(spin-exchange) cross-sections can be found in the literature, and are summarized in Table A.3. The relative thermal motion is found by considering the joint Maxwell-Boltzmann distribution for the thermal motion of the two species. It turns out to be

$$\langle v_{ij} \rangle = \sqrt{\frac{8 k_B T}{\pi \mu_{ij}}} \tag{2.40}$$

where $\mu_{ij} = m_i m_j / (m_i + m_j)$ is the *reduced mass* of the two species and T is the temperature. The optical pumping rate is set by the normalized photon absorption rate given by Equation 2.8, and the intensity of the optical pumping beam. It is typically on the order of 1000 s^{-1}.

Finally, to treat the diffusion term, we can re-cast this part of the master Equation in terms of polarization by taking the expectation values for the spin-polarization on

[§]Other species such as noble gas atoms can also take part in spin-exchange collisions, but we do not use them in this work.

both sides

$$\begin{aligned}\frac{\partial}{\partial t}\mathrm{Tr}\big[\rho(\mathbf{S}/S)\big] &= D\nabla^2\mathrm{Tr}\big[\rho(\mathbf{S}/S)\big] \\ \frac{\partial}{\partial t}\langle\mathbf{P}\rangle &= D\nabla^2\langle\mathbf{P}\rangle\,.\end{aligned} \tag{2.41}$$

We use a nearly cubic cell with a length of d on each side. Equation 2.41 is a diffusion equation that is straightforward to solve by separation of variables using the boundary conditions that the spins are highly polarized at the center of the cell via optical pumping, so $P_0 = \langle\mathbf{P}(0,0,0,t)\rangle \approx 1$, while the polarization at the walls is zero, so
$\langle\mathbf{P}(\pm d/2, y, z, t)\rangle = \langle\mathbf{P}(x, \pm d/2, z, t)\rangle = \langle\mathbf{P}(x, y, \pm d/2, t)\rangle = 0$. The solution is

$$\langle\mathbf{P}(x,y,z,t)\rangle = \sum_{n_x,n_y,n_z} P_0^{(n_x,n_y,n_z)} \cos\left(\frac{n_x\pi x}{d}\right)\cos\left(\frac{n_y\pi y}{d}\right)\cos\left(\frac{n_z\pi z}{d}\right)e^{-t/R_{\mathrm{Wall}}}, \tag{2.42}$$

where n_μ is an integer with $\mu \in \{x, y, z\}$, $P_0^{(n_x,n_y,n_z)}$ is the indexed amplitude of the diffusion modes, and

$$R_{\mathrm{Wall}} = 3D\left(\frac{\pi}{d}\right)^2 \tag{2.43}$$

is the rate of wall collisions. The diffusion constant scales linearly with the density of the buffer gas in the cell, and is specified relative to the value at a reference pressure (and thus density) value D_0. For a fill pressure of $P_{\mathrm{N_2}}$ of $\mathrm{N_2}$ at $T_{\mathrm{Fill}} \sim 0°\mathrm{C}$, we can use the ideal gas law to find that the density is $n_{N_2} = P_{\mathrm{N_2}}/(k_B T)$. Therefore the diffusion constant can be calculated from the reference value at 0°C and 1 amg density found in Table A.3, giving $D = D_0(n_0/n_{N_2})$ where n_0 is the Loschmidt constant defined in Appendix A. Using this, we can find the diffusion rate from the lowest order diffusion mode to be $R_{\mathrm{Wall}} \approx 2.6\,\mathrm{s}^{-1}$. This is a good approximation to the total diffusion, and is negligible compared to the other broadening mechanisms, so we will henceforth drop the diffusion term from our model.

We now have all the tools to model the detailed dynamics of the alkali ensemble as it evolves in the vapor cell. For simulations carried out in this work, a framework was built in *MatLab*. It takes in an initial state ρ_0, the Alkali speices, the buffer

gas species and their fill pressures, the cell temperature, and the optical pumping rate. From this, it finds tabulated literature values and computes spin-exchange and spin-destruction rates and the spin operators for the given alkali species, the nuclear spin of which will set the size of the matrices required. All input vectors are rotated into the spherical basis before the calculation. The evolution is found by implementing Equation 2.27 directly using a solver for differential equations included in *MatLab*. In most cases the initial state ρ_0 is not of great importance, as we seek the equilibrium behavior, and any initial state will converge to it. It is often convenient to start with the stretched state $\rho_{\mathrm{S}} = |F = F_a, m_F = +F_a\rangle \langle F = F_a, m_F = +F_a|$ or the maximally mixed state $\rho_{\mathrm{M}} = \frac{1}{N_Z}\mathbb{I}$ where $\mathbb{I}$ is the identity matrix. Then we can obtain $\rho(t)$, and from it, compute the value of any observable as a function of time. We are particularly interested in the transverse spin-polarization $F_x = \mathrm{Tr}[\hat{F}_x\rho(t)]$, which corresponds to what we measure, as will be seen in the next Section.

2.2.5 Measuring Atomic Polarization

To measure the RF field, we wish to measure the transverse spin-polarization. To accomplish this, we utilize an atom-light interaction within the vapor cell: the Faraday effect. Linearly polarized light passing through a medium parallel to an a magnetic field **B** will experience a rotation of its polarization vector by an angle β given by

$$\beta = \mathcal{V}dB. \tag{2.44}$$

Where $\mathcal{V}$ is the *Verdet* constant of the medium, and d is the distance the light travels through the it. Figure 2.11 illustrates the Faraday effect as it rotates the polarization of a propagating beam of light.

Within the vapor cell, the atom-light interaction is governed by the interaction

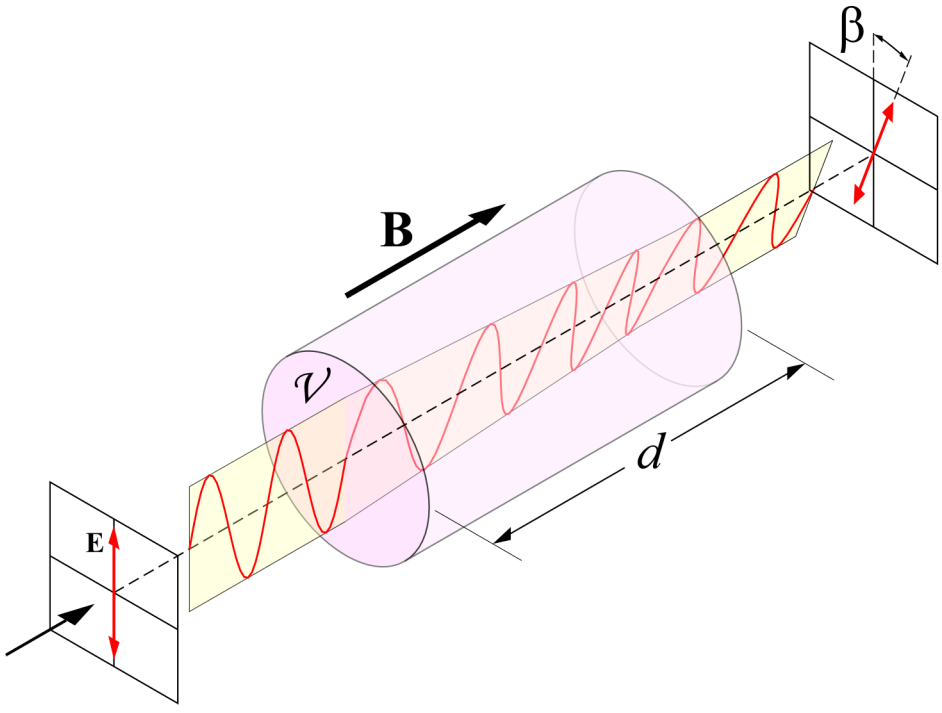

Figure 2.11: An illustration of the Faraday effect. The polarization of the incident light-field is rotated by an angle β as it passes through the medium that is within magnetic field **B**. Image credit to user Wikimedia Commons user DrBob. Shown here unedited under a CC BY-SA 3.0 license.

Hamiltonian [70]

$$\begin{aligned}\hat{H}_F &= -\frac{1}{2}\alpha_{\mathrm{v}}\frac{\mathbf{F}}{F}\cdot\frac{\mathbf{E}\times\mathbf{E}^*}{i} \\ &= -\frac{1}{2}\alpha_{\mathrm{v}}\frac{\mathbf{F}}{F}\cdot E^2\mathbf{s},\end{aligned} \tag{2.45}$$

where $\mathbf{s} = \mathbf{E}\times\mathbf{E}^*/(iE^2)$ is the photon-polarization vector first introduced earlier, * denotes complex conjugation, and α_{v} is the vector atomic polarizability of the alkali species. This effect causes the polarization axis of linearly-polarized light propagating along the μ axis to rotate by an angle [70]

$$\beta = \frac{4\pi^2 dn}{\lambda_{D_1}}\,\mathrm{Re}(\alpha_{\mathrm{v}})\frac{\langle F_\mu\rangle}{F}, \tag{2.46}$$

where d is the distance traveled through the medium, λ_{D_1} is the wavelength of the light at D_1 resonance, and $n = N/V$ is the number density of the alkali species. For

our vapor cell, $d = 1\,\mathrm{cm}$. Because we wish to measure the transverse spin, we will select $\mu = x$. For a a probe beam tuned near the D_1 optical resonance such as the one used in this work, the vector polarizability is given by [70]

$$\alpha_V(\nu) = \frac{f_{\mathrm{Res}} r_e c^2}{2\nu_{D_1}}(-i\pi)\mathcal{L}(\Delta\nu, \Gamma_{\mathrm{Tot}}), \tag{2.47}$$

where ν is the optical frequency, ν_{D_1} is the resonance frequency of the D_1 transition, $r_e = 2.818$ fm is the classical electron radius, $f_{\mathrm{Res}} \approx 1/2$ is the oscillator strength of the D_1 transition, Γ_{Tot} is the optical linewidth, $\Delta\nu = \nu - \nu_{D_1}$ is the detuning from optical resonance, and $\mathcal{L}$ is the complex Lorentzian defined by Equation 2.5. Thus we have

$$\mathrm{Re}(\alpha_V) = \frac{f_{\mathrm{Res}} r_e c^2}{2\nu_{D_1}} \frac{\Delta\nu}{\Delta\nu^2 + (\Gamma_{\mathrm{Tot}}/2)^2} = \frac{\lambda_{D_1} f_{\mathrm{Res}} r_e c}{2} \mathrm{Im}\big(\mathcal{L}(\Delta\nu, \Gamma_{\mathrm{Tot}})\big). \tag{2.48}$$

Combining the RF response of the atoms from eqation 2.22 and 2.46, we see the rotation angle for the probe beam becomes

$$\begin{aligned} \beta &= \frac{\pi n f_{\mathrm{Res}} r_e \gamma}{8} \mathrm{Im}\big(\mathcal{L}(\Delta\nu, \Gamma_{\mathrm{Tot}})\big)\mathrm{Re}\big(\mathcal{L}(\omega_{\mathrm{RF}}, \Gamma_{\mathrm{RF}})\big) dB_{\mathrm{RF}} \sin(\omega_{\mathrm{RF}} t) \\ &= \mathcal{V} dB_{\mathrm{RF}} \sin(\omega_{\mathrm{RF}} t), \end{aligned} \tag{2.49}$$

where $\mathcal{V} = (\pi n f_{\mathrm{Res}} r_e \gamma/8)\mathrm{Im}\big(\mathcal{L}(\Delta\nu, \Gamma_{\mathrm{Tot}})\big)\mathrm{Re}\big(\mathcal{L}(\omega_{\mathrm{RF}}, \Gamma_{\mathrm{RF}})\big)$ is the Verdet constant. In atomic vapors, the Verdet constant is dependent on the alkali density, along with the optical and RF frequency and the specific broadening mechanisms within the vapor cell. Comparison of Equations 2.46 and 2.49 makes it clear that the light undergoes oscillating Faraday rotation due its interaction with the spin-polarization induced in the atoms by RF driving field. We could in principle measure along any axis lying within the transverse plane of the magnetometer, as the measurement will only differ by a phase shift in the sinusoidal term. We designate the x-axis as the measurement axis for our experiments.

We now have a way to measure the RF field seen by the atoms by measuring the rotation of the polarization of the light of the probe beam: hence the name "probe". Measuring the polarization angle is quite simple using a *balanced polarimeter*. This

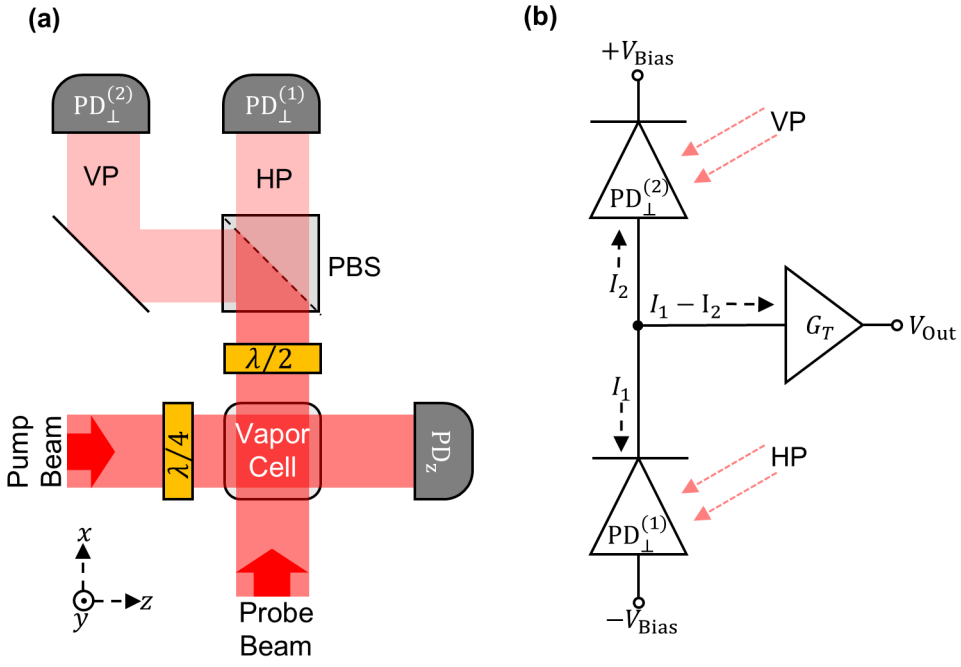

Figure 2.12: Balanced polarimetry for measurement of spin-rotation. **(a)** Optical layout for balanced detection. A probe beam along the x-axis undergoes Faraday rotation of its linear polarization due to the spin-polarization of the atoms as it traverses the vapor cell. A half-wave ($\lambda/2$) wave plate sets the angle of the polarization to be $\pi/4$ in the absence of the vapor cell. A polarizing beam-splitter (PBS) cube projects the polarization state into horizontal (HP) and vertical (VP) states. The former is parallel to the z-axis, while the latter is parallel to the y-axis. Two nominally identical photo-diodes $\mathrm{PD}_{\perp}^{(1,2)}$ detect the fluctuations of the light intensity in each polarization state as they ares modulated at the RF frequency. An additional monitor photo-diode for the pump light PD_z is shown, but not utilized for RF sensing. **(b)** Circuit diagram for balanced photo-detection. Transverse photo-diodes are biased by voltage V_{Bias}, and opposite ends connected to get a junction output that gives the current difference. Said current difference is then amplified by a trans-impedance amplifier to produce a voltage output $V_{\mathrm{Out}} = G_T(I_1 - I_2) \propto \beta$

can be constructed using a half-wave plate, polarizing beam-splitter (PBS), and two photo-detectors as illustrated in Figure 2.12. Either before or after passing through the vapor cell, a half-wave plate is used to rotate the polarization vector of the initially linearly polarized light to an angle of $\pi/4$ relative to the z-axis. Then, after passing through the medium and undergoing Faraday rotation, the PBS separates

the beam into two paths with orthogonal linear polarization states, each of which is separately incident on one of the photo-detectors. If the vapor cell were not present, or if it is not heated, so the alkali density n remains very small, the polarization of the beam as it is incident on the PBS will be $+\pi/4$ due to the wave-plate. Then the beams will have equal intensity, and the photo-detectors will produce signals of equal amplitude. *Balanced* detection from subtraction these signals then gives zero in this ideal case. However, as the Faraday effect rotates the polarization state of the light incident on the PBS, more light will be projected into one of the linear polarization states than the other, and the signal will become nonzero. In fact, so long as the rotation remains small ($\beta \ll 1$), which will be true given the small degree of transverse spin-polarization induced by the RF field, then the angle is given by

$$\beta = \frac{N_1 - N_2}{2(N_1 + N_2)}, \tag{2.50}$$

where $N_{1(2)}$ is the number of photons incident on the first(second) photo-detector respectively. What we actually measure is the current difference between the output of two photo-diodes. The current produced by the i'th photo-diode will be $I_i = q_e \eta_i N_i/\tau$ where q_e is the elementary charge of the individual carriers released at a rate $\eta_i N_i/\tau$ by N_i incident photons per measurement time τ, and η_i is the *quantum efficiency* of the diode that characterizes the faction of incident photons that free a charge carrier. It depends on the complex details of the light-matter interaction between the semiconductor material of the diode and the incident light-field. For two identically manufactured photo-diodes, $\eta_1 \approx \eta_2 = \eta$, and thus from equation 2.50, we see that $\beta = (I_1 - I_2)/[2(I_1 + I_2)]$ as the factors of q_e,η, and τ all cancel. Thus $\beta \propto I_1 - I_2$, which we can easily measure by connecting the current outputs of the photo-diodes in series with opposite polarities which gives the current difference as seen Figure 2.12(b). This can then be converted into a measurable voltage using a trans-impedance amplifier with gain G_T, giving a final output voltage

$$V_{\text{Out}} = G_T(I_1 - I_2) \propto \beta \propto B_{\text{RF}} \sin(\omega_{\text{RF}} t). \tag{2.51}$$

The proportionality of the rotation angle to the RF field amplitude will be set by

the quantum efficiency of our photo-diodes and the intensity and detuning from optical resonance of the probe beam, as discussed in the next section, along with the Verdet constant and depth of the vapor cell as discussed above. The trans-impedance gain G_T is set by the feedback network of the operational-amplifier circuit used to implement it. Equation 2.51 is the basis for deriving the laboratory signals that we will use.

2.2.6 Sensitivity and Fundamental Noise

In Section 2.2.5, the sensitivity of the total atomic spin **F** to an RF field was introduced in Equation 2.22, which provides the basis for the sensitivity of the atomic vapor to external RF fields. We then explored how this could be detected with balanced polarimetry. On RF resonance, we saw that

$$P_x = \frac{F_x}{F} = \frac{\gamma B_{\mathrm{RF}}}{2\pi\Gamma_{\mathrm{RF}}} \sin\left(\omega_{\mathrm{RF}} t\right), \tag{2.52}$$

which shows us that magnetometer signal scales inversely with the RF linewidth. As discussed in Section 2.2.4, RF linewidth is set by the combined effect of numerous relaxation mechanisms; including spin-destruction collisions, collisions with the cell walls, de-pumping effects from the pump and probe light-fields, and spin-exchange collisions. Of these, spin-exchange collisions, despite not destroying the spin coherence of the combined system, can be a dominant effect. Luckily, it can be ameliorated via *light-narrowing*. Light narrowing in this context was first predicted and subsequently demonstrated by by Appelt. et al (1998,1999) [10, 11]. It relies on the fact that when optical pumping pushes the system into the stretched state, then during a spin-exchange collision, the atoms have nearly full spin-polarization, and conservation of angular momentum dictates that since nearly all the spins already lie along the same axis, they will remain the in the same state after colliding. In principle, if the state of the ensemble was *exactly* in the stretched state, then the effect of spin-exchange collisions on the linewidth would disappear entirely. But

of course the RF field induces coherence between Zeenan levels. In particular, the stretched state couples to the $|F = F_a, m_F = F_a - 1\rangle$ state. Therefore, the atomic state of the ensemble has some projection along the $|F = F_a, m_F = F_a - 1\rangle$ state, which undergoes spin-exchange collisions that switch transverse spins during collisions, and thus degrades the transverse spin coherence. In practice, the decoherence effect of spin-exchange collisions can be ameliorated up to a point by increasing the optical pumping rate R_{OP}, which will keep the spins nearly in the stretched state and counter the mixing effect of spin-exchange collisions. However, eventually increasing the optical pumping rate further will itself lead to broadening, as the power broadening causes an increase in the RF line width. At a carefully selected value, the right balance will be struck to minimize the RF linewidth and thus optimize the sensitivity.

The basics of the aforementioned original treatment by Appelt et al. will be summarized here. We first consider the signal from the $|F, m_F\rangle \leftrightarrow |F, m_F - 1\rangle$ transition. As discussed earlier, to first order all these Zeeman transitions will be resonant at the RF (Larmor) frequency set by the bias field in the regime of linear energy splitting in which we work. The strength of the signal is then proportional to the population difference between the two coupled Zeeman levels. To calculate this difference, let $\bar{m} = [m_F + (m_F - 1)]/2 = m_F - 1/2$ be the *average* longitudinal spin-projection of the two coupled Zeeman levels between which the spin transitions. Then the population difference between Zeeman levels is proportional to [10]

$$Q_{\bar{m}} = \frac{2P(1+P)^{I+\bar{m}}(1-P)^{I-\bar{m}}}{(1+P)^{2I+1} - (1-P)^{2I+1}}. \tag{2.53}$$

Note that for $P = 1$, $Q_{\bar{m}} = 0$ for all $\bar{m}$, since all the population is in the stretched state, and there is no population difference between any of the states. However, if $P \approx 1$, then there is a small but finite population difference for $\bar{m} = F_a - 1/2 = I$, while all the other population differences vanish. Exactly the regime in which we intend to work. Appelt et al. used the formalism of the relaxation operator to obtain the linewidths of the individual Zeeman transitions. They are given by [10, 11]

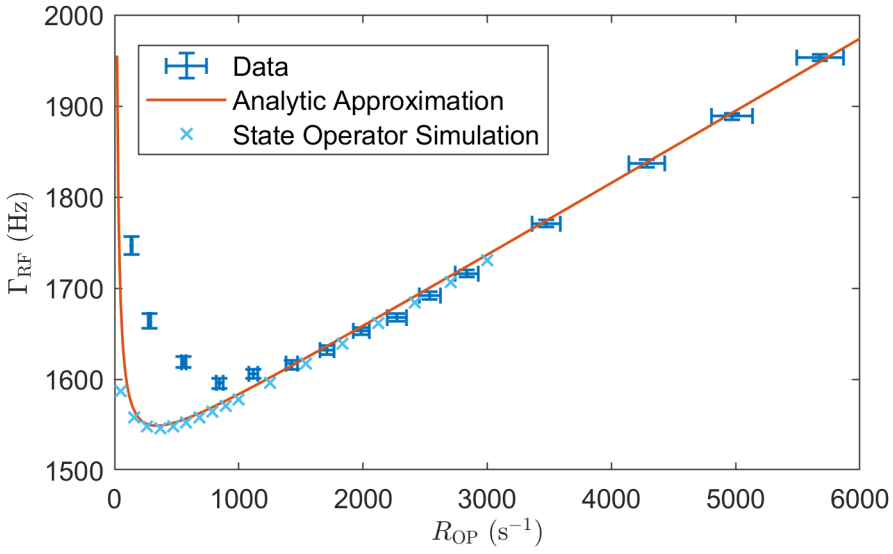

Figure 2.13: Actual data from a ^{87}Rb vapor cell, along with data from a density-operator simulation, and an analytic approximation showing the light narrowing effect. As the optical pumping rate increases, the RF linewidth sharply decreases to a minimum as the pumping compensates spin-exchange collisions and keeps the state approximately in the stretched state. Eventually the linewidth broadens again due to power broadening. A large background offset of +1.5 kHz was found in these data. Error bars in the data reflect 95% confidence for the fits used to determine the linewidth and calibrate the optical pumping rate in terms of applied laser power respectively.

$$\Gamma_{F,\bar{m}} = \frac{1}{\pi}\left[R'\frac{3(2I+1)^2+1-4\bar{m}^2}{4(2I+1)^2} - (PR_{SE}+R_{OP}s_z)\frac{\bar{m}}{2I+1}(-1)^{F_a-F}+ \right. \\ \left. - \frac{(2F+1)^2-4\bar{m}^2}{4(2I+1)^2}R_{SE}Q_{\bar{m}}f_{Iso}\right], \tag{2.54}$$

where $R' = R_{SE} + R_{SD} + R_{OP}$, and f_{Iso} is the isotopic fraction of the alkali species in question. Savukov et al. (2005) considered the case in a highly polarized isotopically pure cell where $P \approx 1$, $R_{SE} \gg R_{SD}$, and $s_z = 1$ for ^{87}Rb with $I = 3/2$. They found that the width of the end resonance with $\Gamma_{F_a,I} = \Gamma_{RF}$ could be expanded in powers of the spin-destruction rate to give the following result to first order [75]

$$\Gamma_{RF} = \frac{1}{\pi}\left(\frac{R_{OP}}{4} + \frac{R_{SE}R_{SD}}{R_{OP}}G(\omega_0, R_{SE})\right), \tag{2.55}$$

with $G(\omega_0, R_{\rm SE}) = {\rm Re}\big((R_{\rm SE} + 8i\omega_0^2/\Delta\omega_{\rm HF})/(5R_{\rm SE} + 16i\omega^2/\Delta\omega_{\rm HF})\big)$ where $\Delta\omega_{\rm HF}$ is the ground-state hyperfine splitting. Seltzer presented a generalized version of this result in his thesis [77]

$$\Gamma_{\rm RF} = \frac{1}{\pi}\Big(\frac{R_{\rm OP}}{2I+1} + \frac{R_{\rm SE}R_{\rm SD}}{R_{\rm OP}}G(\omega_0, R_{\rm SE})\Big), \tag{2.56}$$

with values of $G(\omega_0, R_{\rm SE})$ given in Table 2.1. This is the result used to provide an analytic approximation in Figure 2.13.

I	$G(\omega_0, R_{\rm SE})$
3/2	${\rm Re}\left(\dfrac{R_{\rm SE} + 8i\omega_0^2/\Delta\omega_{\rm HF}}{5R_{\rm SE} + 16i\omega_0^2/\Delta\omega_{\rm HF}}\right)$
5/2	${\rm Re}\left(\dfrac{3R_{\rm SE} + 22i\omega_0^2/\Delta\omega_{\rm HF}}{10R_{\rm SE} + 44i\omega_0^2/\Delta\omega_{\rm HF}}\right)$
7/2	${\rm Re}\left(\dfrac{5R_{\rm SE} + 36i\omega_0^2/\Delta\omega_{\rm HF}}{14R_{\rm SE} + 72i\omega_0^2/\Delta\omega_{\rm HF}}\right)$

Table 2.1: Values of $G(\omega_0, R_{\rm SE})$ for use in the approximation of the RF linewidth in Equation 2.56 provided for various nuclear spin values I by Seltzer in his thesis [77].

It is clear from Equation 2.56 that the approximation diverges in the limit of vanishing optical pumping. However, as can be see in Figure 2.13, it becomes an excellent approximation in the limit of high optical pumping rates, where the leading term becomes dominant and the second term vanishes. The calibration for the optical pumping rate in Figure 2.13 was extracted by fitting to the function

$$\Gamma_{\rm RF} \approx \frac{a}{\pi}\frac{R_{\rm OP}}{4} + b \tag{2.57}$$

in the regime of high optical pumping power. Here a is the calibration for the optical pumping rate in terms of measured photo-diode voltage, and $b = +1.5$ kHz is an offset due to background broadening. It is clear from comparison of the analytic approximation to the points produced by a full state-operator simulation that

the analytic simulation accurately produces the correct theoretical linewidth at the minimum value. Thus we conclude that the analytic approximation is valid for calculating the theoretical minimum linewidth at which we wish to operate. It is found by minimizing Equation 2.56, which gives

$$\Gamma_{\mathrm{RF,Min}} = \frac{1}{\pi}\sqrt{\frac{4G(\omega_0, R_{\mathrm{SE}})R_{\mathrm{SE}}R_{\mathrm{SD}}}{2I+1}}. \tag{2.58}$$

Equation 2.58 holds for an isotopically pure sample. From Equation 2.54, we see that if the isotopic fraction $f_{\mathrm{Iso}} < 1$, then the linewidths of the Zeeman transitions broaden by

$$\Delta\Gamma_{\mathrm{F},\bar{\mathrm{m}}} = \frac{1}{\pi}\frac{(2F+1)^2 - 4\bar{m}^2}{4(2I+1)^2}Q_{\bar{m}}f_{\mathrm{Iso}}R_{\mathrm{SE}}. \tag{2.59}$$

For the end state transition that we use, with $F = F_a = I + 1/2$, $\bar{m} = I$ and $P \approx 1 \implies Q_{\bar{m}} \approx 1$ this reduces Equation 2.59 to

$$\Delta\Gamma_{\mathrm{RF}} = \Delta\Gamma_{\mathrm{F_a,I}} = \frac{R_{\mathrm{SE}}(1 - f_{\mathrm{Iso}})}{\pi(2I+1)}. \tag{2.60}$$

Thus the total minimum RF linewidth becomes

$$\Gamma_{\mathrm{RF,Min}} = \frac{1}{\pi}\left(\sqrt{\frac{4G(\omega_0, R_{\mathrm{SE}})R_{\mathrm{SE}}R_{\mathrm{SD}}}{2I+1}} + \frac{R_{\mathrm{SE}}(1 - f_{\mathrm{Iso}})}{2I+1}\right) \tag{2.61}$$

We know that the signal amplitude scales inversely with the linewidth. Now we must find where the fundamental noise limit lies. The sensitivity of an OPM must ultimately be limited by quantum noise processes. As quantum sensors, they provide the distinct benefit of actually being able to approach this ultimate quantum mechanical limit. Savukov et al. (2005) derived the fundamental noise limit of an RF OPM [75], while Seltzer provided an expanded version of this treatment in his thesis [77], both of which we will follow here. They consider the three major contributing sources of quantum-mechanical noise:

1. **Spin-Projection Noise**: As angular momentum operators, the orthogonal

components of the total spin operator $\hat{\mathbf{F}}$ do not commute, but are given by[¶]

$$[\hat{F}_i, \hat{F}_j] = i\epsilon_{i,j,k}\hat{F}_k, \tag{2.62}$$

where $i, j, k \in \{x, y, z\}$. Thus there is an uncertainty relation given by the generalized uncertainty principle

$$\delta F_i \delta F_j \geq \tfrac{1}{2}|F_k|. \tag{2.63}$$

This is minimized for full polarization, which we have already assumed to be approximately true. Ensembles are not spin-squeezed in this work, so the directions are uncorrelated, and in particular, $\delta F_x = \delta F_y$. Then the uncertainty from N uncorrelated measurements of the transverse spin is

$$\delta F_x = \sqrt{\frac{|F_z|}{2N}}. \tag{2.64}$$

We do not perform discrete measurements. Instead, we continuously probe the ensemble with the probe beam and monitor the signal. Gardner (1986) provides the uncertainty for the case of continuous measurements such as ours [38]

$$\begin{aligned} \delta\langle F_x\rangle &= \delta F_x \left[\frac{2}{t}\int_0^t \Big(1 - \frac{\tau}{t}\mathcal{K}(\tau)\Big)d\tau\right]^{1/2} \\ &= \delta F_x \left[\frac{2}{\pi\Gamma_{\mathrm{RF}}t} + \frac{2\big(\mathcal{K}(t)-1\big)}{\pi^2\Gamma_{\mathrm{RF}}^2 t^2}\right]^{1/2}, \end{aligned} \tag{2.65}$$

where $\mathcal{K}(\tau) = e^{-\pi\Gamma_{\mathrm{RF}}\tau}$ is the time correlation function for spin-coherence. For measurement times $t \gg T_2 = 1/\pi\Gamma_{\mathrm{RF}}$, we can combine Equations 2.65 and 2.64 to find the transverse uncertainty within a measurement bandwidth $BW = 1/(2t)$ to be

$$\delta\langle F_x\rangle = \sqrt{\frac{2F_z BW}{\pi\Gamma_{\mathrm{RF}}N}}. \tag{2.66}$$

[¶]Einstien summation over repeated indices is implied here.

The noise power in this bandwidth is then

$$\delta \langle F_x \rangle^2 = \frac{2F_z BW}{\pi \Gamma_{\mathrm{RF}} N}. \tag{2.67}$$

So the root-mean sqaure (RMS) noise power per unit bandwidth is

$$\delta \langle F_x \rangle^2_{\mathrm{RMS}} = \frac{2F_z}{\pi \Gamma_{\mathrm{RF}} N}. \tag{2.68}$$

Thus the RMS noise amplitude per unit bandwidth is simply Equation 2.66 divided by $\sqrt{BW}$

$$\delta \langle F_x \rangle_{\mathrm{RMS}} = \sqrt{\frac{2F_z}{\pi \Gamma_{\mathrm{RF}} N}}. \tag{2.69}$$

Using Equation 2.52, we can calculate the noise in the transverse polarization-projection to be

$$\delta \langle P_x \rangle = \frac{\delta \langle F_x \rangle}{F} = \frac{\gamma}{2\pi \Gamma_{\mathrm{RF}}} \delta B_{\mathrm{RF}}. \tag{2.70}$$

Combing Equations 2.70 and 2.69 we can find the RMS spin-projection noise per unit bandwidth in the RF magnetic field to be

$$\delta B_{\mathrm{SPN}} = \frac{1}{\gamma} \sqrt{\frac{8\pi \Gamma_{\mathrm{RF}}}{F_z N}} \approx \frac{1}{\gamma} \sqrt{\frac{8\pi \Gamma_{\mathrm{RF}}}{(I+1/2)N}}. \tag{2.71}$$

2. **Photon Shot Noise**: We consider the photon-flux over the total area A_{PR} of the probe beam, which is given by integrating the photon-flux per unit-area Φ taken over the entire pump beam

$$\Phi_{\mathrm{Tot}} = \int_{A_{\mathrm{PR}}} \Phi dA. \tag{2.72}$$

The photon flux is simply the incident photons photons N_{P} per time τ, so $\Phi_{\mathrm{Tot}} = N_{\mathrm{P}}/\tau$. Thus we can combine this result with Equation 2.50 to get the measured rotation angle of the polarimeter in terms of the photon fluxes of the orthogonal polarization states in the arms of the polarimeter

$$\beta = \frac{\Phi_V - \Phi_H}{2(\Phi_V + \Phi_H)}, \tag{2.73}$$

where $\Phi_{V(H)}$ is the photon flux with vertical(horizontal) polarization in the polarimeter. The photon fluxes in each arm of the the polarimeter are nominally balanced, with $\beta \ll 1$ a small angle, so $\Phi_V \approx \Phi_H = \Phi_{\text{Tot}}/2$. Then the quantum fluctuations of the flux in each arm of the polarimeter are[‖]

$$\delta\Phi_{V(H)} \approx \sqrt{\frac{\Phi_{\text{Tot}}}{2}}. \tag{2.74}$$

The corresponding RMS fluctuation per unit bandwidth in the measurable rotation angle is then

$$\begin{aligned} \delta\left\langle\beta\right\rangle_{\text{RMS}} &= \sqrt{2\left[\left(\frac{\partial\beta}{\partial\Phi_V}\delta\Phi_V\right)^2 + \left(\frac{\partial\beta}{\partial\Phi_H}\delta\Phi_H\right)^2\right]} \\ &= \sqrt{\frac{1}{2\Phi_{\text{Tot}}}}. \end{aligned} \tag{2.75}$$

Accounting for the finite quantum efficiency η at which the photo-diodes convert incident photons into measurable current, we can then use Equations 2.52 and 2.75 to find the RMS photon shot-shot noise per unit bandwidth in the measurement of the magnetic field on RF resonance to be

$$\delta B_{\text{PSN}} = \frac{4\Gamma_{\text{RF}}}{\gamma d n r_e c f_{\text{Res}} \left|\text{Im}\big(\mathcal{L}(\Delta\nu, \Gamma_{\text{Tot}})\big)\right| \sqrt{2\eta\Phi_{\text{Tot}}}}. \tag{2.76}$$

3. **Light-Shift Noise**: The AC Stark effect of the pump and probe lasers causes a shift in the energy levels of the atoms given by Appelt et al. (1998) to be [10]

$$\begin{aligned} \Delta E_{\text{AC}} &= \tfrac{1}{2}\pi\hbar r_e c f_{\text{Res}} \Phi (1 - 2\mathbf{s}\cdot\mathbf{S}) \text{Im}\big(\mathcal{L}(\Delta\nu, \Gamma_{\text{Tot}})\big). \\ &= \tfrac{1}{2}\pi\hbar r_e f_{\text{Res}} \Phi \text{Im}\big(\mathcal{L}(\Delta\nu, \Gamma_{\text{Tot}})\big) + \hbar\gamma_e \mathbf{B}_{\text{LS}}\cdot\mathbf{S}, \end{aligned} \tag{2.77}$$

where the second line reflects the fact that the first line can be decomposed into a constant term common to all energy levels, and a vector term with the

[‖] This assumes the state of the light is given by a coherent state, and thus displays classical Poissonian statistics. Because we do not squeeze the state of the probe beam, this is true in our case.

same form as the Zeeman interaction. Because we measure energy *differences* between Zeeman levels, the common offset in the first term of the second line has no measurable effect. The measurable response of the atoms to this light-shift is indistinguishable from the influence of an additional external field given by

$$\mathbf{B}_{\mathrm{LS}} = -\frac{\pi r_e c f_{\mathrm{Res}} \Phi}{\gamma_e} \mathrm{Im}\big(\mathcal{L}(\Delta\nu, \Gamma_{\mathrm{Tot}})\big)\mathbf{s}. \tag{2.78}$$

Because this effect is indistinguishable from the influence of an external magnetic field, the influence can be compensated by applying a control field $\mathbf{B}_{\mathrm{Cont}} = -\mathbf{B}_{\mathrm{LS}}$. However, there will also be quantum fluctuations in the photon polarization state $\mathbf{s}$, which will then be converted into amplitude noise by the PBS within the balanced polarimeter and appear as noise within the measured magnetic field. We may write the linear polarization of the probe beam as an equal superposition of $\sigma_\pm$ states. To do so, let $\Phi_\pm$ be the total fluxes of circularly polarized photons with positive and negative helicities, then the polarization s of the probe beam is an equal superposition of circularly polarized photon-fluxes with opposite helicities given by

$$s = \frac{\Phi_+ - \Phi_-}{\Phi_{\mathrm{Tot}}}, \tag{2.79}$$

where $\Phi_{\mathrm{Tot}} = \Phi_+ + \Phi_-$ is the total photon flux. Since the superposition is equal, the photon number and thus quantum noise in each circular polarization mode is equal

$$\delta\Phi_\pm = \sqrt{\frac{\Phi_{\mathrm{Tot}}}{2}}. \tag{2.80}$$

Then the calculation of the total RMS noise per unit bandwidth in $\langle s \rangle$ proceeds almost identically to the one carried out for the rotation angle noise in Equation 2.75

$$\begin{aligned} \delta\langle s \rangle_{\mathrm{RMS}} &= \sqrt{2\left[\left(\frac{\partial s}{\partial \Phi_+}\delta\Phi_+\right)^2 + \left(\frac{\partial s}{\partial \Phi_-}\delta\Phi_-\right)^2\right]} \\ &= \sqrt{\frac{1}{2\Phi_{\mathrm{Tot}}}}. \end{aligned} \tag{2.81}$$

We can then combine Equations 2.78 and 2.81 to get the RMS magnetic field noise per unit bandwidth due to quantum fluctuation in the light polarization state to be

$$\delta B_{\mathrm{LSN}} = \frac{\sqrt{2}\pi r_e c f_{\mathrm{Res}} \Phi}{2(2I+1)\gamma\sqrt{\Phi_{\mathrm{Tot}}}} \left|\mathrm{Im}\big(\mathcal{L}(\Delta\nu, \Gamma_{\mathrm{Tot}})\big)\right|. \tag{2.82}$$

Note there is an extra factor of $1/2$ in the RF field noise compared to the DC field described by Equation 2.78. This is due to only the co-rotating component of the RF field making a meaningful contribution. In general, the photon flux per unit-area Φ depends on the exact spacial profile of the light-field of the probe laser. To attain an average value throughout the cell, we can approximate $\Phi \approx \Phi_{\mathrm{Tot}}/A$, where A is the effective cross-sectional area of the probe laser. Then we may approximate the RMS light-shift noise per unit bandwidth over the entire cell as

$$\delta B_{\mathrm{LSN}} \approx \frac{\sqrt{2\Phi_{\mathrm{Tot}}}\pi r_e c f_{\mathrm{Res}}}{2(2I+1)\gamma A} \left|\mathrm{Im}\big(\mathcal{L}(\Delta\nu, \Gamma_{\mathrm{Tot}})\big)\right|. \tag{2.83}$$

Figure 2.14 shows the contribution to the quantum noise floor from each of the three effects, along with the total given by their quadrature sum for realistic values measured in our magnetometer using ^{85}Rb. Note that at the lowest noise value, the spin-projection noise dominates, while for values near resonance or far detuned from it, the photon shot noise becomes the dominant effect. We also see that our magnetometer can achieve a sensitivity on the order of 1 fT $\mathrm{Hz}^{-1/2}$.

We see from Figure 2.14 that the best sensitivity is achieved several linewidths off-resonance, where we may approximate $\mathrm{Im}\big(\mathcal{L}(\Delta\nu, \Gamma_{\mathrm{Tot}})\big) \approx 1/(\pi\Delta\nu)$. In this regime, the off-resonant pumping rate of the probe beam is given by

$$R_{\mathrm{PR}} = \sigma(\Delta\nu, \Gamma_{\mathrm{Tot}})\frac{\Phi_{\mathrm{Tot}}}{A} = \frac{r_e c f_{\mathrm{Res}} \Gamma_{\mathrm{Tot}} \Phi_{\mathrm{Tot}}}{2A\Delta\nu^2}, \tag{2.84}$$

and resonant optical depth of the probe beam is given by

$$\mathrm{OD}_0 = \sigma(\Delta\nu = 0, \Gamma_{\mathrm{Tot}}) nd = \frac{2ndr_e c f_{\mathrm{Res}}}{\Gamma_{\mathrm{Tot}}}. \tag{2.85}$$

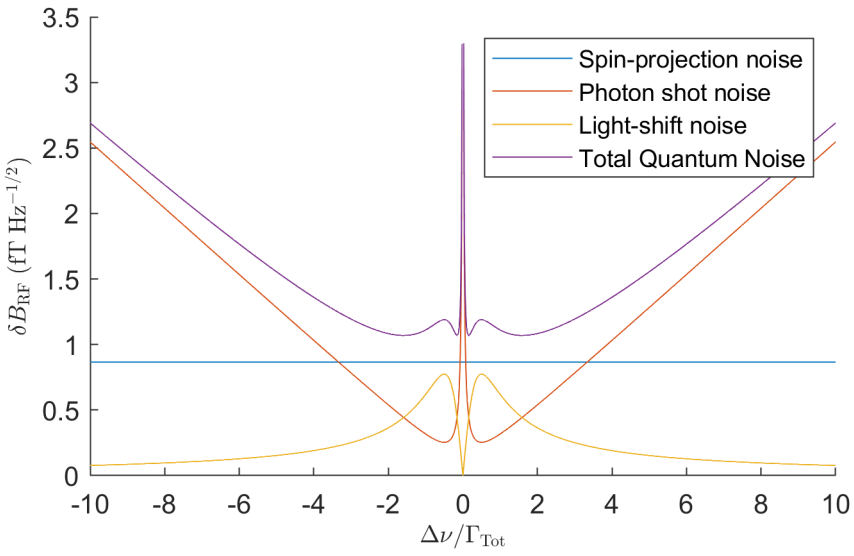

Figure 2.14: Comparison of quantum noise sources in our RF magnetometer using realistic values for ^{85}Rb. Cell temperature was assumed to be 125°C. Area was estimated using the $1/e^2$ Gaussian size of the probe beam. Photon flux was estimated from a realistic probe beam power of 20 mW as $\Phi_{\mathrm{Tot}} = 20\ \mathrm{mW}/(\hbar\nu_{D_1})$. This sensitivity assumes an approximately 1 cm^3 cubic cell with a length of $d = 1$ cm on each side. A quantum efficiency of 90% was used.

These results allow us to write the total magnetic field noise as the quadrature sum of the three effects

$$\begin{aligned}\delta B_{\mathrm{RF}} &= \sqrt{\delta B_{\mathrm{SPN}}^2 + \delta B_{\mathrm{PSN}}^2 + \delta B_{\mathrm{LSN}}^2} \\ &= \frac{1}{\gamma\sqrt{nV}}\sqrt{\frac{16\pi\Gamma_{\mathrm{RF}}}{(2I+1)} + \frac{8(\pi\Gamma_{\mathrm{RF}})^2}{R_{\mathrm{PR}}\mathrm{OD}_0\eta} + \frac{R_{\mathrm{PR}}\mathrm{OD}_0}{2(2I+1)^2}},\end{aligned} \tag{2.86}$$

where we have identified $N = nV$ with active measurement volume V defined by the intersection of the probe and pump beams. We can minimize Equation 2.86 to find that the optimum value occurs where the last two terms under the radical in the second line are equal, giving

$$R_{\mathrm{PR}}\mathrm{OD}_0 = \frac{4\pi\Gamma_{\mathrm{RF}}(2I+1)}{\sqrt{\eta}}. \tag{2.87}$$

Using the minimized value of Γ_{RF} provided by Equation 2.61, we see that the best

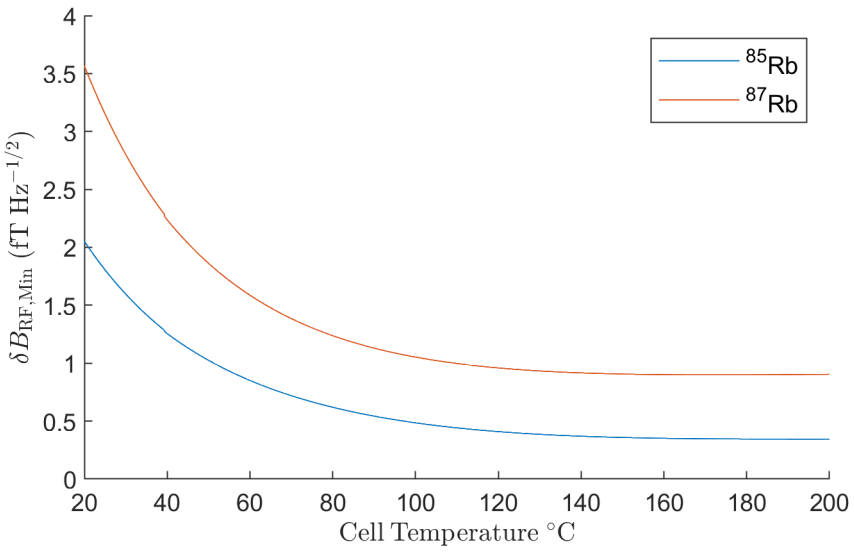

Figure 2.15: Theoretical optimal sensitivity vs. cell temperature using our natural abundance Rb vapor cell with 400 Torr of nitrogen. Density was calculated using the CRC formula for Rb vapor pressure over liquid, and is likely an over-estimate. The approximation $G(\omega_0, R_{\mathrm{SE}}) \approx 1/5, 3/10$ was used for $I = 3/2, 5/2$ because we are in the regime $\omega_{\mathrm{RF}} \ll \omega_{\mathrm{HF}}$. Quantum efficiency was generously assumed to be $\eta = 0.9$. The fundamental sensitivity limit using ^{85}Rb is around 0.4 fT Hz$^{-1/2}$. Using ^{87}Rb leads to worse sensitivity due to considerably less isotopic abundance.

possible sensitivity at maximum light-narrowing is given by

$$\delta B_{\mathrm{RF,Min}} = \frac{1}{\gamma\sqrt{nV}}\sqrt{\frac{4(4+\eta^{-1/2})}{2I+1}\left(\sqrt{\frac{4G(\omega_0, R_{\mathrm{SE}})R_{\mathrm{SE}}R_{\mathrm{SD}}}{2I+1}} + \frac{R_{\mathrm{SE}}(1-f_{\mathrm{Iso}})}{2I+1}\right)}. \tag{2.88}$$

Values in Figure 2.15 are smaller than the minimum value seen in Figure 2.14 because the theoretical smallest linewidth given by Equation 2.61 under these conditions is $\Gamma_{\mathrm{RF,Min}} \approx 552$ Hz, while the measured value is closer to $\Gamma_{\mathrm{RF}} = 1.5$ kHz. Previous measurements of alkali density in a heated vapor cell also indicate that the CRC formula tends to under-estimate the true vapor density at a given temperature, reducing the number of interacting particles and decreasing the sensitivity [77]. Nevertheless, Figure 2.15 shows why we prefer to operate in the $120 - 130$°C temperature range: It puts us into the asymptotic regime of maximum achievable sensitivity while re-

quiring the least heater power, and also without unnecessarily increasing the optical depth so much that untenable laser powers are required for pumping and probing.

2.3 Conclusions

In this chapter, we have seen see the great promise in this approach to RF magnetometery with OPMs. We have also seen the limitation of the technique: it requires the bias field $\mathbf{B}_0$ being maintained at the correct value. This has made the application of this technique challenging outside the controlled magnetic field environment provided by a magnetic shield, and limited the accessible applications. In the next Section, we explore a method that provides for active control of $\mathbf{B}_0$, allowing us to maintain the correct bias field in an unshielded environment.

Chapter 3

OPM Variometry

To implement the techniques detailed in Chapter 2 within dynamic magnetic field environments outside of a magnetic shield, we must actively stabilize the low-frequency field environment near DC so the atoms experience the correct bias field. This can be achieved via active feedback to a set of tri-axial field control coils that produce a control field $\mathbf{B}_{\text{Cont}}$ such that the low-frequency field external field is properly compensated and $\mathbf{B}_{\text{Cont}} + \mathbf{B}_{\text{Ext}} = \mathbf{B}_0$. Then the question becomes, how do we produce the correct control field?

We must measure $\mathbf{B}_{\text{Ext}}$ to obtain the requisite information to synthesize the correct control field. What we need is another magnetometer that operates near DC within Earth's geomagnetic field. This magnetometer must sample the magnetic field close to, or preferably within, the volume of the vapor cell containing the RF OPM in order to minimize errors due to gradients within the external field. One approach is to use a flux-gate magnetometer positioned as near as physically possible to minimize the distance between the flux-gate probe and the OPM vapor cell. This approach is used by several groups in the United Kingdom focused on electromagnetic induction imaging applications in medicine, industry, and security [50, 72, 16, 17, 15, 29, 31, 30, 18, 58, 32, 28, 59, 60, 46]. The best sensitivity achieved via this method thus far

is 50 fT $\text{Hz}^{-1/2}$ [58]. In this work, we opted to develop a new approach using another OPM directly within the same vapor cell. This approach provides the advantage of sampling from within *exactly* the same volume occupied by the RF OPM, and thus minimizing errors due to field gradients.

3.1 Conceptual Overview

To understand how we build this second *comagnetoemter* within the vapor cell, note that because natural rubidium contains 72.15% ^{85}Rb with $I = 5/2$ and 27.85% ^{85}Rb with $I = 3/2$. If we use the former to create a high-sensitivity RF OPM based on its larger abundance, as seen in the comparison in Figure 2.15, we can then use the latter as an a secondary OPM. This works because the gyromagnetic ratio of an atomic species with nuclear spin I is given by

$$\gamma = \frac{\gamma_e}{q} = \frac{\gamma_e}{2I+1}, \tag{3.1}$$

where γ_e is the gyromagnetic ratio of a bare electron. So the ratio of gyromagetic ratios between the two isotopes in natural Rb is

$$\frac{\gamma_{87}}{\gamma_{85}} = \frac{\frac{\gamma_e}{2(3/2)+1}}{\frac{\gamma_e}{2(5/2)+1}} = \frac{3}{2}. \tag{3.2}$$

Combing Equation 3.2 with Equation 1.1, we see that in a given external bias field B_0, if ^{85}Rb is resonant at the RF frequency so $f_{85} = f_{\text{RF}} = \gamma_{85} B_0/(2\pi)$, then ^{87}Rb is resonant at

$$f_{87} = \frac{3}{2} f_{\text{RF}}. \tag{3.3}$$

Figure 3.1(a) shows how the amplitude of the RF atomic response from the two isotopes splits in frequency for the two isotopes within natural Rb. It is important to note that Equation 3.3 holds only to first order in the regime of linear Zeeman splitting. In addition, slight differences in the AC Stark shift between the two isotopes can contribute to differential resonant frequency shifts that affect this result.

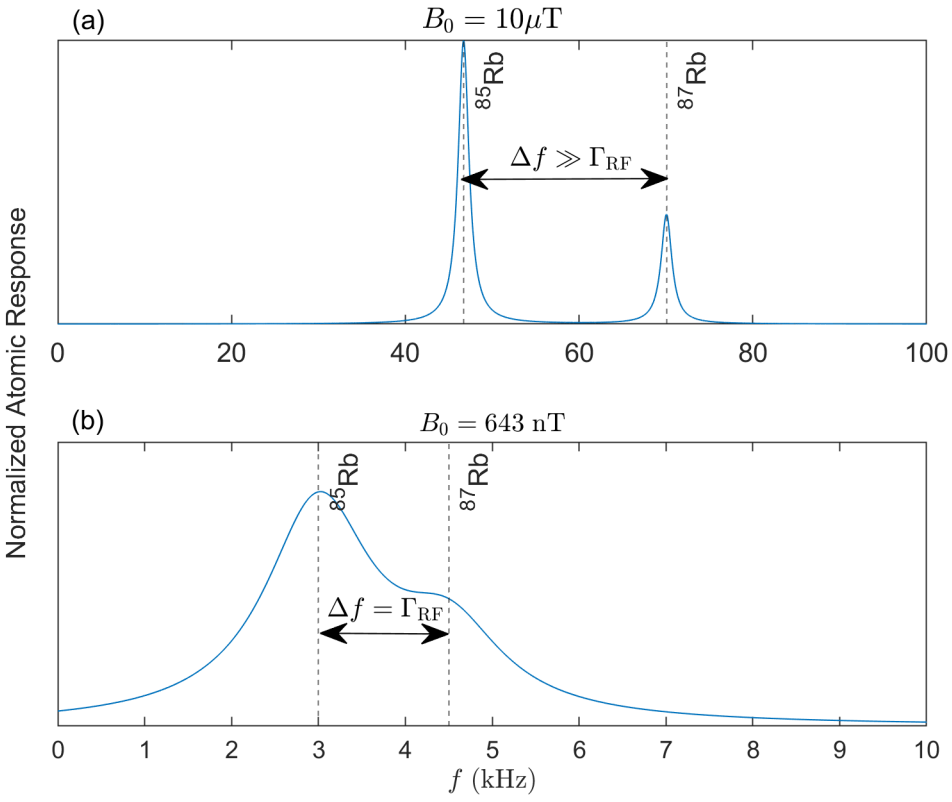

Figure 3.1: Amplitude of the RF atomic response vs. frequency as given by Equation 2.5 with FWHM linewidth of $\Gamma_{RF} = 1.5$ kHz. Relative weights of each response are provided by the abundances of 72.15% and 27.85% for ^{85}Rb and ^{87}Rb respectively. **(a)** The frequency separation is large in comparison to the RF linewidth. The clear separation between the responses allows us to operate the variometer and RF magnetometer simultaneously. **(b)** The same situation as in (a), but at the minimum resolvable frequency of $f_{RF,Min} = 2\Gamma_{RF} = 3$ kHz, showing how the responses can only just be individually resolved.

However, these offsets will be much smaller than the ~ 1 kHz RF linewidth and can be neglected for our purposes. Thus by holding ^{87}Rb resonant at 3/2 the desired RF sensing frequency, we can properly stabilize the external field near DC for RF sensing with ^{85}Rb. In addition to providing field information from directly within the same volume as the RF OPM vapor cell, this also allows for a more compact device and for reduction in power consumption. Details of the integration of this secondary OPM will be discussed in Chapter 4. Here, we will discuss how an OPM *variometer*

can provide the platform we need for magnetic field sensing near DC. This approach will work so long as the responses of the two isotopes remain clearly distinguishable in frequency. The lowest frequency at which this approach can operate at a given FWHM RF linewidth Γ_{RF} is

$$\Delta f = f_{87} - f_{85} \geq \Gamma_{\mathrm{RF}}. \tag{3.4}$$

The condition for resolvability in Equation 3.4 can be simplified using the ratio from Equation 3.3 to get the minimum operating frequency and bias field in terms of the RF linewidth and gyromagnetic ratio of ^{85}Rb

$$f_{\mathrm{RF}} \geq 2\Gamma_{\mathrm{RF}} \tag{3.5a}$$

$$B_0 \geq \frac{2\pi}{\gamma_{85}} 2\Gamma_{\mathrm{RF}}. \tag{3.5b}$$

Figure 3.1(b) shows the situation at the minimum resolvable frequency of $f_{\mathrm{RF}} = 3$ kHz in a bias field of $B_0 = 642$ nT with an RF linewidth of $\Gamma_{\mathrm{RF}} = 3$ kHz.

Now we will turn out attention to exactly how to build the secondary OPM for active field stabilization. Our method is based on using a modified OPM *variometer*. This discussion will closely follow the methodology for the OPM variometetry presented by E.B. Alexandrov and colleagues at the Vavilov State Optical Institute in St. Petersburg, RU [4, 3, 90]. It starts with a standard scalar magnetometer that works by orienting the longitudinal axis approximately along the external field, which we will assume is provided by Earth's geomagnetic field, so $\mathbf{B}_{\mathrm{Ext}} = \mathbf{B}_{\mathrm{Earth}}$. The total external field may also be affected by additional fields from sources such as power lines, industrial equipment, metal used in structures, etc. But that will not affect the conclusions of this discussion, as they can be simply included as part of $\mathbf{B}_{\mathrm{Ext}}$. Measuring the Larmor frequency by monitoring the transverse spin-polarization allows the magnitude of the external field to be easily determined as shown in Figure 1.1 and Equation 1.1. If we wish to stabilize the field near DC, we can use the information provided by this simple scalar magnetometer to provide feedback currents

to drive control coils with a control current $I_{\mathrm{Cont},z}$ to provide a longitudinal control field $B_{\mathrm{Cont},z}$ such that

$$2\pi f_{\mathrm{RF}} = \gamma|\mathbf{B}_{\mathrm{Ext}} + B_{\mathrm{Cont},z}\mathbf{e}_z| = \gamma|\mathbf{B}_{\mathrm{Tot}}|. \tag{3.6}$$

Equation 3.6 assumes that $\mathbf{B}_{\mathrm{Ext}} \approx B_{\mathrm{Ext},z}\mathbf{e}_z$, since the device has been oriented to approximately align the longitudinal axis along the geomagnetic field. Thus we have a method to stabilize the longitudinal field. It can also be used to measure the fluctuations $|\Delta\mathbf{B}_{\mathrm{Ext}}(t)|$ in the amplitude of the geomagnetic field over time, since $\Delta B_{\mathrm{Ext}}(t) \propto B_{\mathrm{Cont},z}(t) \propto I_{\mathrm{Cont},z}(t)$. Thus known calibrations $I_{\mathrm{Cont},z}(t)$ provide a record of the amplitude variation in the geomagnetic field over time. Tracking these variations was the original intent of the OPM variometery and is the reason for its name.

As alluded to in the previous paragraph, external geomagnetic fields are not perfectly static. They vary over time, and these variations are not confined to a single direction. For this reason, the longitudinal direction of the variometer can only ever be approximately aligned along the direction of the geomagnetic field vector, even in the ideal case. We thus need a method to track variations in the plane transverse to the optical pumping beam. To achieve this, we can use additional magnetic field coils oriented to drive magnetic fields along the x and y directions, which we shall denote the x and y *modulation* coils. These coils are used to drive a small a rotating magnetic field $\mathbf{B}_{\mathrm{Mod},\perp}$ in the transverse plane of the magnetometer that rotates at transverse modulation frequency $\omega_\perp \ll \omega_{\mathrm{RF}}$, such that the modulation field is approximately static relative to the RF oscillation. We must also avoid introducing significant perturbation to the total field amplitude, so we require $B_{\mathrm{Mod},\perp} \ll B_0$, such that the total field is minimally affected by this small modulation. Then the transverse modulation field is given by

$$\begin{aligned}\mathbf{B}_{\mathrm{Mod},\perp}(t) &= B^{(x)}_{\mathrm{Mod},\perp}(t)\mathbf{e}_x + B^{(y)}_{\mathrm{Mod},\perp}(t)\mathbf{e}_y \\ &= B_{\mathrm{Mod},\perp}\big(\cos(\omega_\perp t)\mathbf{e}_x + \sin(\omega_\perp t)\mathbf{e}_y\big).\end{aligned} \tag{3.7}$$

Equation 3.7 reflects how we achieve a rotating modulation: we drive the x and y modulation coils with sinusoidal currents that have a $\pi/2 = 90°$ phase offset. We take the phase of driving-field along the x-axis to be zero, and thus drive it with an in-phase (I) sinusoid given by the cosine term, while the y-axis is driven with an in-quadrature (Q) sinusoid with a $+\pi/2$ (90°) phase-shift given by the sine term. The rotating modulation is illustrated in Figure 3.2(a). Figure 3.2 (a) and (b) show the dynamics of the variometer when the external field is exactly along the longitudinal direction. In this case, the transverse field is given by $\mathbf{B}_\perp = \mathbf{B}_{\mathrm{Mod},\perp}$. Because $B_{\mathrm{Mod},\perp} \ll B_0$, the overall field amplitude as a function of time is given by

$$\begin{aligned}
|\mathrm{B_{Tot}(t)}| &= \sqrt{B_0^2 + B_\perp(t)^2} \\
&= \sqrt{B_0^2 + \Big[\big(B_{\mathrm{Mod},\perp}\cos(\omega_\perp t)\big)^2 + \big(B_{\mathrm{Mod}}\sin(\omega_\perp t)\big)^2\Big]} \\
&= \sqrt{B_0^2 + B_{\mathrm{Mod},\perp}^2\Big[\cos(\omega_\perp t)^2 + \sin(\omega_\perp t)^2\Big]} \\
&= \sqrt{B_0^2 + B_{\mathrm{Mod},\perp}^2} \\
&\approx B_0.
\end{aligned} \tag{3.8}$$

Equation 3.8 shows that if the external field is oriented completely along the longitudinal direction, the total field amplitude remains constant in time, and is well approximated by the longitudinal field, as shown in Figure 3.2 (b). Now let us consider what happens when a small transverse component $\Delta\mathbf{B}_\perp$ is present in the external field, so the external field is $\mathbf{B}_{\mathrm{Ext}} = \big(B_0 + \Delta B_z\big)\mathbf{e}_z + \Delta B_\perp \mathbf{e}_\perp$ where $\mathbf{e}_\perp$ is a general unit vector in the transverse plane. We will assume any dynamics in the behavior of $\Delta B(t)$ occur on a time-scale $\tau_\Delta \gg 1/\omega_\perp$, so we may treat this transverse error field as a constant relative to the rotating modulation field. If we let $\mathbf{e}_\perp = \mathrm{I}\mathbf{e}_x + \mathrm{Q}\mathbf{e}_y$ where $\mathrm{I}^2 + \mathrm{Q}^2 = 1$, then the transverse field becomes

$$\begin{aligned}
\mathbf{B}_\perp(t) &= B_{\mathrm{Mod},\perp}\big(\sin(\omega_\perp t)\mathbf{e}_x + \cos(\omega_\perp t)\mathbf{e}_y\big) + \Delta B_\perp \mathbf{e}_\perp \\
&= \big(B_{\mathrm{Mod},\perp}\cos(\omega_\perp t) + \Delta B_\perp \mathrm{I}\big)\mathbf{e}_x + \big(B_{\mathrm{Mod},\perp}\sin(\omega_\perp t) + \Delta B_\perp \mathrm{Q}\big)\mathbf{e}_y.
\end{aligned} \tag{3.9}$$

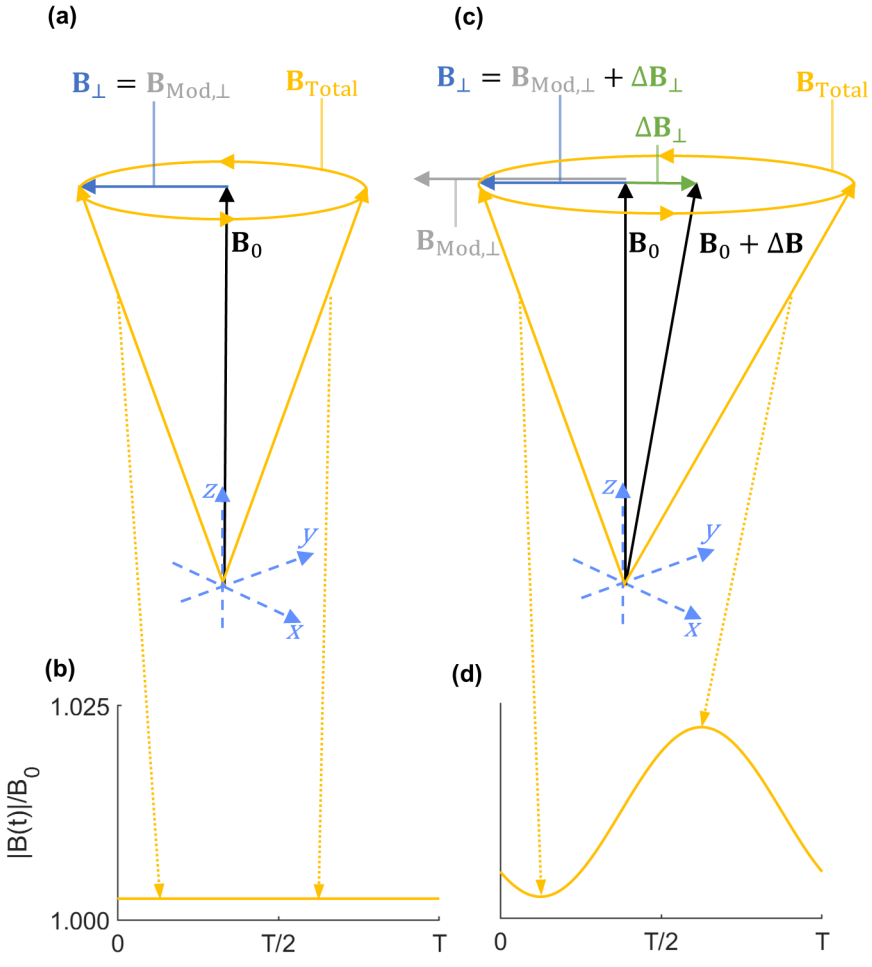

Figure 3.2: Dynamics of the rotating variometer modulation in the transverse plane. **(a)** Rotating modulation adds a small rotation about the longitudinal magnetic field in the transverse plane. In the absence of external transverse fields, the total field amplitude $B_{\mathrm{Tot}} = \sqrt{B_0^2 + B_{\mathrm{Mod}}^2} \approx B_0$ remains constant over time, as illustrated by the plot in **(b)** of the field amplitude vs. time. Arrows indicate sample points on the rotation in (a) and the corresponding field amplitude in (b). In **(c)**, an external offset in the transverse field introduces an alternating addition and subtraction to the rotating modulation field, leading to a modulation of the field amplitude at frequency $f_\perp = \omega_\perp/(2\pi)$, as illustrated in **(d)**. Arrows again connect points in the rotation of the modulation field in (c) to the corresponding field amplitude in (d). Values in (d) were calculated using an offset field of $\Delta\mathbf{B}_\perp = \frac{B_0}{10}\frac{1}{\sqrt{2}}(\mathbf{e}_x + \mathbf{e}_y)$.

So the amplitude of the transverse field is

$$\begin{aligned} B_\perp(t) &= \sqrt{B_x(t)^2 + B_y(t)^2} \\ &= \sqrt{\left(B_{\mathrm{Mod},\perp}\cos(\omega_\perp t) + \Delta B_\perp \mathrm{I}\right)^2 + \left(B_{\mathrm{Mod},\perp}\sin(\omega_\perp t) + \Delta B_\perp \mathrm{Q}\right)^2} \\ &= \sqrt{\left(B_{\mathrm{Mod},\perp}^2 + \Delta B_\perp^2\right) + 2B_{\mathrm{Mod},\perp}\Delta B_\perp\left(\mathrm{I}\cos(\omega_\perp t) + \mathrm{Q}\sin(\omega_\perp t)\right)}. \end{aligned} \tag{3.10}$$

Thus the total field amplitude as a function of time is

$$\begin{aligned} |\mathbf{B}_{\mathrm{Tot}}(t)| &= \sqrt{(B_0 + \Delta B_z)^2 + B_\perp(t)^2} \\ &= \Big[\left((B_0 + \Delta B_z)^2 + B_{\mathrm{Mod},\perp}^2 + \Delta B_\perp^2\right) \\ &\qquad + 2B_{\mathrm{Mod},\perp}\Delta B_\perp\left(\mathrm{I}\cos(\omega_\perp t) + \mathrm{Q}\sin(\omega_\perp t)\right)\Big]^{1/2}. \end{aligned} \tag{3.11}$$

Equation 3.11 shows that in the presence of an external transverse offset field, the total field amplitude is modulated at $\omega_\perp$. Furthermore, this modulation can be broken into two orthogonal components with a $\pi/2$ (90°) phase shift between them. The in-phase (I) part of this modulation corresponds to the x-component of the offset field, while the in-quadrature (Q) part corresponds to the y-component. Thus by using phase-sensitive lock-in detection of this modulation of the field amplitude, we can fully characterize the transverse components of the external field to obtain control currents $I_{\mathrm{Cont},x(y)} \propto \Delta B_{x(y)}$ which can be applied via additional field *control* coils oriented along the $x(y)$-axes to produce transverse control fields $\mathbf{B}_{\mathrm{Cont},x(y)}$ that cancel the effect of deviations in the transverse field.

Once the transverse part $\Delta\mathbf{B}_\perp$ of the external offset field is known along with the total field amplitude $|\mathbf{B}|$, we have full information on the external field from which we can synthsize feedback to compensate it. Figure 3.3 gives a block diagram overview of our implementation of the variometer to stabilize the field environment near DC and maintain the correct bias field along the longitudinal axis. The approach outlined here could be implemented by digital or analog means. Alexandrov et al. originally used a fully analog approach. We opted to use a mixed analog and digital platform using a field-programmable gate array (FPGA) to implement various tasks,

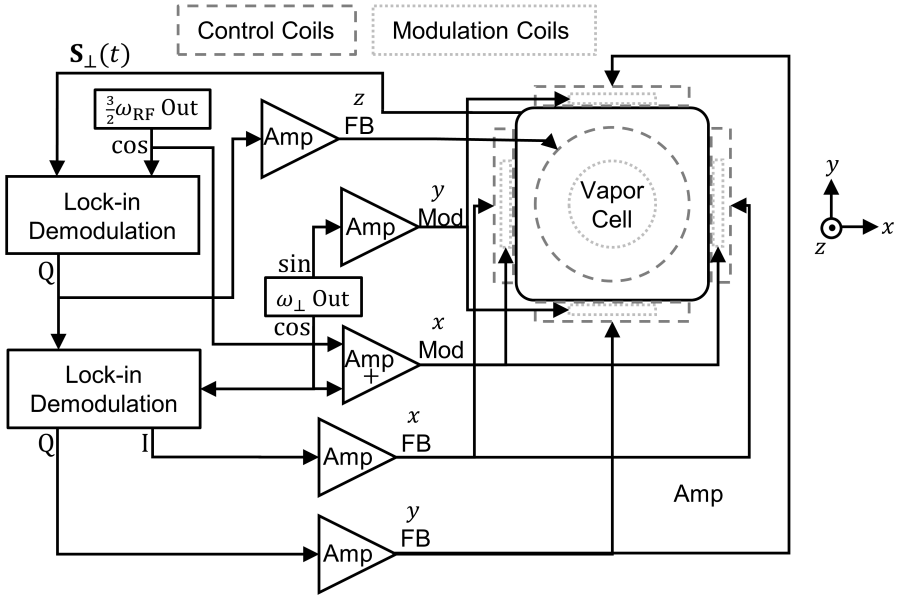

Figure 3.3: Block diagram of our implementation of the OPM variometer. Modulations are applied via the modulation coils in the x and y-directions. The transverse spin signal is demodulated twice. First, the in-quadrature part of the demodulated signal relative to the excitation of ^{87}Rb at $\frac{3}{2}\omega_{\mathrm{RF}}$ is used to derive the total error signal to hold the bias field at the correct value via feedback to the z-direction field control coil. It is then further demodulated at $\omega_\perp$ to obtain signals for feedback to the x and y-direction field control coils. FB: feedback, Mod: modulation, Amp: amplifier, I: in-phase, Q: in-quadrature.

including generating output analog output signals via high-speed output sampling of the waveforms using digital-to-analog converters (DACs), high-speed input sampling of the transverse spin signal using a analog-to-digital converter (ADC), and implementing the cascaded lock-in demodulations and generating feedback signals using a proportional-integral-differential (PID) algorithm. Analog electronics were used for further filtering and buffering of the analog signals, as detailed in Chapter 4. It is technically also possible to completely eliminate the separate modulation coils and instead simply sum all signals to be applied along a given axis together onto the relevant field control coils. However, as we shall also discuss in Chapter 4, separating the modulation signals onto separate coils allows us to introduce analog filtering to

considerably improve the noise performance of the RF OPM.

3.2 Sensitivity and Stability

The sensitivity of the variometer is limited by both the scalar magnetometer on which it is based, and on the amplitude of the rotating modulation from which vector information is derived. In the case of scalar sensitivity, Smullin et al. (2006) used a similar line of reasoning to that presented in Section 2.2.6 to find the fundamental quantum noise limit of a scaler magnetometer to be

$$\delta B = \frac{2(\pi\Gamma_{\mathrm{RF}})^2}{\gamma B_{\mathrm{Mod,RF}}}\frac{1}{\gamma\sqrt{nV}}\sqrt{\frac{4}{(2I+1)(\pi\Gamma_{\mathrm{RF}})}+\frac{R_{\mathrm{PR}}\mathrm{OD}}{2(2I+1)^2(\pi\Gamma_{\mathrm{RF}})^2}+\frac{4}{R_{\mathrm{PR}}\mathrm{OD}\eta}}. \quad (3.12)$$

The first term under the radical comes from spin-projection noise, the second from light-shift noise, and the third from photon shot-noise. Comparison of Equations 2.86 and 3.12 shows that a scalar magnetometer shares some important similarities with an RF magnetometer. Photon shot-noise provides the same contribution to each magnetometer, and both share a characteristic $(nV)^{-1/2}$ scaling, showing that the sensitivity improves with increasing alkali density and sensing volume. We also see that the sensitivity is inversely proportional to the amplitude $B_{\mathrm{Mod,RF}}$ of the field $\mathbf{B}_{\mathrm{Mod,RF}}(t) = B_{\mathrm{Mod,RF}}\cos(\gamma B_0 t)\mathbf{e}_x$ used to drive the RF response of the variometer species. The amplitude of this modulation is ultimately limited by the RF linewidth, as unless $\gamma B_{\mathrm{Mod,RF}} \ll \Gamma_{\mathrm{RF}}$, RF power broadening will begin to degrade the scalar sensitivity. In our case, the frequency will be ^{87}Rb, driven at $3/2\omega_{\mathrm{RF}} = \gamma_{87}B_0$. Fortuitously, if we optimize Equation 3.12 with respect to the off-resonant depumping rate R_{PR} of the probe laser, we simply recover Equation 2.87. So the scalar part of the variomter and the RF magnetometer are simultaneously optimized for the same probe beam parameters, for which the optimized scalar sensitivity of the variometer is

$$\delta B = \frac{4(\pi\Gamma_{\mathrm{RF}})^{3/2}}{\gamma^2 B_{\mathrm{Mod,RF}}}\sqrt{\frac{2}{nV(2I+1)}}. \quad (3.13)$$

If we assume a cell a temperature of 130°C with an RF-optimized linewidth of $\Gamma_{\mathrm{RF}} = 1.5$ kHz, we will have a scalar sensitivity around

$$\delta B \approx \frac{2.76 \times 10^{-22}\ \mathrm{T^2\ Hz^{-1/2}}}{B_{\mathrm{Mod,RF}}}. \tag{3.14}$$

We found it to be best to operate at $\gamma B_{\mathrm{Mod,RF}} = 1\%\Gamma_{\mathrm{RF}}$ to $6\%\Gamma_{\mathrm{RF}}$ for reasons that will be expanded upon in Chapter 4. This means that for for a typical test frequency of $f_{\mathrm{RF}} = 21.5$ kHz with $B_0 = 4.6\ \mu$T, we have an absolute best scalar variometer sensitivity of $\delta B = 15$ fT to 60 fT which corresponds to a stabilization in the value of the scalar field B_0 to one part in 10^7 to 10^8. Across the complete operating frequency of $f_{\mathrm{RF}} \sim 1$ kHz to 1 MHz, we will have a bias field amplitude on the order of $B_0 \sim 0.1\ \mu$T to 100 μT. For the lowest end of the frequency range, this allows for scalar stabilization to at least the order of a part in 10^5, while on the higher end, it can be as high a part in 10^9. The ressonance frequency of ^{85}Rb is stabalized to the order of $\gamma_{85}\delta B \sim 100\ \mu$Hz, which is more than sufficient for our purposes, as this corresponds to a stabilization of the RF frequency within a part in 10^6 of the RF linewidth.

The observable transverse signal $s_\perp$ is given by the magnitude of the amplitude modulation induced on the signal from the scalar magnetometer by the rotating modulation. In the regime of small field errors, where $\Delta B \ll B_0$ Alexandrov et al. found it is given by

$$s_\perp = k_\perp \Delta B \tag{3.15a}$$

$$\begin{aligned} k_\perp &= \frac{B_\perp}{\sqrt{B_z^2 + B_\perp^2}} \\ &\approx B_\perp / B_z \\ &\approx \frac{B_{\mathrm{Mod},\perp}}{B_0}, \end{aligned} \tag{3.15b}$$

where $B_\perp = |\mathbf{B}_\perp(t)|$ is given by Equation 3.10. Combing Equations 3.13 and 3.15a, we see that the best possible transverse sensitivity is a factor of $k_\perp$ smaller than the scalar sensitivity. Unsurprisingly, Equations 3.15a and 3.15b show that the transverse sensitivity increases as the amplitude of the rotating modulation is increased.

However, all the results derived thus far hinge on the assumption that the rotating field remains small compared to the bias field. In their original work, Alexandrov et al. used a value of $B_{\mathrm{Mod},\perp} \approx B_0/10$, selected to have a minimal impact on the long-term stability of variometric measurements. However, we found that this was far too large for our application. In the frequency domain, the rotating modulation manifests as side-bands on the scalar magnetometer signal that are spaced at $\pm\omega_\perp$ from the carrier signal at $3/2\omega_{\mathrm{RF}}$. Such side-bands are necessarily also added to the RF magnetometer signal. Power in the RF signal is re-distributed to these side-bands as $k_\perp$ increases and the depth of the modulation rises. This quickly begins to degrade the SNR of the RF signal. We found it necessary to set $k_\perp < 1/100$ to maintain a high RF sensitivity. More details will be given in the discussion of the integrated system in Chapter 4. Best transverse sensitivity is then on the order of pT $\mathrm{Hz}^{-1/2}$.

The fractional error in the measurement of the scalar value of the magnetic field $B_0 = \sqrt{|\mathbf{B}|^2 - B_\perp^2}$ will be

$$\begin{aligned} \frac{\Delta B_0}{B_0} &= \frac{1}{B_0^2}\sqrt{(|\mathbf{B}|\Delta B)^2 + (B_\perp \Delta B_\perp)^2} \\ &\approx \sqrt{\left(\frac{\Delta B}{|\mathbf{B}|}\right)^2 + \left(\frac{k_\perp \Delta B_\perp}{|\mathbf{B}|}\right)^2}. \end{aligned} \tag{3.16}$$

The first term $\Delta B/|\mathbf{B}|$ under the radical is the long-term stability of unadulterated scalar magnetometer without rotating modulation. Allen and Bender (1972) measured a long-term stability of 0.04 $\mathrm{nT_{RMS}}$ in a Rb magnetometer, limited by high-frequency noise and temperature drift [6]. Brill (1975) improved the high-frequency noise performance but had slightly worse temperature effects, leading to a similar stability [20]. Ware (1983) improved upon these results to achieve a long-term stability of around 0.01 $\mathrm{nT_{RMS}}$ [92]. As we do not go to any effort to optimize the long-term stability, such as using a carefully temperature stabilized coil mounting system, we should err on the higher side to estimate a long-term stability of $\Delta B \sim 0.1$ $\mathrm{nT_{RMS}}$, which corresponds to a long-term frequency stability of $\Delta f_{\mathrm{Long}} \sim 1$ Hz. Fractional

scalar stability is then $\Delta B_0/B_0 \sim 0.1$ nT/4600 nT $\sim 1 \times 10^{-5}$ at our test frequency. The second term describes how the stability is degraded by the presence of the rotating modulation. With $B_0 \sim 0.1$ μT to 100 μT and $k_\perp \sim 10^{-2}$, we find $k_\perp \Delta B_\perp/|\mathbf{B}| \sim 10^{-5}$ $(\text{nT})^{-1}\Delta B_\perp$ to 10^{-8} $(\text{nT})^{-1}\Delta B_\perp$. For the degradation of long-term stability due to the rotating modulation to become comparable to the original stability of the scalar magnetometer, the transverse error field needs to be $\Delta B_\perp \sim 1$ nT to 1 μT. Thus so long as the transverse field is stabilized to below $\Delta B_\perp = 1$ nT, we can avoid noticeable degradation of variometric stability. This is achievable so long as the geomagnetic field does not change fast enough relative to the frame of the variometer to introduce such field errors, as the transverse variometric sensitivity of $\delta B_\perp = k_\perp \delta B_{\text{RF}} \sim$ pT $\text{Hz}^{-1/2}$ is high enough to stabilize low-frequency fields near DC to within this range. Larger transverse field errors due to dynamic motion of the device through geomagnetic fields can be expected to degrade the stability. Chapter 4 discusses tests of dynamic variometer performance.

The total stabilized field intensity is

$$\begin{aligned} |\mathbf{B}(t)| &= \sqrt{B_0^2 + B_\perp^2} \\ &\approx B_0 + \frac{B_\perp^2}{2B_0} \\ &\approx B_0 + \frac{k_\perp B_\perp}{2} \\ &\approx B_0 \left(1 + \tfrac{1}{2}k_\perp^2\right). \end{aligned} \tag{3.17}$$

So the rotating modulation shifts the scalar field amplitude by a relative amount $k_\perp^2/2$. Then the deviation in the total field amplitude due to deviation in the transverse field is given by

$$\frac{\Delta B}{\Delta B_\perp} \approx \frac{k_\perp \Delta B_\perp/2}{\Delta B_\perp} = \frac{k_\perp}{2}. \tag{3.18}$$

In our case with $k_\perp \sim 10^{-2}$, then $\Delta B/\Delta B_\perp \sim 10^{-3}$. The shift in the scalar amplitude measurement introduced by the rotating modulation will be on the order of 0.1 nT. Thus the performance of the scalar part of the magnetometer is minimally

affected by the rotating modulation of the variometer, at the cost of reduced variometric sensitivity. This is more than adequate to stabilize the resonant frequency for operation of the RF magnetometer, so long as deviations in the external field, such as those due to motion of the device, are kept small enough to prevent ΔB from becoming too large and moving outside of the dynamic range of the feedback. From this we see the main limitation of the this approach: dynamic range will be limited by a combination of the chosen values of $B_{\mathrm{Mod,RF}}$, $B_{\mathrm{Mod},\perp}$, and proper optimization of the feedback controller. No matter the situation, the feedback can only stabilize the field in the low-frequency regime near DC where $\omega \ll \omega_{\perp} \ll \omega_{\mathrm{RF}}$. It also cannot handle sudden movements that cause large changes in the single-axis field components ΔB_{μ} in the frame of the device that put them outside of the available dynamic range. Nevertheless, the bandwidth and dynamic range of the device will prove quite sufficient for unshielded application.

3.3 Conclusions

OPM variometry provides us with a technique to stabilize the low-frequency field environment near DC. This in turn allows us to maintain the scalar value of the field such that $\mathbf{B}_{\mathrm{Total}} \approx B_0 \mathbf{e}_z$ near DC. It thus provides a method to allow implementation of the techniques discussed in Chapter 2 in an unshielded environment. In the next chapter, we will discuss the synthesis of these concepts into a single integrated device.

Chapter 4

Experimental Synthesis

In the previous few chapters, we have seen how a high-sensitivity OPM for detection of RF fields can be constructed within an environment with a well controlled bias field and how we may use an OPM variometer to counter the effects of dynamic external field environments to achieve the requisite control of the bias field near DC to enable operation of such an RF OPM. In this chapter, we will now discuss these ideas can be synthesized into a practical sensor. Much of the work in this chapter has already been published [33]. However, a more comprehensive discussion will be presented here.

4.1 Experimental Overview

The overall layout of the experiments detailed in this chapter is shown in Figure 4.1. Some aspects have been already alluded to throughout this work. At the heart of the experiment is a vapor cell provided by Precision Glassblowing Inc (Englewood, CO, US), filled with a small drop of natural abundance Rb metal and nominally filled with 400 Torr of nitrogen gas. A fit to the spectroscopic signal from the D_1 optical transition within the cell was used to determine the real density of nitrogen

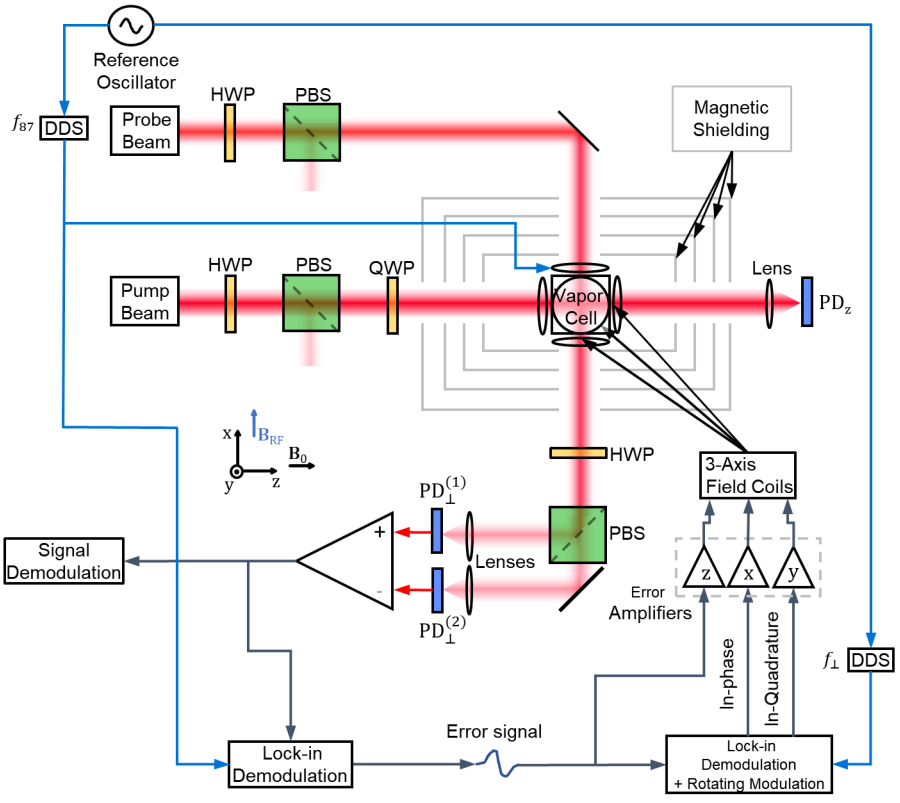

Figure 4.1: High-level diagram of the apparatus used in the experiments detailed in this chapter. Some beam conditioning optics are omitted. DDS: direct digital synthesizer. PBS: polarizing beam-splitter cube. QWP: quarter-wave plate. HWP: half-wave plate. PD_z: z-direction photo-diode. $PD_\perp^{1(2)}$: transverse photo-diodes 1 and 2.

gas within the cell to be $n_{N_2} = 0.471$ amg, which corresponds to a fill pressure of 384 Torr at a temperature of 20°C. See Appendix B.1 for details. Figure 4.2(a) shows a view of a vapor cell manufactured to the same specifications as the one used in the experiment. To heat the vapor cell in order to achieve sufficient vapor density n_{Rb}, 36 AWG twisted-pair phosphor-bronze filament wire of high resistivity from LakeShore Cryotronics (Westerville, OH, US) is wrapped around areas of the cell not required for optical access, and affixed with polyimide (Kapton®) tape. The vapor cell is then placed into a nonmagnetic oven 3D printed from Ultem™1010

filament to withstand high-temperature operation. Between the 3D printed oven and the vapor cell, 3.2 mm thick sheets of polyimide insulation are inserted to increase heat retention and improve thermal efficiency. The four vertical (paralell y) faces of the oven have 8 mm circular apertures with corresponding cutouts in the insulation to allow for optical access to the vapor cell. On the exterior of the oven, there are depressions in the plastic sized to slot in 12.7 mm circular windows. The windows mounts are intentionally tilted by 2° relative to the external faces of the oven to avoid potential negative effects due to unwanted optical feedback from back-reflected light into the laser diodes. Windows from Edmund Optics (Barrington, NJ, US) made from NBK7 at 3 mm thickness and anti-reflection coated on both sides are used within the mounts. The vapor cell mount was also rotated by 3° about the vertical (y)-axis to avoid effects due to back reflections. Figure 4.2 (b) shows how the surfaces are tilted, while Figure 4.2 (c) shows the actual vapor cell mounted within the 3D-printed oven mounted with the PCBs that provide the field control and modulation coils, as detailed in Section 4.4. DC heating would be unsuitable, as despite using twisted-pair heater wire, a residual field magnetic field due to currents through the heater wire is unavoidable. Instead, we use AC heating, provided by driving the heater wire with an amplified sinusoidal signal at 1 MHz, which was determined to be sufficiently large compared to RF frequencies of interest. The entire cell, oven, and control coil assembly is placed within a four layer MS-1L magnetic shield from Twinleaf (Plainsboro, NJ, US) to provide a controlled magnetic field environment for evaluation. Upon initial heating of the cell and oven apparatus, a noticeable film formed on the inside surface of the windows. We attribute this to volatile hydrocarbons in the adhesive of the tape used to affix the heater wire to the vapor cell. To address this issue, the windows were removed and the heater was run at high power over a weekend to drive off any further volatile compounds within the adhesive before the windows were cleaned and re-installed. No visible film was deposited on the interior surface of the windows subsequent to implementing these measures.

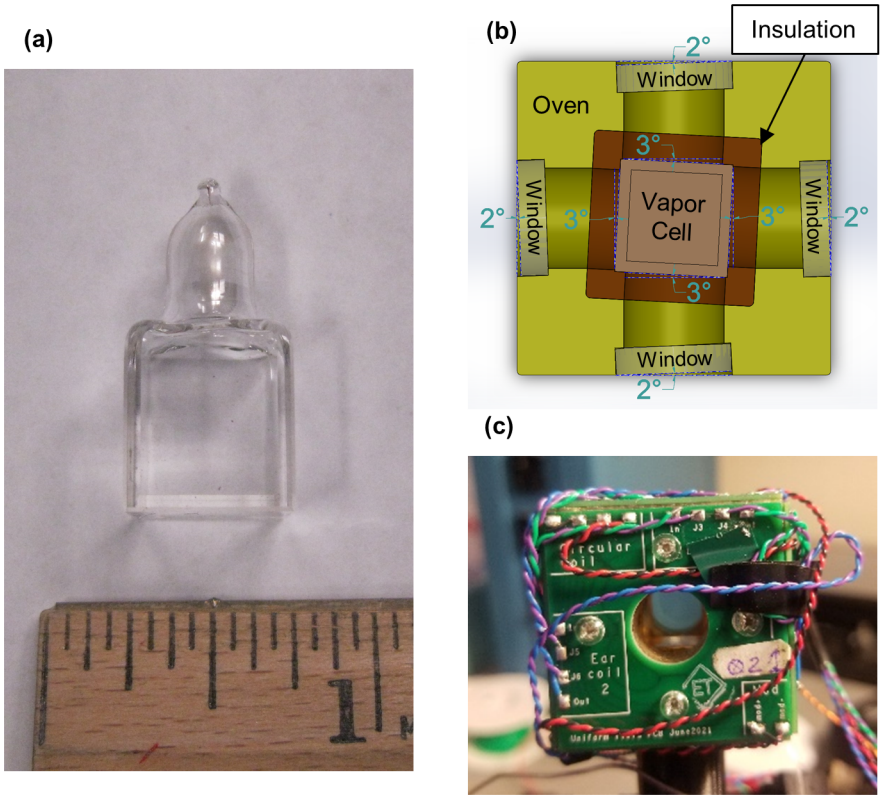

Figure 4.2: The vapor cell and surrounding oven used in these experiments. **(a)** An example cell manufactured to identical specifications as the one used in our experiments. Reference scale in inches. **(b)** Shaded image from *SolidWorks* of a top-down cross-sectional view through the vertical (y-direction) mid-plane of the vapor cell and 3D printed oven used to insulate it. Thin heater wires are on the outer surface of the cell are omitted. **(c)** Fully assembled cell and oven with PCB field coils (see Section 4.4) affixed to the exterior.

Once the cell and heater are assembled into the oven, a type E thermocouple affixed to the fill stem at the top of the vapor cell is used to measure the cell temperature. This should be a good estimate of the effective coldest point in the cell, as a hole in the top of the oven leaves this part of the cell uninsulated; it is exposed directly to the surrounding air. As discussed in Section 2.2.6, the coldest point in the cell sets the alkali density and is the temperature that must be used to determine

the best available sensitivity from Equation 2.88. The amplitude of the sinusoid used to drive the heater is then adjusted to produce an equilibrium cell temperature of $125 - 130°\text{C}$, which corresponds to an optical depth of $25 - 30$. Slight temperature drifts do occur over time, but the temperature remains within a $\pm 3°\text{C}$ range for our experiments in the laboratory.

4.2 Optics

Figure 4.1 gives an overview of the optical layout. The pump beam is supplied by a laser diode utilizing distributed feedback (DFB) from Eagleyard Photonics (now Toptica-Eagleyard, Berlin, DE). The probe beam is provided by a diode using a distributed Bragg-reflector (DBR) from Vescent Photonics (Golden, CO, USA). Both are collimated to a small $1/e^2$ diameter of 2 to 3 mm by the optics integrated into the respective laser modules. To increase the size the beams to more fully utilize the available volume of the vapor cell, telescopes expand the collimated pump and probe beams to a $1/e^2$ diameter of about 10 mm and 8 mm respectively. A smaller size for the latter was selected to reduce unwanted distortion of the probe beam within the vapor cell due to diffraction from the beam clipping the apertures of the wave plates and cell oven. In addition, the elliptical pump beam is passed through an anamorphic prism pair to render the beam nearly circular before telescopic expansion. To set optical powers within the vapor cell, the beams are passed through half-wave plates (HWP) from Tower Optical (Boyton Beach, FL, US) and a polarizing beam-splitter cube (PBS) from ThorLabs (Newton, NJ, US). Light transmitted through the PBS has a linear P polarization parallel to the x-direction, while extra power in the beam is "dumped" into the S polarized reflected direction (parallel to the y-direction) that we do not utilize. In the transmitted direction, the extinction ratio of transmitted power $T_{\text{S(P)}}$ in each polarization component is $\text{T}_\text{P} : \text{T}_\text{S} > 1000 : 1$ [85], leading to a good polarization purity. An additional quarter-wave plate (QWP) also from

Tower Optical is used on the pump beam to rotate it into a circular polarization that combines with the bias field within the vapor cell to drive σ_+ transitions that optically pump the atoms to the stretched as described in Section 2.2.2. The probe beam retains a linear polarization which undergoes Faraday rotation as it passes through the vapor cell as described in Section 2.2.5. An additional HWP and PBS are used to form a balanced polarimeter along with a Newport (Andover, MA, US) 2107 balanced photo-detector (BPD) for the transverse photo-diodes and associated trans-impedance amplification. The pump beam is tuned to resonance by scanning the temperature of the diode and setting its driving current to place the signal from the z-direction photo-diode at the center of the absorption dip due to D_1 resonance. Power in the pump beam is optimized by scanning the RF driving frequency over resonance at a fixed bias field, or scanning the bias field over resonance at a fixed RF frequency, and using the RF resonance signal from the BPD to minimize the RF linewidth to ensure we are in the regime of optimal light-narrowing, as described in Section 2.2.6. Power and detuing of the probe beam are optimized in accordance with Equation 2.52 by driving the RF resonance using the x-direction field coil included within the magnetic shield and optimizing the SNR in the frequency domain using a fast Fourier transform (FFT) spectrum analyzer. Probe beam detuing was found to be optimal at $\Delta\nu \sim 1.5$ to 3 Γ_{Tot}, in agreement with the predictions shown in Figure 2.14.

4.3 Electronics

In addition to the optical layout, Figure 4.1 gives an overview of the electronics in our experiment, shown by dark blue connections, used to measure the optical signal, and to implement feedback control variometry using ^{87}Rb as detailed in Chapter 3. As mentioned previously, this experiment contrasts with the original work on OPM variometers by Alexandrov et al. [4, 3] in using a mixed analog and digital approach,

rather than a fully analog implementation. This allows for more flexibility in the design of the control architecture. In this section, both analog and digital aspects of the electronics will be described in detail.

4.3.1 Digital Electronics

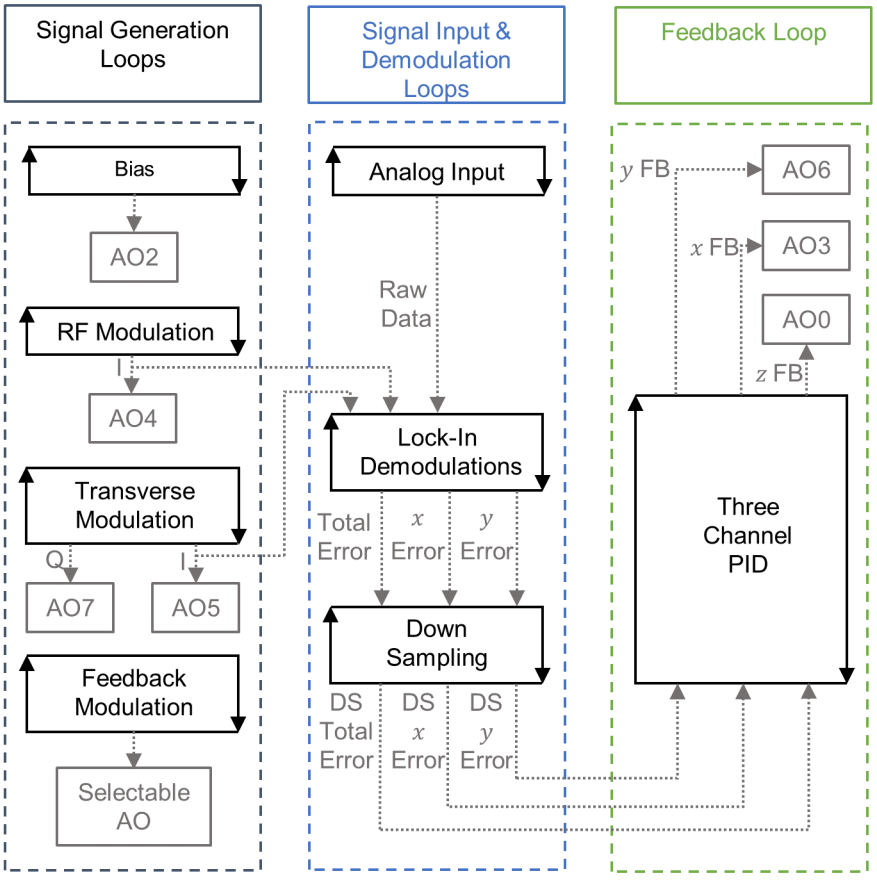

Figure 4.3: Diagram of the digital control structure showing loops executing in parallel on the FPGA. Loops shown in the left column generate various outputs. Loops shown in the center column handle data acquisition and processing. The final loop shown in the right column provides feedback control signals to drive the field control coils. AO: analog output. DS: down-sampled. FB: feedback. I: in-phase. Q: in-quadrature

Data acquisition is performed with a Measurement Computing (Pullman, WA, US) USB 1602HS data acquisition (DAQ) device powered by a 16 bit analog-to-digital converter (ADC). An FFT spectrum analyzer is implemented using this device via a program in LabVIEW to gather data in the frequency domain.

At the heart of the digital side of our control platform is an NI (formerly National Instruments, Austin, TX, US) PXIe-7857 re-configurable input/output (I/O) module. It is powered by a Kintex-7 160T field-programmable gate array (FPGA) providing eight analog input (AI) channels via dedicated 16 bit ADCs, and eight analog output (AO) channels via dedicated 16 bit digital-to-analog converters (DAC)s. The FPGA runs on a 100 MHz clock integrated into the PXIe system [26]. Each analog I/O channel has a range of ± 10 V and can sample at a rate of up to 1 MHz $= 10^6$ Samples s^{-1}. The FPGA is programmed via NI's LabVIEW FPGA software. Our PXIe system consists of the FPGA module slotted into a PXIe-1062Q chassis that is controlled remotely via a PC using a Thunderbolt link through a PXIe-8301 remote control module that is also connected to the chassis. This system allows the I/O module to be fully controlled via the control computer. A slower "host" program runs on the control computer to provide a graphical user interface (GUI) for the operator to set various experimental parameters such as the sensing frequency, and the amplitude of the rotating modulation. These parameters are passed to a program executing much more quickly on the FPGA, which samples the analog input data from the magnetometer, and implements the variometer control structure discussed in Chapter 3.

Figure 4.3 shows a diagram of the structure of the program as it executes on the FPGA. Four loops, shown in the left column of Figure 4.3, generate analog outputs to drive various aspects of the magnetometer. The first supplies a voltage to create a constant bias field along the z-direction, holding a constant value unless the desired sensing frequency is altered by the user. It assumes a linear dependence of bias field (and thus RF frequency) on driving voltage and uses a calibration value found

from optimizing the RF resonance signal from ^{85}Rb at 21.5 kHz. The second output loop produces the RF signal to drive the resonance of ^{87}Rb at $\frac{3}{2}f_{\mathrm{RF}}$. Because we did not anticipate operating at an RF frequency above $f_{\mathrm{RF}}^{(\mathrm{Max})} = 50$ kHz in these experiments, this loop executes at a sampling rate of 500 kHz to over-sample the RF output by at least a factor of five. Amplitude of the RF sinusoid is controlled by via the GUI on the control laptop. The third loop generates the in-phase (cos) and in-quadrature (sin) sinusoids that drive the rotating modulation variometric modulation in the transverse plane. In these experiments, we operate at a maximum rotating modulation frequency of $f_{\perp}^{(\mathrm{Max})} = 1$ kHz $\ll f_{\mathrm{RF}}$, so we operate this loop at a sampling rate of 10 kHz to ensure at least a factor of five over-sampling for these signals as well. The fourth loop optionally generates a user-selectable output waveform (sinusoid, triangle, or square wave) with user controlled frequency (up to 1 kHz), amplitude (up to 10 V), and phase. This signal is summed in the digital domain with the aforementioned RF and/or rotating modulation signals applied to the field modulation coil of the selected channel. This is useful for fine tuning various aspects of the experiment, such as the bias field, and optimizing feedback parameters. Because this loop is synced to the output of the field modulation coils, it is sampled at 1/50 the data input sampling rate to match the rate of feedback output as discussed below.

Another set of three loops, shown in the center column in Figure 4.3 handles analog data input sampling and processing. The first uses a 16 bit ADC to sample analog data from the balanced polarimeter. This DAQ loop samples at 500 kHz to ensure at least a factor of five over-sampling of frequency components up to 50 kHz. These data are then passed to the second loop, which implements the cascaded lock-in demodulations required for variometry. A distinct benefit of the FPGA manifests here: because the modulations are generated from the same clock, no external phase reference is required; phase references from the modulation generation loops are simply available within the FPGA. The first stage lock-in is phase-locked with a user

controlled phase offset to the RF modulation that excites ^{87}Rb. Output from this first stage is then split into two channels. The first is low-pass filtered with user controlled cut-off frequency to obtain the total error signal, with amplitude modulations at $f_\perp$ removed. This provides the scalar variometer error signal, which is used to provide feedback control for the z-direction field control coil. The second is high-pass filtered to isolate the amplitude modulations at $f_\perp$ due to the rotating modulation combined with external field changes. This signal is passed into the second-stage lock-in that is phase-locked to the rotating modulation at $f_\perp$, again with a user controlled phase offset. The in-phase and in-quadrature output of this second stage lock-in provide the signals used to provide feedback control for the x and y-direction field control coil respectively. The third loop down-samples by a factor of fifty to match the rate of incoming data to the execution speed of the final loop.

The final loop, shown in the right column of Figure 4.3 implements a proportional-integral-differential (PID) feedback servo control algorithm using the error signals derived in the preceding steps to produce feedback control signals to drive the tri-axial field control coils and cancel the effects of external fields and enable high-sensitivity operation of the RF magnetometer. Proportional (P), integral (I), and differential (D) feedback gains are set individually by the user for each channel. This loop executes a factor of fifty more slowly than data acquisition, meaning a rate of 10 kHz. Because this is still a factor of ten larger than $f_\perp^{(\mathrm{Max})}$, and feedback can only act at frequencies $\ll f_\perp$, this does not degrade the usable feedback bandwidth.

4.3.2 Analog Electronics

The FPGA platform provides a fast and versatile platform to handle data I/O operations. However, it cannot provide sufficient current to drive the field control coils, and the finite sampling rate of its inputs and outputs can lead to signal artifacts above the Nyquist frequency. For these experiments, we set the BPD to a trans-

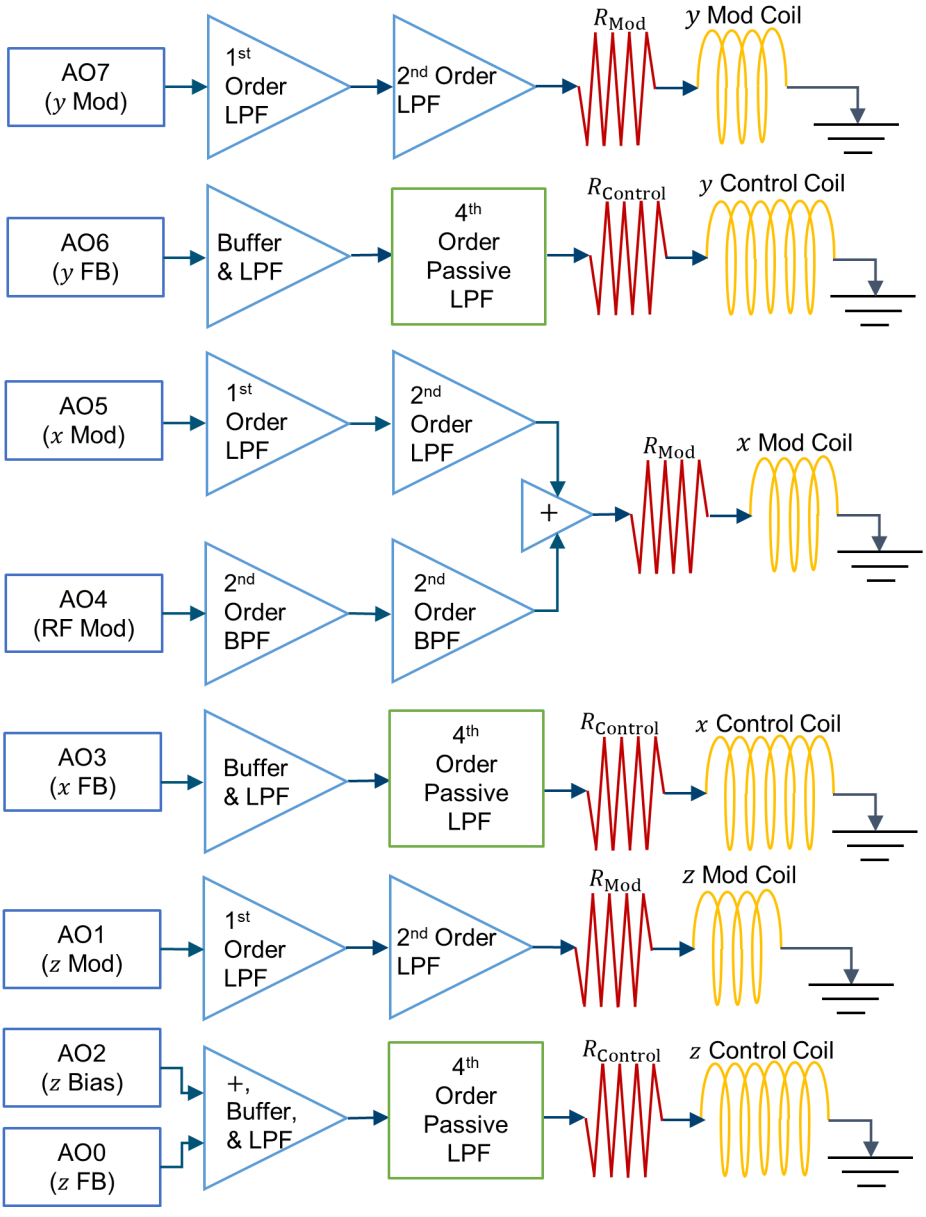

Figure 4.4: High-level Layout of the analog output electronics. Operational amplifiers provide current buffering between the analog FPGA outputs and field control coils and provide reconstruction filtering. Fourth-order passive low-pass filters bandwidth limit noise noise above 1 kHz. Triangles indicate operational amplifiers. AO: analog output. FB: feedback. Mod: modulation. LPF: low-pass filter. BPF: band-pass filter. +: analog summation.

impedence gain of 630×10^2 V A^{-1} in order to bring the optical noise to a level above the electronic noise floor of our sampling electronics, allowing us to resolve the quantum noise limit. The BPD has a built in low-pass filter, which we set to a cut-off frequency of 100 kHz to remove unwanted higher frequency noise, such as the effects from the 1 MHz heater. It also has a high-pass filter, which we set to a cut-off frequency of 1 kHz to remove low frequency content near DC, including any DC offset.

Figure 4.4 provides a diagram of the analog electronics that interface analog outputs from FPGA to the magnetic field coils implemented on printed circuit boards (PCBs) as detailed in Section 4.4. The purpose of these electronics is fourfold: as mentioned, the DAC outputs from the FPGA cannot naively drive sufficient currents for field control coil operation. To address this, operational amplifiers (op-amps) are used to provide buffers that allow for sufficient current drive. Secondly, the op-amps allow a convenient method to sum together multiple signals simultaneously on a single channel. This is used on the B_z field control coil to sum together the bias field and feedback control, as well as on the x-direction field modulation coil, to sum together the signal to drive ^{87}Rb for the scaler part of the variometer with the in-phase part of the rotating variometric modulation. Thirdly, the op-amps provide a convenient avenue for reconstruction filtering to remove digitization artifacts on the DAC outputs from the FPGA due to the finite output sampling rate.

Finally, we must address noise from the FPGA and relatively high current drive op-amps. Voltage noise density δV that is present across the field control coils with impedance Z_{C} will be converted to a current noise density $\delta I = \delta V / Z_{\mathrm{C}}$. This current noise will then couple with the magnetic field gain G_{B} of the field control coils to produce a magnetic noise density due to the coil of $\delta B_{\mathrm{C}} = G_{\mathrm{B}} \delta I$. Our field control coils have a relatively high gain of $G_{\mathrm{B}}^{(Control)} = 269$ nT mA^{-1} as discussed in Section 4.4. A current noise density of $\delta I \sim 10$ pA $\mathrm{Hz}^{-1/2}$ through this gain will then produce a magnetic field noise density on the order of fT $\mathrm{Hz}^{-1/2}$,the same order as

the quantum limit seen in Equation 2.52 and Figure 2.14. For the measured coil impedance of $Z_{\mathrm{C}} \sim 10\ \Omega$, this corresponds to a voltage noise density on the order of 10^2 pV $\mathrm{Hz}^{-1/2}$, which is well below the typical output noise for even the lowest noise op-amps, which is on the order of 1 to 10 nV $\mathrm{Hz}^{-1/2}$. To address this and prevent amplifier noise from dominating, we use fourth-order passive low-pass ladder filters with a cut-off frequency of 1 kHz between the output of the buffer op-amps and the control coils. In this configuration, the output voltage noise spectrum of the op-amp will experience a much higher impedance at the RF frequencies of interest, and current noise densities across the field-control coils are brought to a level comparable to the quantum noise floor within our sensing bandwidth. Output resistors denoted by R_{Control} & R_{Mod} combine with the resistance of the field control and modulation coils to set the voltage-to-current conversion of the field coils. Because the requisite modulation fields are much smaller than those needed for field control, $R_{\mathrm{Mod}} = 4.7\ \mathrm{k}\Omega \gg R_{\mathrm{Control}} = 12\ \Omega$ which combined with the much lower modulation coil gain of $G_{\mathrm{Mod}} = 46$ nT mA^{-1} prevents op-amp voltage noise coupled in through the modulation coils from becoming a concern. The much greater impedance and smaller gain lead to magnetic field noise density on the order of $\delta B \sim 10^{-2}$ fT $\mathrm{Hz}^{-1/2}$ orders of magnitude below the quantum noise limit.

4.4 Magnetic Field Coils

The feedback scheme outlined in Chapter 3 and the proceeding sections in this chapter requires a set of tri-axial magnetic field control coils. In the worse case, where the geomagnetic field is opposite the desired bias field, these field control coils must be able to produce field amplitudes on the order of the geomagnetic field of Earth, plus the requisite bias field, which for operating frequencies on the order of 100 kHz corresponds to a control field amplitude on the order of 100 μT. We also wish for the coils to produce a highly uniform field distribution to avoid broadening of the RF res-

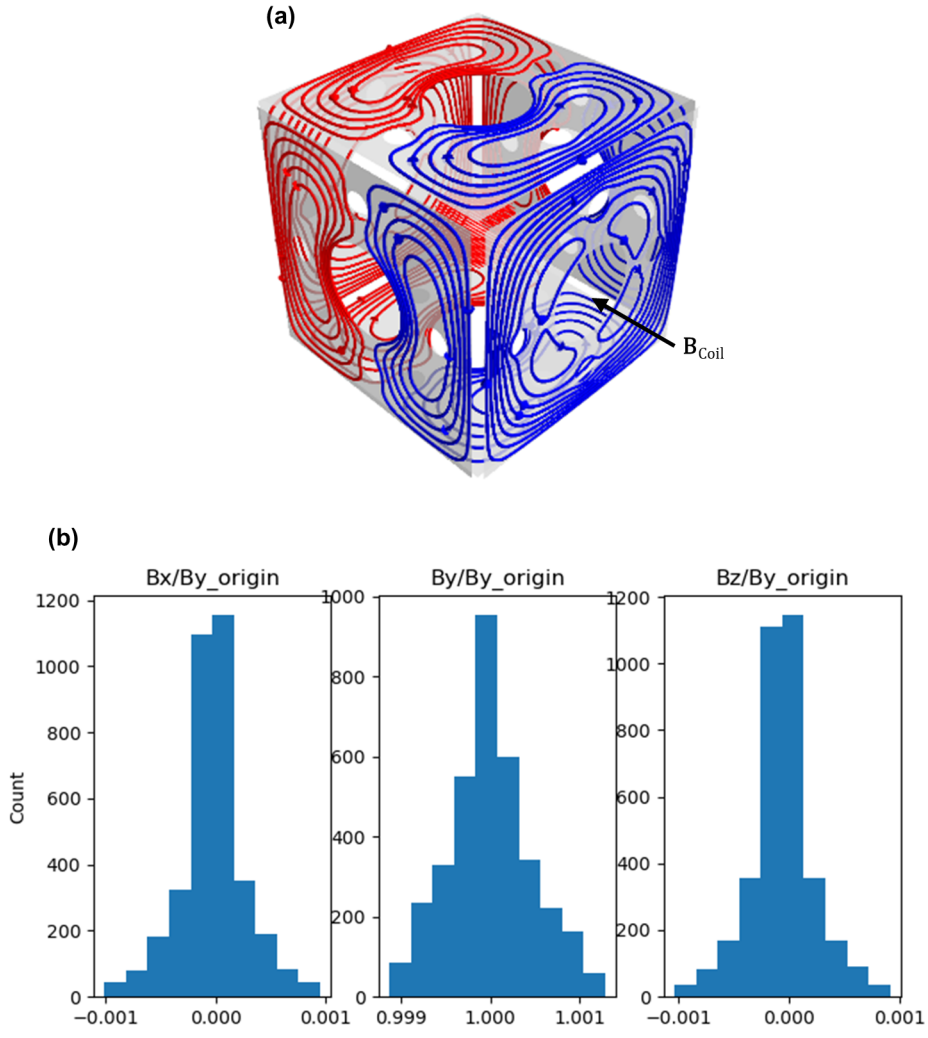

Figure 4.5: Details of the current distributions produced by the magnetic field coils used in our apparatus. **(a)** Surface current distribution over all six cubic faces to produce optimized field strength and uniformity in the indicated direction. Colors code indicate the handedness of current flow, with blue for clockwise about the outward surface normal, and red for counterclockwise. **(b)** Histograms from *bfieldtools* showing the uniformity of the magnetic field produced by the y direction (vertical) field control coil along each of the independent axes. Values in each bin are the number of counts of field intensity relative to the field generated at the center of the cube as a function of position within the discretized volume. This uniformity is predicted to be similar for all three directions.

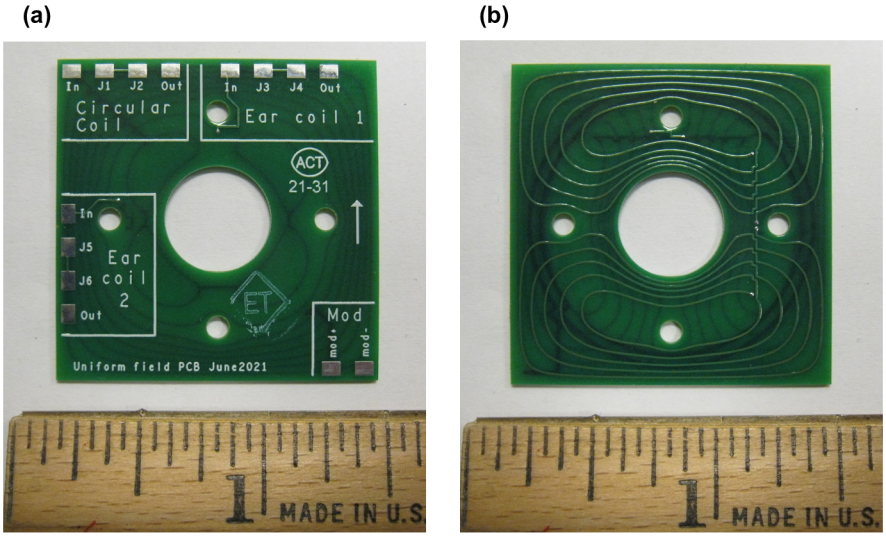

Figure 4.6: **(a)** and **(b)** Front and back views of the four-layer PCBs affixed to each face of cubic cell oven to implement the surface current distribution shown in (a) along each axis, along with an additional circular trace to generate modulation fields. Reference scale in inches. The oven assembly with PCBs affixed and connected is shown in Figure 4.2 (c)

onance line due to magnetic field inhomogeneity that would degrade the sensitivity. A set of Helmholtz coils that meets these requirements would have a large diameter of around 1 m on each side, leading to a cumbersomely large device. To avoid this, we opted to use the open source *bfieldtools* package [66, 97] to design compact coils that fit onto the six exterior faces of our 3D printed cubic cell oven. *bfieldtools* was used to compute a surface current distribution over the six available faces of the cube that maximizes resultant magnetic field amplitude along a given direction within the cube volume while maintaining high field uniformity and leaving a space for optical apertures as shown in Figure 4.5 (a). Current distributions designed in *bfieldtools* in this manner were realized on six-layer printed circuit boards (PCB)s. All six faces of the cube produce currents for generating control fields along each direction. Four layers contain conductive traces to implement the requisite surface currents. Of these, three are used to implement the control fields, while one is a smaller roughly

circular trace used to provide the dedicated modulation coils. Control field coils are assembled by connecting the proper PCB layer for the required current distributions in series using 32 AWG twisted-pair wire. Care was taken in the design of the solder pads that interface to the wires to ensure stray magnetic fields from the connection traces were at least partially canceled by the field of the connected wire above it. The completed cell oven, with field control coil PCBs affixed, is shown in Figure 4.2(c).

As designed, *bfieldtools* predicts the the gain of the main direction control coils to be 271 nT mA^{-1} with a field norm and field vector homogeneity of 0.35%. The field modulation coils were predicted to have a gain of 47 nT mA^{-1} when two opposite faces on the cube are connected in series. We tested the completed coils by driving a DC current through the coils using a precision current source from DM Technologies (Liszki, PL, EU) and measuring the shift in the Larmor resonance frequency as described in Appendix B. Using this method, we find a field control coil gain of 269 ± 0.5 nT mA^{-1}*.This 0.74% decrease can likely be attributed to imperfections in the geometry due to manufacturing errors in the 3D printed oven and field coil PCBs. Gain of the modulation coils was likewise found to be $G_{\mathrm{Mod}} = 46 \pm 0.9$ nT mA^{-1}, 2% below the predicted value, but with a slightly higher uncertianty due to the smaller field amplitudes used in the test.

4.5 System Evaluation

For evaluation, "external" fields were applied using the tertiary set of tri-axial field coils built into the magnetic shield. Such external fields include an a calibrated RF field at known strength B_{Test}† to evaluate the system sensitivity, along with low-frequency fields near DC to test the ability of the servo the respond to fields fields

*Uncertainty from 95% fit confidence

†See Appendix B for details of the calibration procedure.

along each direction. For these tests, an RF test frequency of $f_{\mathrm{RF}} = 21.5$ kHz was selected. Frequency spectra were gathered by sampling at a rate of 500 kHz in the time domain to gather 500 k samples per shot using a Hanning window. This produces an FFT frequency spectrum with 1 Hz resolution over a DC to 250 kHz bandwidth.

4.5.1 Servo Performance

Servo performance was manually optimized by applying a square wave modulation sequentially to each channel and observing the feedback response. First, the proportional (P) term was increased until the feedback began to oscillate. Then the integral (I) term was increased to make the response as fast as possible without introducing further oscillation. Both terms were then iteratively adjusted to minimize both the rise time and oscillation amplitude to find the best approximation of a critically damped response. Finally, the differential (D) term was used to minimize any residual overshoot and oscillation.

After optimizing the servo parameters for each channel, we tested that the servo could successfully cancel external fields by applying magnetic fields along each of the three orthogonal directions. The directions of the PCB field control coils were nominally aligned with the axes of the coils included within the magnetic shield, but due to small mounting errors there may have been slight misalignment between them. The coils included in the shield have a gain of 130 nT mA^{-1} in the longitudinal (z)-direction, and 69 nT mA^{-1} along the transverse (x and y)-directions [89]. We drove these coils with the maximum current available from our precision current source, which can provide up to 40 mA per channel from eight total channels to produce a total of 320 mA of current. Thus we can produce DC fields of up to 41.6 μT in the longitudinal direction and 22 μT in the transverse directions. Currents were slowly ramped from 0 to the full 320 mA to keep the test fields in the near DC regime.

During this test, the variometer servo was able to successfully cancel the effect of the external field and maintain the desired bias field. This confirms our feedback can successfully compensate for DC fields on the order of geomagnetic field at $\sim 10\ \mu$Ts along all three independent axes. Dynamic performance was evaluated by introducing a small amplitude square wave generated on the FPGA and applied successively to each channel through its dedicated modulation coil. The normalized step response of the error signal was then measured to determine the feedback bandwidth for that channel by fitting it to the function

$$F(t) = A\left(1 - e^{-2\pi \mathrm{BW}_n \Delta t}\right), \tag{4.1}$$

where A is the amplitude, BW_n is the feedback bandwidth for channel $n \in \{x, y, z\}$, and $\Delta t = t - t_0$ is the elapsed time. Feedback bandwidths for each channel determined using this method are shown in Table 4.1. Figure 4.7 shows the normalized step response of the error signals, along with the fit from Equation 4.1 used to extract the feedback bandwidths. Because the step response of the system can be used to easily extract the transfer function in the Laplace domain [47], this method serves as a good characterization of the frequency response of the servo system. Another useful metric of system performance is provided by the slew rate of the system, defined as the maximum magnetic field change per unit time that can be sustained before the servo fails. We evaluated this by applying an external field which was linearly ramped in amplitude over 1 s along each axis, and gradually increasing the ramp amplitude until the servo could could no longer track the rate of field change, causing failure of the feedback servo. Results were double checked by increasing to a ramp over 2 s and doubling the amplitude. Both tests were in agreement. Slew rates determined using this method are also shown in Table 4.1.

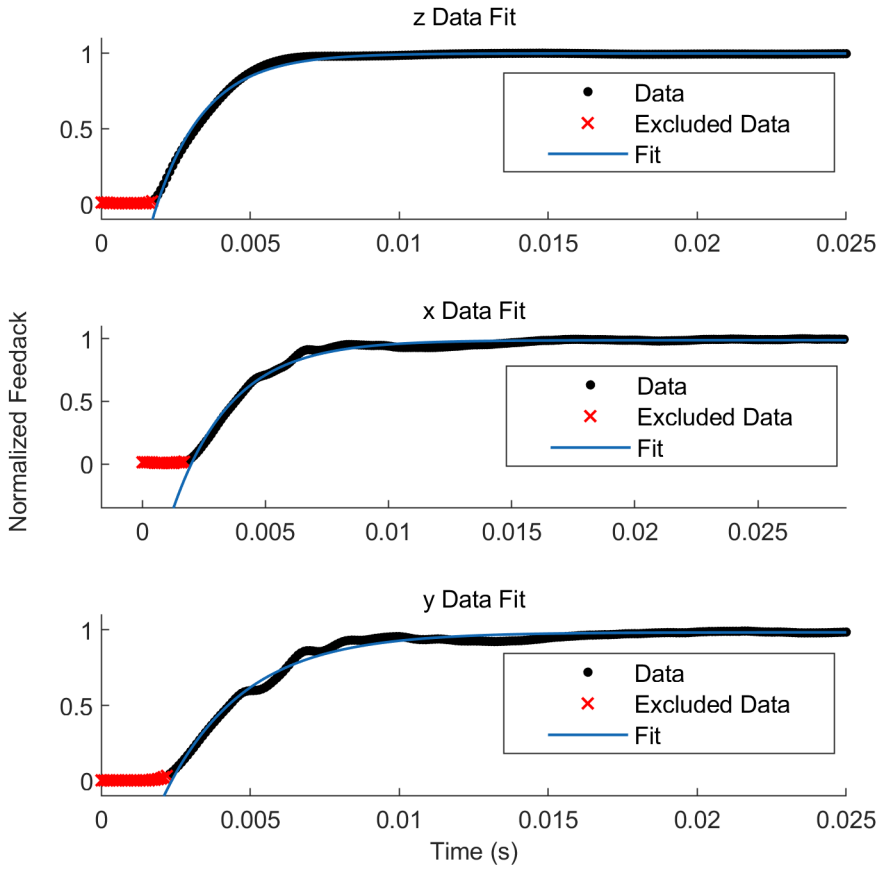

Figure 4.7: The step response of each channel of the servo to the rising edge of a 20 Hz square wave. Fits used to determine the feedback bandwidths are also shown. Data are averages over 100 individual shots.

4.5.2 Magnetometer Sensitivity

To evaluate the variometric sensitivity, a 1 Hz sinusoidal test signal of known amplitude $B_{\mathrm{Test,V}}$ was applied via each of the modulation coils. The level $\Delta\mathcal{E}_n(1\ \mathrm{Hz})$ of the open-loop error signal above background at 1 Hz was then measured and compared to the noise level in the low-frequency error signal near DC $\delta\mathcal{E}_n(10\ \mathrm{Hz})$. Both the signal and noise levels were averaged over 100 shots using power spectral densities. The variometric sensitivity $s_{\mathrm{V,n}}$ along each axis is then calculated by dividing the noise density $\delta\mathcal{E}_n(10\ \mathrm{Hz})$ near DC by the measured response of the system to the

Direction (n)	Feedback Bandwidth BW_n (Hz)	Feedback Slew Rate (μT s^{-1})	Variometer Sensitivity $s_{V,n}$ (pT Hz$^{-1/2}$)
z	96	33	5.8
x	67	8	1000
y	60	8	1300

Table 4.1: Experimentally determined bandwidth, slew rate, and sensitivity for each direction of the variometer. These values are heavily dependent on optimization of the PID parameters, the amplitude of ^{87}Rb excitation, and the variometer sensitivity $s_\perp$ (see Chapter 3). In general, increasing variometer sensitivity to improve response rates also degrades the SNR of the RF magnetometer due to signal power being lost to sidebands of increasing relative amplitude.

calibrated field $\Delta\mathcal{E}_n(1\text{ Hz})/B_{\text{Test,V}}$:

$$s_{V,n} = \frac{\delta\mathcal{E}_n(10\text{ Hz})}{\Delta\mathcal{E}_n(1\text{ Hz})/B_{\text{Test,V}}}. \tag{4.2}$$

Results are shown in Table 4.1. Sensitivity is considerably better along the longitudinal direction, limited primarily by the amplitude of the RF drive used to excite ^{87}Rb for the scalar part of the variometer, which we kept at $B_{\text{RF,Mod}} = 18.4$ nT or $\gamma_{85}B_{\text{RF,Mod}} \approx 6\%\Gamma_{\text{RF}}$ for this experiment. Sensitivity in the transverse plane is limited by both the aforementioned RF drive amplitude and the amplitude of the rotating variometer modulation, which was set at $B_0/100$, corresponding to $s_\perp \approx 1/100$. Measured longitudinal sensitivity is sufficient to stabilize the bias field to one part in 10^6, or on the order of 10 mHz resonance frequency stability. Transverse sensitivity is sufficient to stabilize the bias field to one part in 10^3, or on the order of 1 Hz frequency stability. Since both are far below the measured linewidth of around 1.5 kHz, this is quite sufficient for our purposes, but it is worse then the fundamental limits on variometric discussed in Section 3.2 for undetermined reasons.

RF sensitivity at a given test RF test frequency f_{RF} is determined similarly by applying a calibrated sinusoid of amplitude $B_{\text{Test,RF}}$ at the RF test frequency and calculating the ratio of RF voltage noise density of the signal $\delta V(f \approx f_{\text{RF}})$ to the voltage response $\Delta V(f_{\text{RF}})/B_{\text{Test,RF}}$ of the system to the calibrated field. Thus the

RF sensitivity of the OPM is:

$$\delta B_{\mathrm{RF}} = \frac{\delta V(f \approx f_{\mathrm{RF}})}{\Delta V(f_{\mathrm{RF}})/B_{\mathrm{Test,RF}}}. \tag{4.3}$$

RF OPM sensitivity was first tested in an open-loop configuration; the variometer was not utilized, so the only fields present were the longitudinal bias field and RF test signal. Bias field strength was tuned to center the RF resonance peak at the RF test frequency. Results of this test are shown if Figure 4.8 (a). In this ideal situation, experimental sensitivity is around $\delta B_{\mathrm{RF}} \approx 8$ fT Hz$^{-1/2}$. This is above the predicted quantum noise limit seen in Figure 2.14 using the measured value of Γ_{RF}. It worth noting that this is very near the thermal noise density limit for the magnetic shield used in this experiment at our test frequency [89]. Thus thermal noise from the shield may be limiting the noise floor. There also remains an unexplained offset in Γ_{RF} that brings the quantum noise above the fundamental limits predicted by Equation 2.88, and shown in Figure 2.15. In the second test of RF sensitivity, variometric feedback was activated, and the servo loop was closed to remove any residual fields within the magnetic shield. Results are shown in Figure 4.8 (b). Sensitivity decreases slightly to around 9 fT Hz$^{-1/2}$ compared to the idealized conditions. We attribute this to current noise introduced by the field control coils in the transverse directions. Some residual thermal noise is present at RF frequencies, despite the aforementioned efforts to filter it. Because the thermal current noise density of an impedance Z has the form $\sqrt{4k_BT\mathrm{Re}(Z)}/Z$ where k_B is the Boltzmann constant and T is the absolute temperature, this noise will not depend on the magnitude of the currents applied through the coils. Noise contributions from the active electronics of the op-amps are likewise independent of applied currents. Only the current shot noise density, which is given by $\delta I_{\mathrm{Shot}} = \sqrt{2q_e|I_{\mathrm{C}}|}$ depends on the current I_{C} applied through the coil [27]. However, even for the maximum currents of $I_{\mathrm{C}}^{(\mathrm{Max})} = 300$ mA designed to be applied through the coils, this amounts to a current noise density on the order of 10^{-7} mA Hz$^{-1/2}$ which produces magnetic noise densities on the order of 10 fT Hz$^{-1/2}$. These noise currents are then attenuated at RF frequencies by the

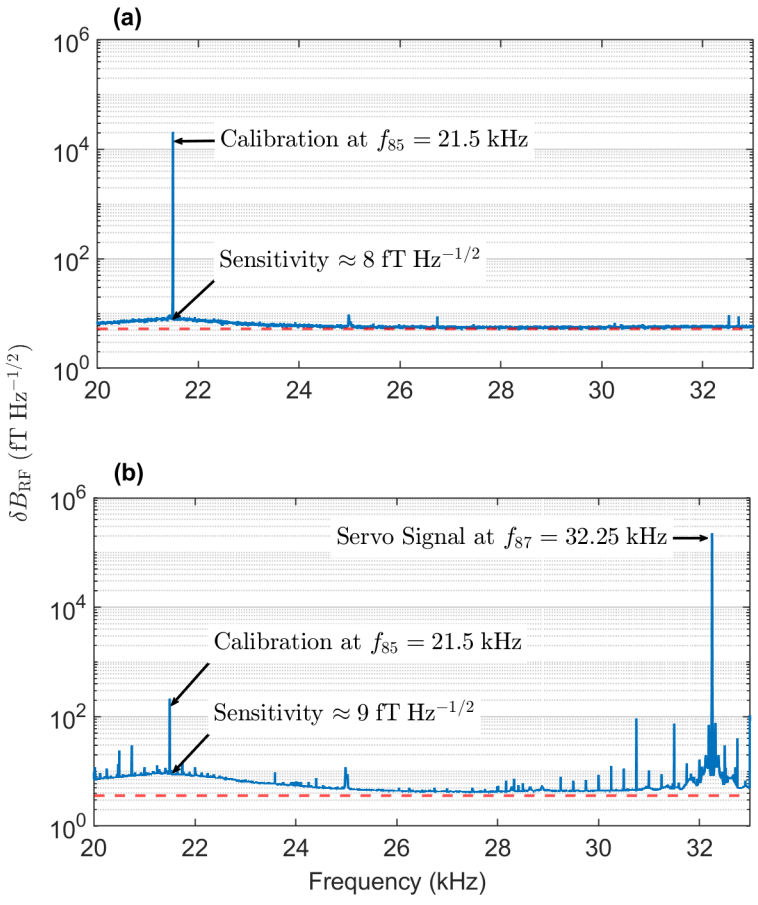

Figure 4.8: Data showing the performance of our test system. Blue solid lines show the magnetic noise floor. Orange dashed lines show an estimate of the photon shot noise limit based on the DC levels measured on the BPD and converted into magnetic field units. Because a calibrated field is used for calculation of spectral magnetic values, only values near the calibration frequency are an accurate representation of RF sensitivity. **(a)** Operation in the magnetic shield with only a static bias field applied. **(b)** Performance with the full optimized servo system engaged to cancel out residual fields inside the shield. Current noise from the transverse field control coils slightly increases the magnetic noise, but shield noise is still dominant. Small spurs occur at multiples of 60 Hz and $f_{\perp}$, along with their sums and differences. Spectra shown are averages over 500 shots

passive filtering to a level far below the quantum noise limit. Thus we conclude that noise contribution from the field control coils will remain small, and similarly high RF OPM sensitivity can be achieved even when the field control coils are engaged

outside of a magnetic shield. As expected, the RF signal seen in the spectrum in Figure 4.8 also contains side-bands on either side of the scalar variometer drive at $f_{87} = \frac{3}{2} f_{\mathrm{RF}} = 32.25$ kHz due to the rotating modulation at frequency $f_{\perp}$. They would be present on the RF OPM signal as well, but are too small to be seen above the noise floor. In addition, there are various "spurs" on either side of both resonances at frequencies of the form $f_{\mathrm{Spur}} = f_{\mathrm{Center}} + n \times 60$ Hz $+ m f_{\perp}$ where n and m are integers. These spurs can be minimized by reducing the amplitudes of the scalar variometer drive and rotating modulation, at the expense of reduced servo performance. Variometer parameters are ultimately selected by maximizing these drive amplitudes to the greatest extent possible before RF SNR begins to quickly decrease.

4.6 Conclusions

In this chapter, we have develped an experimental platform to implement an RF OPM as described in Chapter 2 based on ^{85}Rb using variometric feedback derived from^{87}Rb within the same vapor cell to actively stabilize the field environment near DC. The servo system based on this *comagnetometer* has been shown to be able to compensate fields on the order of the geomagnetic field of Earth, and provide sufficient dynamic performance compensate low-frequency fields from DC to around 60 kHz. We have also seen that even with the servo engaged, high RF sensitivity can be maintained. This provides us with a direct path toward completely unshielded operation of our OPM while maintaining high RF sensitivity.

Chapter 6

Conclusion

A great many discoveries and ideas in physics come with the promise of eventual application. The vast majority never realize such lofty dreams. Development of a physically possible idea into a useful technology takes many years, commitment of sufficient resources, and a great deal of effort by dedicated researchers and engineers. Technologies that utilize quantum physics seem poised to offer great technological potential. Few have thus far left the laboratory. Atomic clocks, the original quantum sensors, have become robust enough for deployment in space to power the GPS technology that has become a staple of the modern world [93] and are also available as rack mounted laboratory units [81]. Several companies have begun to offer quantum sensors commercially for gravimetry [9, 12]. Commercial laser-based OPMS have also begun to be offered [68, 34, 88], but they are not sensitive at RF frequencies, focusing instead on field sensing from from DC to 100 Hz.

The maturity of a technology can be characterized by its *technology readiness level* (TRL), a number ranging from 1 for exploration of basic physical principles, to 9 for a robust, proven product [44, 48]. Figure 6.1 shows a graphic from *NASA* describing the TRL scale. At the start of this project, RF OPMs were at a TRL between 3 and 4. In this project, we have advanced them to a TRL between 5 and 6.

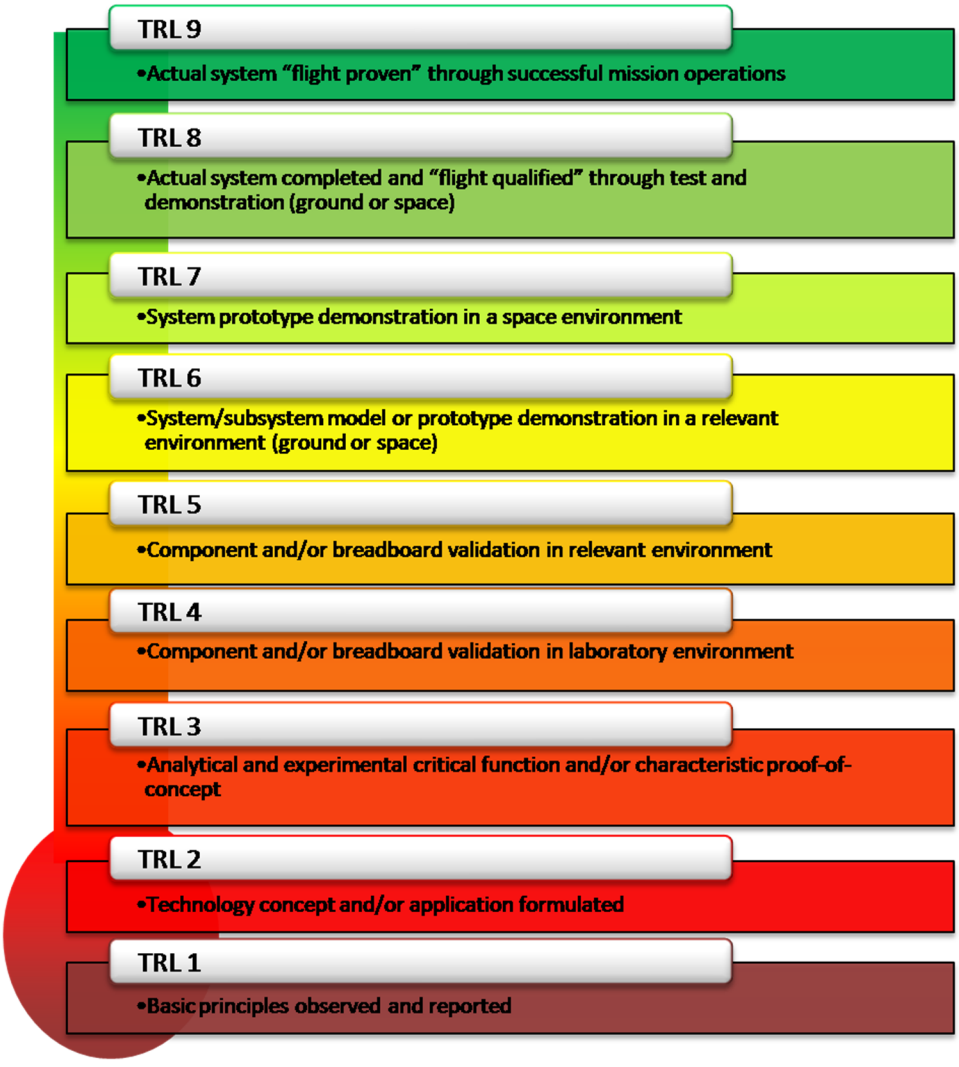

Figure 6.1: Illustrated scale from *NASA* describing technology readiness level (TRL) categories.

This places it solidly in the realm where commercial research and development may become the primary factor driving development of this concept into a highly robust technology. Many promising technologies languish in the space between TRL 3 and 5, as purely academic interest wanes, while commercial funding is not yet committed. Much of the research at a National Laboratory is conducted to bridge this critical gap. In this work, we believe this has been achieved for RF OPMs.

Many challenges remain. Additional evaluation of the trade-off between RF sensitivity and dynamic servo performance and testing of the system in more varied environments would help more completely characterize the device. Conversion of the system electronics to run directly on DC would help both to eliminate noise at harmonics of 60 Hz and to greatly improve overall system efficiency while vastly reducing the size, weight, and power of the electronics. Development of a more user friendly interface, with software automation of many tasks that have thus far been performed manually, could create a more robust device. From a fundamental physics perspective, there remains an explained broadening of the RF line-width, with around a factor of three additional sensitivity to be gained by addressing it. These challenges all appear tractable. The approach developed in this work synthesizes several OPM techniques that have heretofore been confined to laboratory demonstrations, and leverages them to lay the foundation of the RF OPM concept as a viable quantum sensor outside the laboratory, opening a path forward for commercialization to realize the societal and economic potential of an additional application for quantum sensing technology.

Appendices

Appendix A

Relevant Alkali Properties

This work is based on the physics of alkali atoms moving within a heated vapor cell. Many properties and interactions discussed in Chapter 2 ultimately require empirically determined values to calculate. Relevant formulae and values will be provided here.

The density of an alkali metal within a heated vapor cell at temperature T can be modeled using formulae derived from fits to empirical data. Singh, Dolph, and Tobias [80] compared formulae from the CRC *Handbook of Chemistry and Physics* [55], along with the work of Nesmeyanov [67] and Killian [53]. They found them all to be quite close, with especially good agreement between the results from the CRC and Nesmeyanov. The Killian formula for potassium diverges from the others at higher temperatures. For the purposes of this work, we use the CRC formula for alkali number density n at absolute temperature T in units of cm^{-3} given by [55, 80]

$$\begin{aligned} n &= \left[\left(\frac{101325\ \mathrm{Pa}}{1\ \mathrm{atm}}\right)\left(10^{A-B/T}\ \mathrm{atm}\right)\right]\left[\frac{1}{k_B T}\left(\frac{1\ \mathrm{m}}{100\ \mathrm{cm}}\right)^3\right] \\ &= n_0\left(\frac{T_0}{T}\right)\exp\left(b\left[1-\frac{T_0}{T}\right]\right) \end{aligned} \tag{A.1}$$

where A and B are parameters depending on the alkali atom. The additional parameters n_0, T_0 and b are derived from them. Different values for these parameters

Alkali	Li	Na	K	Rb	Cs
A	5.055	4.704	4.404	4.312	4.165
B (K)	8023	5377	4453	4040	3830
T_0 (K)	800.94	546.90	463.79	422.98	406.51
n_0			10^{14}		
b	23.065	22.638	22.108	21.993	21.694

Table A.1: Parameters from the CRC [55] for use in Equation A.1 for calculating the saturated vapor density of various alkali species over their liquid phase.

also apply for computing the saturated vapor pressure of an alkali species over solid or liquid alkali phases. For modeling the pressure within a vapor cell, we use the parameters for computing the density over a liquid, as we operate above the melting temperature of the alkali species typically used for OPMs. Values of these parameters are given in Table A.1.

Equation A.1 ignores the density of alkali *dimers*-diatomic alkali molecules that can form very briefly during collisions. They do not constitute a significant fraction of the alkali atoms, as they break apart very quickly after formation. However, this brief formation of a dimer during an alkali-alkali collision and the resultant splitting between singlet and triplet potentials of the dual electron bound state is actually the physical origin of spin-exchange collisions. Figure A.1 shows the density predicted by the CRC formula for various alkali species versus temperature. Because Alkali species lighter than potassium must be heated to very high temperatures to achieve appreciable vapor pressures, they are vary rarely used in vapor cell experiments. Also, as the alkali species become lighter, the transition wavelengths of the D_1 and D_2 transitions becomes shorter as summarized in table A.2, making compact high efficiency laser diodes capable of addressing them more difficult or impossible to

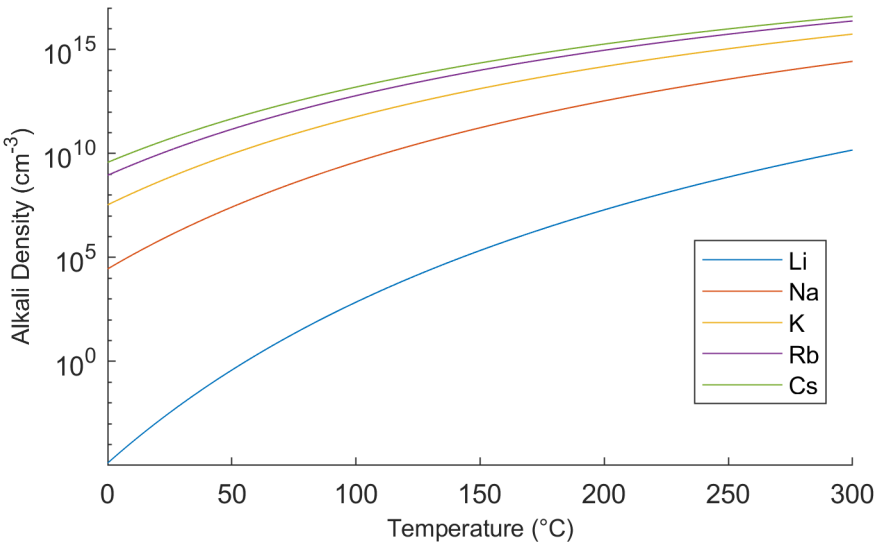

Figure A.1: Densities of alkali species over liquid predicted by Equation A.1

source.

Table A.2 summarizes some basic physical properties of various alkali isotopes

In addition to basic properties, calculation of the effects of various interactions of the alkalki atoms with their environment within the vapor cell are required for the density operator approach explored in Section 2.2.4. Here we will review sources of values to calculate these dynamic interactions between the typically used alkali species for OPMs (K,Rb, and Cs) when used within an N_2 buffer/quenching gas.

Ressler, Sands, and Stark (1969) [69] and Alexandrov et al. [1] measured the cross-sections $\sigma_{\mathrm{SE}}^{(\mathrm{Self})}$ for spin-exchange collisions between alkali of the same species. They did not measure any diffrence between isotopes of the same element. Walker and Happer (1997) [91], Kadlecek, Anderson, and Walker (1998) [51], and Allred et al. (2002) [7] measured the cross-sections for spin-destruction collisions between like alkali species $\sigma_{\mathrm{SD}}^{(\mathrm{Self})}$ as well as the cross-sections $\sigma_{\mathrm{SD}}^{(\mathrm{N_2})}$ for alkali species colliding with nitrogen gas. McGillis and Krause (1967,1968) [63, 62] and Hrycyshyn and Krause (1970) [45] measured the cross-sections $\sigma_{\mathrm{Q,D}_{1(2)}}^{(\mathrm{N_2})}$ for quenching by nitrogen gas on both

Isotope	^{39}K	^{41}K	^{85}Rb	^{87}Rb	^{133}Cs
Natural isotopic fraction, f_{Iso}	0.933	0.067	0.722	0.278	1.000
Nuclear Spin, I	3/2	3/2	5/2	3/2	7/2
D_1 Transition in Vacuum (nm)	770.1	770.1	795.0	795.0	894.6
D_2 Transition in Vacuum (nm)	766.7	766.7	780.2	780.2	852.3
D_1 Oscillator strength, f_{D_1}	0.324	0.324	0.332	0.332	0.347
D_2 Oscillator strength, f_{D_2}	0.652	0.652	0.668	0.668	0.721
D_1 Natural linewidth (FWHM, MHz)	5.94	5.94	5.75	5.75	4.57
D_2 Natural linewidth (FWHM, MHz)	6.01	6.01	6.07	6.07	5.24
Ground Hyperfine splitting (MHz)	461.7	254.0	3036	6835	9193

Table A.2: Basic properties of alkali species commonly used in hot vapor cells. Information for potassium is complied by Tiecke [86], while Steck has compiled references for both rubidium and cesium [83, 84, 82].

D line transitions. Franz and Volk (1976,1982) [36, 37] along with Silver (1984) [79] measured the diffusion constants $D_0^{(\mathrm{N_2})}$ at 273 K and 1 amg density for diffusion of various alkali species through nitrogen gas. The pressure broadenings $\Delta\Gamma^{(\mathrm{N_2})}_{\mathrm{D}_{1(2)}}$ and optical resonance shifts $\Delta\nu^{(\mathrm{N_2})}_{0,\mathrm{D}_{1(2)}}$ of the D lines of potassium in the presence of nitrogen was reported by Lwin and McCartan (1978) [56], while Romalis, Miron, and Cates (1997) [71] provide these data for rubidium, and Andalkar and Warrington (2002) [8] provide them for cesium. These data are given in Table A.3. Number densities are reported in amagats, which are defined by the relation [87]

$$1 \text{ amg} = 2.687 \times 10^{19} \text{ cm}^{-3} \tag{A.2}$$

This is also called the *Loschmidt* number (or constant). It is the number of ideal gas particles per unit volume.

Alkali	K	Rb	Cs
$\sigma_{\mathrm{SE}}^{(\mathrm{Self})}$ (cm^2)	1.8×10^{-14}	1.9×10^{-14}	2.1×10^{-14}
$\sigma_{\mathrm{SD}}^{(\mathrm{Self})}$ (cm^2)	1.0×10^{-18}	1.6×10^{-17}	2.0×10^{-16}
$\sigma_{\mathrm{SD}}^{(\mathrm{N_2})}$ (cm^2)	7.9×10^{-23}	1×10^{-22}	5.5×10^{-22}
$\sigma_{\mathrm{Q,D_1}}^{(\mathrm{N_2})}$ (cm^2)	3.5×10^{-15}	5.8×10^{-15}	5.5×10^{-15}
$\sigma_{\mathrm{Q,D_2}}^{(\mathrm{N_2})}$ (cm^2)	3.9×10^{-15}	4.3×10^{-15}	6.4×10^{-15}
$D_0^{(\mathrm{N_2})}$ $(\mathrm{cm}^2\ \mathrm{s}^{-1})$	0.20	0.19	0.10
$\Delta\Gamma_{\mathrm{D_1}}^{(\mathrm{N_2})}$ $(\mathrm{GHz\ amg}^{-1}, \mathrm{FWHM})$	21.0	17.8	14.83
$\Delta\nu_{0,\mathrm{D_1}}^{(\mathrm{N_2})}$ $(\mathrm{GHz\ amg}^{-1})$	-15.7	-8.25	-6.25
$\Delta\Gamma_{\mathrm{D_2}}^{(\mathrm{N_2})}$ $(\mathrm{GHz\ amg}^{-1}, \mathrm{FWHM})$	21.0	18.1	17.24
$\Delta\nu_{0,\mathrm{D_2}}^{(\mathrm{N_2})}$ $(\mathrm{GHz\ amg}^{-1})$	-11.3	-5.9	-5.11

Table A.3: Empirical parameters for calculating the interactions of alkali atoms with their environment within a vapor cell filled with nitrogen buffer/quenching gas. References for these values are provided in the text.

Appendix B

Calibration Details

In this appendix, the methods used to extract the true nitrogen buffer gas pressure and calibrate the magnetic field coils will be detailed.

B.1 Extraction of the Buffer Gas Density

As unpolarized light travels through a vapor cell, energy is absorbed in proportion to the alkali vapor density n and local light local intensity I, leading to an exponential attenuation of intensity with distance known as the Beer-Lambert law. In addition, the D line transitions have a absorption cross-section $\sigma(\Delta\nu, \Gamma_{\mathrm{Tot}})$ given by Equation 2.9, leading to the following relation for the light intensity as a function of the distance z traveled through the vapor

$$\begin{aligned} I(z) &= I(0) \exp\left[-n\sigma(\Delta\nu, \Gamma_{\mathrm{Tot}})z\right] \\ &= I(0) \exp\left(-\pi r_e c f_{\mathrm{Res}} n z \frac{\Gamma_{\mathrm{Tot}}/(2\pi)}{\Delta\nu^2 + (\Gamma_{\mathrm{Tot}}/2)^2}\right). \end{aligned} \tag{B.1}$$

For light traveling all the way through a cell of depth d, we may write the transmitted light intensity in terms of the optical depth OD as

$$I(d) = I(0) \exp\left[-\mathrm{OD}(\Delta\nu, \Gamma_{\mathrm{Tot}})\right], \tag{B.2}$$

where optical depth $\mathrm{OD}(\Delta\nu, \Gamma_{\mathrm{Tot}})$ is defined by

$$\begin{aligned} \mathrm{OD}(\Delta\nu, \Gamma_{\mathrm{Tot}}) &= \pi r_e c f_{\mathrm{Res}} n d \frac{\Gamma_{\mathrm{Tot}}/(2\pi)}{\Delta\nu^2 + (\Gamma_{\mathrm{Tot}}/2)^2} \\ &= \pi \frac{\Gamma_{\mathrm{Tot}}}{2} \mathrm{OD}_0 \mathrm{Re}\big(\mathcal{L}(\Delta\nu, \Gamma_{\mathrm{Tot}})\big), \end{aligned} \tag{B.3}$$

using the resonant optical depth OD_0 where $\mathcal{L}(\Delta\nu, \Gamma_{\mathrm{Tot}})$ is a Lorentzian distribution as defined by Equation 2.5 .

As discussed in Chapter 2, there is sufficient buffer gas to broaden the line to a great enough extent that the hyperfine splitting of the optical resonance cannot be resolved. Thus we can fit the total absorption spectrum to a single Lorentzian response within an exponential a profile of the form

$$I(d) = I(0) \exp\left[-\mathrm{OD}_0 \frac{\Gamma_{\mathrm{Tot}}}{2} \left(\frac{\Gamma_{\mathrm{Tot}}/2}{(\nu - \nu_0)^2 + (\Gamma_{\mathrm{Tot}}/2)^2}\right)\right] \tag{B.4}$$

where ν_0 is the optical resonance frequency.

To scan the optical frequency of our DBR laser, we slowly ramp the temperature of our laser diode, which allows for a wide scan over a range on the order of 100 GHz. The vapor cell was heated to a relatively low temperature to keep optical depth low and prevent over saturation in the absorption data. A separate data set was taken using a Moglabs (Carlton,VIC, AUS) economical wavelength meter to calibrate the change in optical frequency $\delta\nu$ of the laser from the start of the scan as a function of time $\delta\nu(t)$. Combing this with $V(t)$, we find the transmitted voltage as a function of optical frequency shift from the start of the scan $V(\delta\nu)$. The resultant data were then fit to the following function derived from the form of Equation B.4:

$$V(\nu) = (a\nu + b) \exp\left[-\mathrm{OD}_0 \left(\frac{\Gamma_{\mathrm{Tot}}}{2}\right)^2 \left(\frac{1}{(\nu - \nu_0)^2 + (\Gamma_{\mathrm{Tot}}/2)^2}\right)\right] + c, \tag{B.5}$$

where the pre-factor $(a\nu + b)$ accounts for a weak linear dependence of laser power on temperature, and we have allowed for a constant offset c to the signal. Fit parameters were a, b, c, the resonant optical depth OD_0, the resonance frequency ν_0 and of course

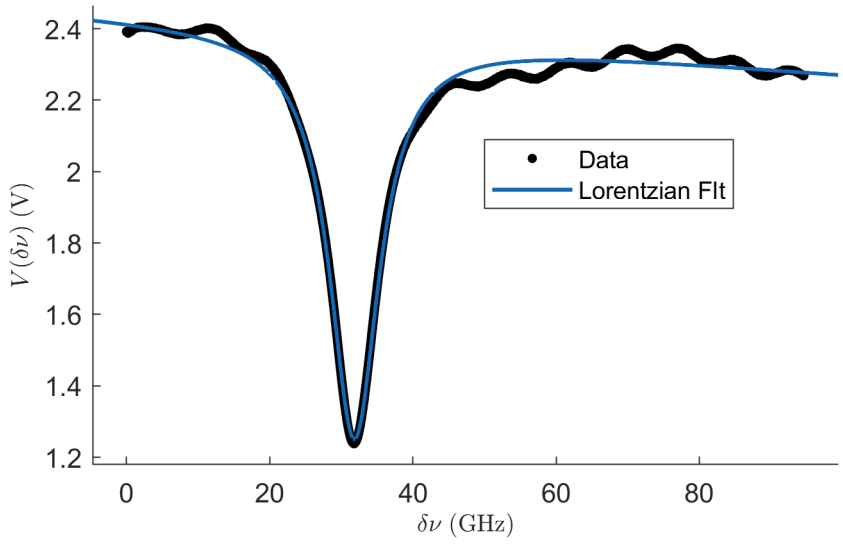

Figure B.1: Optical transmission data and a fit of the function given by Equation B.5 to them. The resultant fit has $R^2 = 0.9909$ giving a value of $\Gamma_{\text{Tot}} = 8.39$ GHz with 95% confidence in $[6.95, 9.83]$ GHz

the linewidth Γ_{Tot}. Fitting was performed in *MatLab*. The resultant fit shown Figure B.1 has $R^2 = 0.9909$ and gives a value for the optical linewidth of $\Gamma_{\text{Tot}} = 8.39$ GHz with 95% confidence in the interval $[6.95, 9.83]$ GHz. Because the linewidth is heavily dominated by pressure broadening, we can approximate the total linewidth by the pressure broadened linewidth Γ_P, so $\Gamma_{\text{Tot}} \approx \Gamma_{\text{P}}$ and combine this result with the literature value for broadening of the D_1 line by nitrogen buffer gas in rubidium from Table A.3 of $\Delta\Gamma_{\text{Tot}} = 17.8$ GHz amg^{-1} to find the density of nitrogen within the vapor cell to be

$$n_{N_2} = \frac{8.39 \text{ GHz}}{17.8 \text{ GHz amg}^{-1}} = 0.471 \text{ amg}. \tag{B.6}$$

B.2 Magnetic Field Coil Calibration

The PCBs discussed in Section 4.4 were calibrated to extract their magnetic field gains G_C using two methods: measuring shift in the Larmor resonance frequency

caused by application of DC currents, and RF measurements at a test frequency of $f_{\mathrm{RF}} = 21.5$ kHz. Both methods provide similar results, with the latter giving slightly higher values. This can likely be attributed to additional impedance due to the inductive reactance of the coils themselves becoming relevant at RF frequencies. The procedure for calibration using both methods will be detailed in this section. All calibrations were carried out within our magnetic shield to eliminate the influence of external magnetic fields on the results.

B.2.1 DC Calibration by Measurement of Resonance Shift

Equation 1.1 details how Larmor precession results from a magnetic field of given amplitude $|\mathbf{B}| = \sqrt{B_z^2 + B_x^2 + B_y^2}$. Thus by measuring the Larmor resonance frequency directly, we can find the strength of the magnetic field. For this calibration, a small ($B_{\mathrm{RF}} < 1$ nT) RF excitation field was applied at $f_{\mathrm{RF},0} = 21.5$ kHz through either the x, or y-direction modulation coils to drive resonant Larmor precession, and a bias current applied through the z-direction control coil was scanned over the Larmor resonance. Using lock-in detection, the RF resonance of ^{85}Rb was centered at $f_{\mathrm{RF},0}$. From the known gyromagnetic ratio of $_{85}$Rb $\gamma_{85} = 2\pi \times 4.671$ Hz nT^{-1}, this gives a bias field of 4.603 μT.

Within the magnetic shield, we know that $|\mathbf{B}| = B_z$ under these conditions. Thus the magnetic field gain of the z-direction coils at DC can be simply calculated from the DC current I_{DC} applied through the coils as

$$G_{\mathrm{C}}^{(z)} = \frac{4.603\ \mu\mathrm{T}}{I_{\mathrm{DC}}}. \tag{B.7}$$

The result of calibration for the z-direction are given in Table B.1. To find the gain of the transverses coils, we add a small transverse component $B_{x(y)} \ll 4.608\ \mu$T to the field, so the Larmor precession frequency shifts to

$$2\pi f_{\mathrm{RF}} = \gamma_{85}\sqrt{(4.608\ \mu\mathrm{T})^2 + B_{x(y)}^2}. \tag{B.8}$$

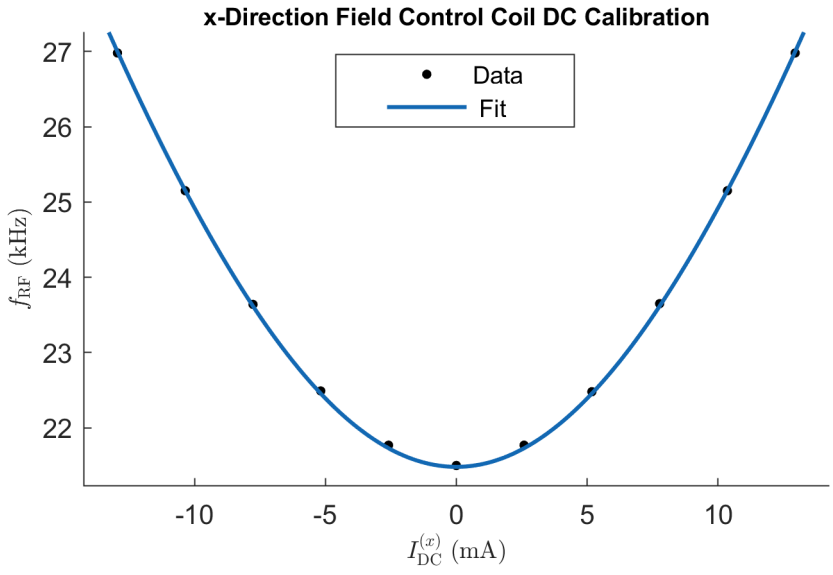

Figure B.2: Example of a nonlinear fit to Equation B.9 used extract the field coil gains.

We scan the applied RF frequency and use lock-in detection to find the new Larmor resonance frequency. Larmor frequencies were recorded for eleven different applied currents and a nonlinear fit to the data was used to extract the gains for the transverse direction field coils. Specifically, resonance frequency vs. applied current data were fit to the function

$$2\pi f_{\mathrm{RF}} = \gamma_{85}\sqrt{(4.608\ \mu\mathrm{T})^2 + (G_{\mathrm{C}} I_{x(y)})^2} + c \tag{B.9}$$

to determine the transverse coil gains G_{C}. Results are listed in Table B.1.

B.2.2 RF Calibration by Free Induction Decay

To calibrate the coils directly at RF frequencies, a function generator with 50 Ω output impedance was connected to the coil to be tested through a current divider formed from a 50 Ω resistor and additional resistor of resistance R_{In} as shown in Figure B.3. For our test frequency, inductive reactance from the coils was not expected

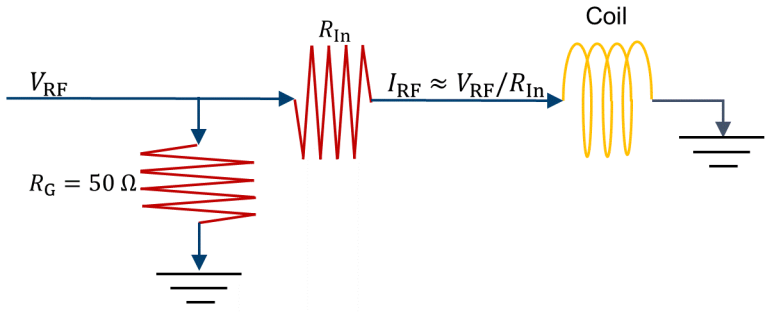

Figure B.3: Current divider circuit used in RF calibrations. A 50 Ω resistor is used to impedance match to the function generator. Current through the test coil is then approximately $V_{\mathrm{RF}}/R_{\mathrm{In}}$.

make a significant contribution to the total impedance. The coils themselves have a measured resistance of 12 to 13 Ω for the control coils and around 0.5 Ω for the modulation coils. By selecting an input resistor $R_{\mathrm{In}} \gg 50\ \Omega$, the impedance of the devider circuit is $Z_D = (R_{\mathrm{In}} \times 50\ \Omega)/(50\ \Omega + R_{\mathrm{In}}) \approx 50\ \Omega$, which properly matches the output impedance of the function generator. The current through the coil at RF frequencies provided from the function generator output voltage V_{RF} is then simply $I_{\mathrm{RF}} \approx V_{\mathrm{RF}}/R_{\mathrm{In}}$.

To find the RF calibration of the field coils at our test frequency, an optical chopper (a rotating slotted disc) was put in the path of the pump laser to periodically block the optical pumping beam. This effective introduces an on/off (square wave) modulation of optical the pumping rate. As the spins begin to decay freely in the absence of pumping light, the ensemble will still be subject to the influence of the RF magnetic field. In the RWA, this appears as a DC field of magnitude $B_{\mathrm{RF}}/2$ in the rotating frame, about which the atoms will begin to precess with a decaying amplitude as the spins relax. The frequency of this decaying oscillation will be

$$\begin{aligned} 2\pi f' &= \gamma_{85}(\tfrac{1}{2}B_{\mathrm{RF}}) \\ &= \tfrac{1}{2}\gamma_{85}G_{\mathrm{C}}I_{\mathrm{RF}}, \end{aligned} \tag{B.10}$$

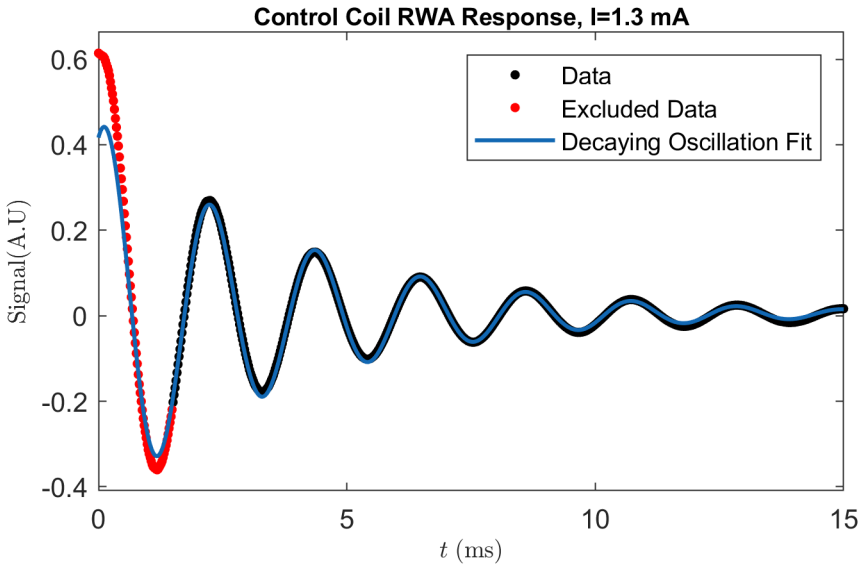

Figure B.4: Free induction decay data from a field control coil with an RF current amplitude of $I_{\mathrm{RF}} = 1.3$ mA. Signal from the rotating frame of the atomic spins is obtained via lock-in demodulation at f_{RF} showing the characteristic decaying oscillation. A fit to Equation B.11 is also shown. Early data for $t < 1.5$ ms are excluded because the decay is super-exponential for short times.

thus by measuring the frequency of this precession in the rotating frame, we can extract the RF coil calibration. To do so, we use lock-in detection at $f_{\mathrm{RF}} = 21.5$ kHz to get the decaying oscillation signal in the rotating frame, and then fit the resultant signal to the function

$$S(t) = ae^{-t/\tau}\sin\left(\tfrac{1}{2}\tfrac{1}{2\pi}\gamma_{85}G_{\mathrm{C}}I_{\mathrm{C}}t + \phi\right) + c \tag{B.11}$$

where a, τ, ϕ, c and G_{C} are free fit parameters. An example data set and fit from a field control coil calibration with RF current amplitude of $I_{\mathrm{RF}} = 1.3$ mA is shown in Figure B.4.

Resistors with values ranging from $R_{\mathrm{In}} = 1$ kΩ to 10 kΩ corresponding to RF current amplitudes of 5 mA to 500 μA were used to test the response at decreasing RF signal amplitudes. Table B.1 summarizes the measured coil calibrations using both methods.

Coil	Gain (nT mA^{-1})	Method	Uncertainty (nT mA^{-1})
z Control	270	DC Set	
x Control	269	DC Offset	± 0.5
x Modulation	46	DC Offset	± 0.9
	44.5	RF FID	± 1
y Control	258	RF FID	± 4.6
y Modulation	44.3	DC Offset	± 0.9
	45.2	RF FID	± 1.6

Table B.1: Calibrated values of magnetic field gain for the various PCB field control coils found using the methods in this section. Uncertainties for DC offset method results are from 95% fit confidence. Uncertainties for the RF FID method are standard deviations over tests at ten RF current amplitudes from 5 mA to 500 μA.

References

[1] Aleksandrov, E., Balabas, M., and Vershovskii, A. Spin-exchange broadening of magnetic-resonance line. *Optics and Spectroscopy 87*, 3 (1999), 329–334.

[2] Alexandrov, E., and Vershovskiy, A. M_x and m_z magnetometers. In Budker and Kimball [21].

[3] Alexandrov, E. B., Balabas, M., Kulyasov, V. N., Ivanov, A. E., Pazgalev, A. S., Rasson, J. L., Vershovski, A. K., and Yakobson, N. N. Three-component variometer based on a scalar potassium sensor. *Measurement Science and Technology 15*, 5 (apr 2004), 918–922.

[4] Alexandrov, E. B., and Rasson, J. L. Concept of a vector magnetic field stabbilizer. No. STR98/21, IAGA, GFZ Scientific Technical Report, pp. 131–135.

[5] Allegrini, M., Arimondo, E., and Orozco, L. A. Survey of hyperfine structure measurements in alkali atoms. *Journal of Physical and Chemical Reference Data 51*, 4 (2022), 043102.

[6] Allen, J., and Bender, P. Narrow line rubidium magnetometer for high accuracy field measurements. *Journal of geomagnetism and geoelectricity 24*, 1 (1972), 105–125.

[7] Allred, J. C., Lyman, R. N., Kornack, T. W., and Romalis, M. V. High-sensitivity atomic magnetometer unaffected by spin-exchange relaxation. *Phys. Rev. Lett. 89* (Sep 2002), 130801.

[8] Andalkar, A., and Warrington, R. B. High-resolution measurement of the pressure broadening and shift of the cs $d1$ and $d2$ lines by n_2 and he buffer gases. *Phys. Rev. A 65* (Feb 2002), 032708.

[9] Aosense: Gravimeter. `https://aosense.com/products/atom-optic-sensors/gravimeter/`. Market an atom interferometer gravimeter.

[10] Appelt, S., Baranga, A. B.-A., Erickson, C. J., Romalis, M. V., Young, A. R., and Happer, W. Theory of spin-exchange optical pumping of ^{3}He and ^{129}Xe. *Phys. Rev. A 58* (Aug 1998), 1412–1439.

[11] Appelt, S., Ben-Amar Baranga, A., Young, A. R., and Happer, W. Light narrowing of rubidium magnetic-resonance lines in high-pressure optical-pumping cells. *Phys. Rev. A 59* (Mar 1999), 2078–2084.

[12] Atomsensors: Atomic gravity gradiometer/gravimeter. `http://www.atomsensors.com/index.php/en/products/atomic-gravity-gradiometer-gravimeter`. Market a commerical atom interferometer gravimeter/gradiometer.

[13] Auzinsh, M., Budker, D., and Rochester, S. *Optically Polarized Atoms: Understanding Light-atom Interactions*. OUP Oxford, 2010.

[14] Ballentine, L. *Quantum Mechanics: A Modern Development*. World Scientific, 1998.

[15] Bevington, P., Gartman, R., Botelho, D. J., Crawford, R., Packer, M., Fromhold, T. M., and Chalupczak, W. Object surveillance with radio-frequency atomic magnetometers. *Review of Scientific Instruments 91*, 5 (2020), 055002.

[16] Bevington, P., Gartman, R., and Chalupczak, W. Enhanced material defect imaging with a radio-frequency atomic magnetometer. *Journal of Applied Physics 125*, 9 (2019), 094503.

[17] Bevington, P., Gartman, R., and Chalupczak, W. Imaging of material defects with a radio-frequency atomic magnetometer. *Review of Scientific Instruments 90*, 1 (2019), 013103.

[18] Bevington, P., Gartman, R., Chalupczak, W., Deans, C., Marmugi, L., and Renzoni, F. Non-destructive structural imaging of steelwork with atomic magnetometers. *Applied Physics Letters 113*, 6 (2018), 063503.

[19] Bloch, F. Nuclear induction. *Phys. Rev. 70* (Oct 1946), 460–474.

[20] Brill, R. Differential geomagnetic field measurements at the edge of the denver basin. *Journal of Geophysical Research (1896-1977) 80*, 11 (1975), 1593–1599.

[21] Budker, D., and Kimball, D., Eds. *Optical Magnetometry*. Optical Magnetometry. Cambridge University Press, 2013.

[22] Cooper, R., Prescott, D., and Sauer, K. Magnetic field mapping and the detection of explosives using radio-frequency atomic magnetometers. In *APS Division of Atomic, Molecular and Optical Physics Meeting Abstracts* (May 2018), vol. 2018 of *APS Meeting Abstracts*, p. S08.006.

[23] Cooper, R. J., Mark, B. L., Prescott, D. W., and Sauer, K. L. Improving the design of atomic magnetometer arrays for RF interference mitigation in NQR detection of explosives. In *Detection and Sensing of Mines, Explosive Objects, and Obscured Targets XXII* (2017), S. S. Bishop and J. C. Isaacs, Eds., vol. 10182, International Society for Optics and Photonics, SPIE, p. 1018208.

[24] Cooper, R. J., Prescott, D. W., Matz, P., Sauer, K. L., Dural, N., Romalis, M. V., Foley, E. L., Kornack, T. W., Monti, M., and Okamitsu, J. Atomic magnetometer multisensor array for rf interference mitigation and unshielded detection of nuclear quadrupole resonance. *Phys. Rev. Applied 6* (Dec 2016), 064014.

[25] Corney, A. *Atomic and Laser Spectroscopy*. Oxford science publications. Clarendon Press, 1977.

[26] Corporation, N. I. Ni pxie-7857r specifications. Online, Available at https://www.ni.com/docs/en-US/bundle/pxie-7857-specs/page/specs.html, 2023.

[27] Cristofolinini. Thermal and shot noise. appendix c. Online. Available at `https://web.archive.org/web/20181024162550/http://www.fis.unipr.it/~gigi/dida/strumentazione/harvard_noise.pdf`. From the notes of Prof. Cristofolinini, University of Parma. Archived on Wayback Machine.

[28] Deans, C., Cohen, Y., Yao, H., Maddox, B., Vigilante, A., and Renzoni, F. Electromagnetic induction imaging with a scanning radio frequency atomic magnetometer. *Applied Physics Letters 119*, 1 (2021), 014001.

[29] Deans, C., Marmugi, L., Hussain, S., and Renzoni, F. Electromagnetic induction imaging with a radio-frequency atomic magnetometer. *Applied Physics Letters 108*, 10 (2016), 103503.

[30] Deans, C., Marmugi, L., and Renzoni, F. Active underwater detection with an array of atomic magnetometers. *Appl. Opt. 57*, 10 (Apr 2018), 2346–2351.

[31] Deans, C., Marmugi, L., and Renzoni, F. Sub-picotesla widely tunable atomic magnetometer operating at room-temperature in unshielded environments. *Review of Scientific Instruments 89*, 8 (2018), 083111.

[32] Deans, C., Marmugi, L., and Renzoni, F. Sub-sm–1 electromagnetic induction imaging with an unshielded atomic magnetometer. *Applied Physics Letters 116*, 13 (2020), 133501.

[33] Dhombridge, J. E., Claussen, N. R., Iivanainen, J., and Schwindt, P. D. High-sensitivity rf detection using an optically pumped comagnetometer based on natural-abundance rubidium with active ambient-field cancellation. *Phys. Rev. Applied 18* (Oct 2022), 044052.

[34] Fieldline. Online, available at `https://fieldlineinc.com/`. Developers of the HEDscan MEG system using OPMs.

[35] Franz, F. Enhancement of alkali optical pumping by quenching. *Physics Letters A 27*, 7 (1968), 457–458.

[36] Franz, F. A., and Volk, C. Spin relaxation of rubidium atoms in sudden and quasimolecular collisions with light-noble-gas atoms. *Phys. Rev. A 14* (Nov 1976), 1711–1728.

[37] Franz, F. A., and Volk, C. Electronic spin relaxation of the $4^2s_{\frac{1}{2}}$ state of k induced by k-he and k-ne collisions. *Phys. Rev. A 26* (Jul 1982), 85–92.

[38] Gardner, W. *Introduction to Random Processes: With Applications to Signals and Systems*. Macmillan Publishing Company, 1986.

[39] Harris, D., and Bertolucci, M. *Symmetry and Spectroscopy: An Introduction to Vibrational and Electronic Spectroscopy*. Dover Books on Chemistry Series. Dover Publications, 1989.

[40] Hertz, H. Ueber einen einfluss des ultravioletten lichtes auf die electrische entladung. *Annalen der Physik 267*, 8 (1887), 983–1000.

[41] Hertz, H. Ueber sehr schnelle electrische schwingungen. *Annalen der Physik 267*, 7 (1887), 421–448.

[42] Hertz, H. Ueber die ausbreitungsgeschwindigkeit der electrodynamischen wirkungen. *Annalen der Physik 270*, 7 (1888), 551–569.

[43] Hertz, H. Ueber die einwirkung einer geradlinigen electrischen schwingung auf eine benachbarte strombahn. *Annalen der Physik 270*, 5 (1888), 155–170.

[44] Hook-Barnard I, M. Posey Norris S, A. J., Ed. *Technology Readiness Levels in the Department of Defense* (2013), Board on Health Sciences Policy; Board on Life Sciences; Institute of Medicine; National Research Council, National Academies Press (US). Technology Readiness Levels in the Department of Defense. Available from: https://www.ncbi.nlm.nih.gov/books/NBK201356/.

[45] Hrycyshyn, E., and Krause, L. Inelastic collisions between excited alkali atoms and molecules. vii. sensitized fluorescence and quenching in mixtures of rubidium with h2, hd, d2, n2, ch4, cd4, c2h4, and c2. h6. *Canadian Journal of Physics 48*, 22 (1970), 2761–2768.

[46] Hussain, S., Marmugi, L., Deans, C., and Renzoni, F. Electromagnetic imaging with atomic magnetometers: a novel approach to security and surveillance. In *Detection and Sensing of Mines, Explosive Objects, and Obscured Targets XXI* (2016), S. S. Bishop and J. C. Isaacs, Eds., vol. 9823, International Society for Optics and Photonics, SPIE, p. 98230Q.

[47] Iqbal, K. *Introduction to Control Systems*. LibreTexts, 2023.

[48] Technology readiness level. `https://www.nasa.gov/directorates/heo/scan/engineering/technology/technology_readiness_level`. NASA Information Page. Accessed 03/2023.

[49] Rec. itu-r v.431-7, nomenclature of the frequency and wavelength bands used in telecommunications. Archived on the WayBack machine of the Internet Achive at .

[50] Jensen, K., Zugenmaier, M., Arnbak, J., Stærkind, H., Balabas, M. V., and Polzik, E. S. Detection of low-conductivity objects using eddy current measurements with an optical magnetometer. *Phys. Rev. Research 1* (Nov 2019), 033087.

[51] Kadlecek, S., Anderson, L., and Walker, T. Measurement of potassium-potassium spin relaxation cross sections. *Nuclear Instruments and Methods in Physics Research Section A: Accelerators, Spectrometers, Detectors and Associated Equipment 402*, 2 (1998), 208–211. Proceedings of the 7th RCNP International Workshop on Polarized He Beams and Gas Targets and Their Application.

[52] Keder, D. A., Prescott, D. W., Conovaloff, A. W., and Sauer, K. L. An unshielded radio-frequency atomic magnetometer with sub-femtotesla sensitivity. *AIP Advances 4*, 12 (2014), 127159.

[53] Killian, T. J. Thermionic phenomena caused by vapors of rubidium and potassium. *Phys. Rev. 27* (May 1926), 578–587.

[54] Lee, S.-K., Sauer, K. L., Seltzer, S. J., Alem, O., and Romalis, M. V. Subfemtotesla radio-frequency atomic magnetometer for detection of nuclear quadrupole resonance. *Applied Physics Letters 89*, 21 (2006), 214106.

[55] Lide, D. R., Ed. *CRC Handbook of Chemistry and Physics*, 75th ed. CRC Press, 1995.

[56] Lwin, N., and McCartan, D. G. Collision broadening of the potassium resonance lines by noble gases. *Journal of Physics B: Atomic and Molecular Physics 11*, 22 (nov 1978), 3841.

[57] Maddox, B., Cohen, Y., and Renzoni, F. Imaging corrosion under insulation with a mechanically-translatable atomic magnetometer. In *2022 IEEE International Workshop on Metrology for Industry 4.0 & IoT (MetroInd4.0&IoT)* (2022), pp. 104–108.

[58] Marmugi, L., Deans, C., and Renzoni, F. Electromagnetic induction imaging with atomic magnetometers: Unlocking the low-conductivity regime. *Applied Physics Letters 115*, 8 (2019), 083503.

[59] Marmugi, L., Gori, L., Hussain, S., Deans, C., and Renzoni, F. Remote detection of rotating machinery with a portable atomic magnetometer. *Appl. Opt. 56*, 3 (Jan 2017), 743–749.

[60] Marmugi, L., and Renzoni, F. Electromagnetic induction imaging with atomic magnetometers: Progress and perspectives. *Applied Sciences 10*, 18 (2020).

[61] Maxwell, J. C. Viii. a dynamical theory of the electromagnetic field. *Philosophical Transactions of the Royal Society of London 155* (1865), 459–512.

[62] McGillis, D., and Krause, L. Inelastic collisions between excited alkali atoms and molecules. iv. sensitized fluorescence and quenching in mixtures of cesium with n2, h2, hd, and d2. *Canadian Journal of Physics 46*, 9 (1968), 1051–1057.

[63] McGillis, D. A., and Krause, L. Inelastic collisions between excited alkali atoms and molecules. i. sensitized fluorescence and quenching in cs-n_2 and cs-h_2 systems. *Phys. Rev. 153* (Jan 1967), 44–50.

[64] Migdalek, J., and Kim, Y.-K. Core polarization and oscillator strength ratio anomaly in potassium, rubidium and caesium. *Journal of Physics B: Atomic, Molecular and Optical Physics 31*, 9 (1998), 1947.

[65] Molisch, A., and Oehry, B. *Radiation Trapping in Atomic Vapours*. Oxford science publications. Clarendon Press, 1998.

[66] Mäkinen, A. J., Zetter, R., Iivanainen, J., Zevenhoven, K. C. J., Parkkonen, L., and Ilmoniemi, R. J. Magnetic-field modeling with surface currents. part i. physical and computational principles of bfieldtools. *Journal of Applied Physics 128*, 6 (2020), 063906.

[67] Nesmeyanov, A. N. *Vapor Pressure of the Elements*. Academic Press, New York, 1963. Translated by J.S. Carasso.

[68] Quspin: An atomic devices company. `https://quspin.com/`. Developers of several commerical low-frequency OPMs.

[69] Ressler, N. W., Sands, R. H., and Stark, T. E. Measurement of spin-exchange cross sections for cs^{133}, rb^{87}, rb^{85}, k^{39}, and na^{23}. *Phys. Rev. 184* (Aug 1969), 102–118.

[70] Romalis, M. Quantum noise in atomic magnetometers. In Budker and Kimball [21].

[71] Romalis, M. V., Miron, E., and Cates, G. D. Pressure broadening of rb D_1 and D_2 lines by ^{3}he, ^{4}he, n_2, and xe: Line cores and near wings. *Phys. Rev. A 56* (Dec 1997), 4569–4578.

[72] Rushton, L. M., Pyragius, T., Meraki, A., Elson, L., and Jensen, K. Unshielded portable optically pumped magnetometer for the remote detection of conductive objects using eddy current measurements, 2022.

[73] Savukov, I., and Karaulanov, T. Magnetic-resonance imaging of the human brain with an atomic magnetometer. *Applied Physics Letters 103*, 4 (2013), 043703.

[74] Savukov, I., Seltzer, S. J., and Romalis, M. V. Detection of nmr signals with a radio-frequency atomic magnetometer. *Journal of Magnetic Resonance 185*, 2 (2007), 214–220.

[75] Savukov, I. M., Seltzer, S. J., Romalis, M. V., and Sauer, K. L. Tunable atomic magnetometer for detection of radio-frequency magnetic fields. *Phys. Rev. Lett. 95* (Aug 2005), 063004.

[76] Savukov, I. M., Zotev, V. S., Volegov, P. L., Espy, M. A., Matlashov, A. N., Gomez, J. J., and Jr., R. H. K. Mri with an atomic magnetometer suitable for practial imaging applications. *Journal of Magnetic Resonance 199*, 2 (2009), 188–191.

[77] Seltzer, S. J. *Developments in Alkali-Metal Atomic Magnetometry*. Ph.D. thesis, Princeton University, November 2008.

[78] Seltzer, S. J., Rampulla, D. M., Rivillon-Amy, S., Chabal, Y. J., Bernasek, S. L., and Romalis, M. V. Testing the effect of surface coatings on alkali atom polarization lifetimes. *Journal of Applied Physics 104*, 10 (2008), 103116.

[79] Silver, J. A. Measurement of atomic sodium and potassium diffusion coefficients. *The Journal of Chemical Physics 81*, 11 (1984), 5125–5130.

[80] Singh, J., Dolph, P. A., and Tobias, W. A. Alkali metal vapor pressures & number densities for hybrid spin exchange optical pumping. `https://people.nscl.msu.edu/ singhj/docs/vp195.pdf`, 2008. Version 1.95. Accessed: 3/12/2023.

[81] Rubidium audio clock. Online, Available at `https://www.thinksrs.com/products/perf10.html`. Commercially available rack sized atomic clock.

[82] Steck, D. A. Cesium d line data. `https://steck.us/alkalidata/cesiumnumbers.pdf`, 2019. Rev. 2.2.1. Accessed 03/12/2023.

[83] Steck, D. A. Rubidium 85 d line data. `https://steck.us/alkalidata/rubidium85numbers.pdf`, 2021. Rev. 2.2.2. Accessed 03/12/2023.

[84] Steck, D. A. Rubidium 87 d line data. `https://steck.us/alkalidata/rubidium87numbers.pdf`, 2021. Rev. 2.2.3. Accessed 03/12/2023.

[85] Broadband polarizing beamsplitter cubes: Specs. `https://www.thorlabs.com/newgrouppage9.cfm?objectgroup_id=739`, 2022. Information on "Specs" tab.

[86] Tiecke, T. G. Properties of potassium. `https://www.tobiastiecke.nl/archive/PotassiumProperties.pdf`, 2019. Version 1.03. Accessed 03/12/2023.

[87] Tiesinga, E., Mohr, P. J., Newell, D. B., and N., T. B. The 2018 codata recommended values of the fundamental physical constants. `http://physics.nist.gov/constants`, 2022. National Institute of Standards and Technology, Gaithersburg, MD 20899. (Web Version 8.1) Database developed by J. Baker, M. Douma, and S. Kotochigova.

[88] Ms-1l compact magnetic shield. `https://twinleaf.com`. Market several commerical OPMs.

[89] Ms-1l compact magnetic shield. `https://twinleaf.com/shield/MS-1L/`, 2023.

[90] Vershovskii, A., Balabas, M., Ivanov, A., Kulyasov, V., Pazgalev, A., and Aleksandrov, E. Fast three-component magnetometer-variometer based on a cesium sensor. *Technical Physics 51*, 1 (2006), 112–117.

[91] Walker, T. G., and Happer, W. Spin-exchange optical pumping of noble-gas nuclei. *Rev. Mod. Phys. 69* (Apr 1997), 629–642.

[92] Ware, R. H. Improved self-calibrating rubidium magnetometer accurate to 0.01 nt rms. *Review of Scientific Instruments 54*, 12 (1983), 1739–1743.

[93] Gps timing. Online, available at `https://www.gps.gov/applications/timing/`. GPS is operated and maintained by the U.S. Space Force. Website maintained by the National Coordination Office for Space-Based Positioning, Navigation, and Timing and hosted by NOAA.

[94] Wickenbrock, A., Jurgilas, S., Dow, A., Marmugi, L., and Renzoni, F. Magnetic induction tomography using an all-optical 87rb atomic magnetometer. *Opt. Lett. 39*, 22 (Nov 2014), 6367–6370.

[95] Wickenbrock, A., Tricot, F., and Renzoni, F. Magnetic induction measurements using an all-optical 87rb atomic magnetometer. *Applied Physics Letters 103*, 24 (2013), 243503.

[96] Workman, R. L., and Others. Review of Particle Physics. *PTEP 2022* (2022), 083C01.

[97] Zetter, R., J. Mäkinen, A., Iivanainen, J., Zevenhoven, K. C. J., Ilmoniemi, R. J., and Parkkonen, L. Magnetic field modeling with surface currents. part ii. implementation and usage of bfieldtools. *Journal of Applied Physics 128*, 6 (2020), 063905.